U.PORTO
FACULDADE DE CIÊNCIAS
UNIVERSIDADE DO PORTO

U.PORTO
INSTITUTO DE CIÊNCIAS BIOMÉDICAS ABEL SALAZAR
UNIVERSIDADE DO PORTO

Development of Neurotherapeutic Polyplexes for Oxidative Stress in Ischemic Stroke

Joana Filipa Ferreira Moreira

Dissertação de Mestrado em Bioquímica apresentada à

Faculdade de Ciências e ao Instituto de Ciências Biomédicas

Abel Salazar

Universidade do Porto

2020

Orientador
Sofia Duque Santos, Research Scientist, nBTT, i3S

Coorientador
Ana Paula Pêgo, Group Leader, nBTT, i3S

Agradecimentos

Queria começar por agradecer à minha orientadora Sofia Santos por todos os ensinamentos que me transmitiu, pela sua simpatia, paciência e espírito de ajuda. Também queria agradecer à minha orientadora Ana Paula Pêgo pela oportunidade de ingressar no grupo nBTT e por todas as sugestões que me permitiram avançar neste projeto. São de facto grandes exemplos de investigadoras brilhantes, que um dia desejo alcançar.

À equipa do iDNArt por toda a ajuda que me deram relativamente às dificuldades encontradas ao longo deste trabalho. Queria agradecer em especial à Ana Martins por todo o acompanhamento que me deu em várias técnicas que realizei.

À Victoria Leiro e à Ana Jesus por toda o auxílio na parte da síntese química, foram sem dúvida uma ajuda imprescindível.

Por fim, queria agradecer a todos os membros do grupo nBTT, pelo seu dinamismo, simpatia e exemplo de excelência científica.

Agradeço a todas as plataformas científicas do i3s que me facultaram formação em várias técnicas e metodologias, aprendi muito com este projeto.

Queria também agradecer a todos os meus amigos e colegas de faculdade por todo o apoio que me deram, principalmente nos momentos de maior dificuldade.

Queria fazer um muito especial ao Rui, o meu companheiro de viagem para a faculdade. De facto, enfrentamos obstáculos na nossa vida académica, sempre com espírito de ente-ajuda e cumplicidade. É sem dúvida uma das pessoas mais carismáticas que conheci e uma jovem promessa na área da ciência.

Por último, queria agradecer a toda a minha família por todo o apoio que me deram e por perdoarem sempre as minhas ausências. Em especial, queria agradecer aos meus pais que me deram esta oportunidade de prosseguir para o ensino superior que por dificuldades da vida nunca a tiveram, que implicou muito esforço e trabalho por sua parte.

Abstract

Ischemic stroke is one of the main causes of death and morbidity worldwide. This pathology is characterized by a series of molecular events in the affected cerebral area, which include oxidative stress, deregulation of genetic expression, inflammation, and cell death. In this context, the present work had the goal of developing a neuroprotective therapy based in a trimethyl chitosan (TMC) delivery vector functionalized with a brain derived neurotrophic factor (BDNF) mimetic called LM22A1 that was then complexed with anti-mir145. The mimetic was used with the intent of promoting neuronal survival by activating TrkB receptors. The anti-mir145 antagonizes the effects of miRNA145, which decreased SOD2 levels in the case of ischemic stroke, with impact in oxidative stress.

Synthesis and characterization of TMC-PEG-LM22A1 was performed. Poly(ethylene) glycol (PEG) was used to covalently bind TMC and LM22A1 and to increase polyplex stability. The success of this synthesis was confirmed by ^{1}H-NMR and UV-Vis spectroscopy. The different polyplexes – TMC, TMC-PEG and TMC-PEG-LM22A1- formed after complexation with a miRNA, were characterized for their size, polydispersity and zeta potential using DLS. The incorporation of PEG resulted in a decrease in zeta potential and size. The presence of LM22A1 in the polyplex did not affect size but did increase polydispersity and reduced zeta potential more profoundly.

We evaluated the activation of the TrkB by the BDNF mimetics- LM22A1, modified LM22A1 (with a cysteine used for polymer functionalization), and LM22A4 (commercial mimetic). These studies were done using neuronal primary cell cultures and in neuronal cell lines by immunocytochemistry, ELISA and Western blot. Overall, TrkB activation in the presence of the mimetics could not be confirmed.

The expression of SOD2 was evaluated using real-time qPCR, in neuronal cells in conditions of glutamate oxidative stress. There were no significant alterations in the mRNA levels of SOD2 for most of glutamate concentrations used. To complement these studies, ROS levels were measured using a oxidative stress probe.

Finally, we performed internalization studies of the different TMCs complexed with a fluorescent miRNA. The nanoparticles were efficiently internalized though it is still necessary to quantify its extent.

These novel TMC polyplexes are expected to become a successful system to interfere with the oxidative stress and rescue ischemic neurons.

Keywords: Ischemic stroke, Neuroprotection, Delivery Vectors, Gene Therapy

Resumo

O acidente vascular cerebral isquémico constitui umas das principais causas de morte e morbilidade a nível mundial. Nesta patologia ocorre uma série de eventos moleculares na área cerebral afetada que incluem desregulação da expressão genética, inflamação, stress oxidativo e morte celular. Neste contexto, este projeto teve como objetivo o desenvolvimento de uma terapia neuroprotetora baseada na criação de um vetor de polímero trimetilquitosano (TMC) funcionalizado com um mimético do fator neurotrófico derivado do cérebro (BDNF) designado LM22A1 (aumento da sobrevivência neuronal) e complexado com anti-mir 145 (antagoniza o efeito do miRNA145, que por sua vez diminui os níveis de superóxido dismutase 2)

Inicialmente foi realizada a reação de síntese e caracterização do copolímero de TMC-PEG-LM22A1. O polietilenoglicol (PEG) foi utilizado para estabelecer a ligação ao TMC ao LM22A1 e aumentar a estabilidade dos poliplexos. Foi confirmado por ^{1}H-NMR e por Espectroscopia UV/Visível que a ligação do mimético ao polímero foi bem-sucedida. Os poliplexos- TMC-PEG-LM22A1 TMC e TMC-PEG- formados após a complexação com um miRNA, foram caracterizados em termos de tamanho, polidispersão e potencial zeta pela técnica de Dispersão Dinâmica de Luz. Foi observado que a incorporação do PEG resultou numa diminuição do tamanho e potencial zeta. Por sua vez, a presença do péptido LM22A1 no poliplexo não alterou o seu tamanho, mas foi verificado um aumento da polisdispersão e redução mais acentuada do potencial zeta.

Também foi avaliada a performance na ativação dos recetores TrkB por parte dos miméticos do BDNF livres- LM22A1, LM22A1 com uma cisteína modificada (utilizado para a funcionalização ao polímero) e LM22A4. Estes estudos foram realizados em culturas primárias de neurónios de córtex de ratinho e em linhas celulares neuronais por Imunocitoquímica, ELISA e Western Blot. Em geral, não foi comprovado o efeito dos miméticos na ativação do recetor TrkB.

Foi ainda avaliada a expressão da enzima SOD2 por PCR Quantitativo em tempo real, em linhas celulares neuronais em que foi induzido o stress oxidativo por glutamato. Não foram verificadas alterações significativas nos níveis da mRNA de SOD2 na maioria das concentrações estudadas. Para complementar estes estudos, também foi avaliada a produção de espécies reativas de oxigénio por uma sonda de stress oxidativo.

Por fim, foram realizados ensaios de internalização dos diferentes TMCs complexados com um miRNA fluorescente. As nanopartículas foram eficientemente internalizadas, sendo necessário quantificar a sua extensão.

Table of contents

Agradecimentos i
Abstract ii
Resumo iii
Figure Index vii
Table Index x
Abbreviations, Acronyms and Symbols xi
1.Introduction 1
1.1 Stroke 1
1.2 The Ischemic Stroke 2
1.2.1 Pathophysiology of Ischemic Stroke 2
1.2.2 Molecular Mechanisms of Ischemic Stroke 3
1.2.3 Current Treatments for Ischemic Stroke 6
1.3 Neuroprotective Approaches 7
1.3.1 Neuroprotective effect of BDNF 9
1.4 Epigenetic Modifications in Ischemic Stroke: miRNA-145 12
1.5 MiRNAs-based gene-therapies 14
1.6 Viral and non-viral delivery vectors in Gene Therapy 15
1.7 Biological barriers and non-viral vector design 16
1.8 Chitosan delivery vector 18
1.9 Aims 21
2. Materials and Methods 22
2.1 Synthesis of TMC-PEG-LM22A1 Copolymer 22
2.1.1 TMC functionalization with PEG linker 22
2.1.2 TMC-PEG Bioconjugation with LM22A1 BDNF mimetic 23
2.1.3 TMC Quantification by Cibacron Method 23
2.1.4 Functionalization evaluation by Ultraviolet/Visible (UV/Vis) Spectroscopy 24
2.2 Production and physical characterization of TMC, TMC-PEG and TMC-PEG-LM22A1 Polyplexes 25
2.2.1 Production of TMC, TMC-PEG and TMC-PEG-LM22A1 Polyplexes 25
2.2.2 Characterization of TMC, TMC-PEG and TMC-PEG-LM22A1 polyplexes by Dynamic Light Scattering (DLS) 26
2.3 Cell Culture 26
2.3.1 HT22-GFP Cell line 26
2.3.2 Primary Cortical Cell Culture 27
2.4 Evaluation of TrkB Phosphorylation 27

2.4.1 Immunocytochemistry 27
2.4.2 Sandwich Enzyme-linked Immunosorbent (ELISA) Assay 29
2.4.3 Western Blot 30
2.5. Glutamate-induced Oxidative Stress 32
2.5.1 Quantification of SOD2 Expression 32
2.5.2 Quantification of ROS production by Flow Cytometry 34
2.6 Nanoparticles Cellular Internalization Assays 35
3 Results and Discussion 37
3.1 Synthesis of TMC-PEG-LM22A1 Copolymer 37
3.2 Structural Characterization of TMC, TMC-PEG and TMC-PEG-LM22A1 Nanoparticles 38
3.2.1 Nanoparticle's size and polydispersity 39
3.2.2 Zeta Potential 41
3.3 Evaluation of TrkB Phosphorylation 42
3.3.1 Immunocytochemistry 42
3.3.2 ELISA Sandwich with Direct Detection 46
3.3.3 Western Blot 48
3.4 Glutamate-induced Oxidative Stress 51
3.4.1 Quantification of SOD2 Expression 51
3.4.2 Quantification of ROS Production 56
3.6 Cellular Internalization of Polymeric Nanoparticles: TMC, TMC-PEG and TMC-PEG-LM22A1 57
4 Conclusion and Future Prospects 60
5 Bibliography 62
Annex 73

Figure Index

Figure 1. 1- Pathophysiology of Ischemic Stroke. Adapted [2] 2

Figure 1. 2- Ischemic Cascade. Adapted[18] 5

Figure 1. 3- Signaling pathway resulting from activation of the TrkB receptor by BDNF. Adapted [58] 10

Figure 1. 4- Structure of BDNF loop II and its mimetics. Adapted [62] 12

Figure 1. 5- Biogenesis of miRNA and examples of replacement and antagonistic therapies. Adapted[79] 15

Figure 1. 6- Quaternization reaction of chitosan amino groups, giving rise to N, N, N-trimethyl chitosan. Adapted[117] 21

Figure 2. 1- Schematic representation of the assembly of the ELISA assay set up. ... 29

Figure 3. 1- Schematic representation of the two-step synthesis reaction of TMC-PEG-LM22A1. A. Functionalization of TMC with the heterobifunctional N-hydroxysuccinimide-PEG-maleimide linker. B. Bioconjugation reaction of TMC-PEG-MAL copolymer with the LM22A1-Cys peptide. 37

Figure 3. 2- DLS analysis of TMC, TMC-PEG and TMC-PEG-LM22A1 nanoparticles with N/P ratio of 3,5 and10. A. Results of the Z-average (Mean hydrodynamic diameter, based on the size distribution by intensity). B. Polydispersity index. Data from n=3 independent experiments with triplicate measurements each. Asterisks represent statistically significant differences calculated from the two-way ANOVA test. (*** $p<0.01$, ** $p\leq0.01$, * $p\leq0.05$). 39

Figure 3. 3- Zeta potential analysis of TMC, TMC-PEG and TMC-PEG-LM22A1 polyplexes with N/P ratios of 3, 5 and 10, determined by DLS. Results from n= 2 independent experiments with triplicate measurements each. 41

Figure 3. 4- HT22-GFP cells non treated (NT), or treated with BDNF, LM22A4, LM22A1 and LM22A1-Cys. The left column shows the merged images with the EGFP signal (green; recombinant trKB receptors), DAPI (blue; nuclei) and alexa fluor 488 (red; phosphorylated TrkB receptors). The right column present the same images with the nuclei (blue) with phosphorylated TrkB receptors (red). The images were acquired by fluorescence microscopy. 43

Figure 3. 5-NCCC cells non treated (NT), or treated with: BDNF, LM22A4, LM22A1 and LM22A1-Cys. The left column exhibits the co-localization of ph-TrkB receptors

(red), nuclei (blue; nuclei) and β3-tubulin (turquoise). The right column presents the same images with the nuclei and the ph-TrkB receptors. The images were acquired by confocal microscopy. 45

Figure 3. 6- ELISA results for HT22-GFP cells non-treated or stimulated with BDNF or its mimetics: LM22A4, LM22A1, LM22A1-Cys. A. Absorbance values at 370 nm for the detection of the phosphorylated TrkB receptor. B. Fold-change of the TrkB receptor phosphorylation for each condition, calculated in relation to the NT cells absorbance value. Data from n=4 independent experiments with 2 to 4 technical replicates 46

Figure 3. 7- ELISA results for NCCC cells non-treated (NT) or stimulated with BDNF or its mimetics: LM22A4, LM22A1, LM22A1-Cys. A. Absorbance values at 370 nm for the detection of the phosphorylated TrkB receptor. B. Fold-change of the TrkB receptor phosphorylation for each condition, obtained in relation to NT cells. Data from n=4 independent experiments with 2 to 4 technical replicates. Asterisks represent statistically significant differences between treated versus NT cells (**, p≤0.01) 47

Figure 3. 8- Immunoblot analysis for HT22-GFP cells non treated (NT) or incubated with BDNF or LM22A4, LM22A1 and LM22A1-Cys compounds. A. Bands of the phosphorylated TrkB-receptor (170 kDa) and B. Quantified fold changes compared to NT cells. C. Phosphorylated ERK2 protein band and D. Quantification represented as fold variations. Data obtained from n=1 independent experiment. 48

Figure 3. 9 -Exemplificative Immunoblot analysis for NCCC cells cultured for 7 days in vitro, non-treated or incubated with BDNF or LM22A4, LM22A1 and LM22A1-Cys compounds. A. Detection of the phosphorylated TrkB receptor (140 kDa) and respective quantified fold changes compared to NT cells (B.). C. Identification of phosphorylated ERK2 protein and its signal quantification represented as fold variations (D.). Results obtained from n=2 independent experiments**.** 49

Figure 3. 10- Immunoblot analysis for NCCC cells cultured for 14 days in vitro, non-treated or incubated with BDNF or LM22A4, LM22A1 and LM22A1-Cys compounds. A. Detection of the phosphorylated TrkB receptor (140 kDa) and respective quantified fold changes compared to the untreated cells (B.). C. Identification of phosphorylated ERK2 protein and its signal quantification represented as fold variations (D.). Data from n=1 independent experiment**.** 50

Figure 3. 11 Standard curves for the evaluation of primers of the RT-qPCR reaction efficiency for SOD2 primers (A, B, C) and housekeeping genes (YHAWZ and HPRT). The values of efficiency and the respective coefficient of determination are located on top of each graph. Results obtained from CFX Maestro Software. 54

Figure 3. 12- Relative SOD2 expression in HT22-GFP cells not treated (NT) or treated with menadione (4 and 8μM) or glutamate (4,2,1,0,5,0.25 mM) for 24 hours, obtained by RT-qPCR. Two independent experiments were performed for stimuli with menadione (4 and 8μM) and 4 mM glutamate, each with 3 technical replicates. For the

remaining concentrations, an independent experiment was carried out with also 3 technical replicates. The data were processed using the $2^{-\Delta\Delta Cq}$ method. 55

Figure 3. 13- HT22-GFP cells treated with nanoparticles of TMC-PEG-LM22A1 complexed with microRNA Dy547 (12.5 nM), at N/P ratios of 5 and 10. The left column exhibit the co-localization of nuclei (blue), F-actin (green) and micro-RNA Dy547 (red). In the right column is presented the same images with the nuclei and micro-RNA Dy547 signal. Images were acquired by confocal microscopy..... 58

Figure 3. 14- HT22-GFP cells treated with nanoparticles of TMC-PEG complexed with microRNA Dy547 (12.5 nM), at N/P ratios of 5 and 10. The right column exhibit the co-localization of nuclei (blue), F-actin (green) and micro-RNA Dy547 (red). In the left column is presented the same images with the nuclei and micro-RNA Dy547 signal. Images obtained by confocal microscopy..... 59

Figure A. 1- ^{1}H-NMR Spectrum of TMC-PEG-MAL Polymer (D_2O; 400 MHz) 73

Figure A. 2- ^{1}H-NMR Spectrum of TMC-PEG-LM22A1 Polymer (DMSO; 600 MHz) ... 73

Figure A. 3- UV/ VIS spectra and respective chemical structures of the LM22A1, LM22A-Cys, TMC-PEG-LM22A1, TMC and TMC-PEG-MAL compounds..... 75

Figure A. 4- Total protein ponceau stained membrane blots of the experience with HTT22-GFP cells non- treated or incubated for 60 minutes with BDNF or LM22A4, LM22A1 and LM22A1-Cys compounds (A.) and respective total protein quantification relative to the control (NT) of the pink selected band (B.)..... 76

Figure A. 5- Total protein ponceau stained membrane blots of the experience with NCCC cells cultured during 7 days in vitro, non- treated or incubated for 60 minutes with BDNF or LM22A4, LM22A1 and LM22A1-Cys compounds (A.) and respective quantification relative to the control (NT) of a selected band (B.)..... 76

Figure A. 6- Second western blot experiment for NCCC cells cultured for 7 days in vitro, non-treated or incubated for 60 minutes with BDNF or LM22A4, LM22A1 and LM22A1-Cys compounds. A. Detection of the phosphorylated TrkB-receptor (140 kDa) and respective quantified fold changes compared to the untreated cells Although the membrane has a cut, an analysis of the same area per band was guaranteed. (B.). C. Identification of phosphorylated ERK2 protein and its signal quantification represented as fold variations (D.). Band inclination occurred and the lower band of the BDNF was analyzed in comparison with the others..... 77

Figure A. 7- Total protein ponceau stained membrane blots of the experience with NCCC cells cultured during 14 days in vitro, non- treated or incubated for 60 minutes

with BDNF or LM22A4, LM22A1 and LM22A1-Cys compounds (A.) and respective quantification relative to the control (NT) of a selected band (B.). 77

Figure A. 8- Histogram with FL1 and FL2 signal for cells treated for 24 hours with glutamate-0.25 mM (B03-purple), 0.5 mM (B02-pink), 1 mM (B01-dark green), 2 mM (A06-green) 4 mM (A05-orange) and respective controls with cells treated (A01-red) or not treated (A02-blue) with the DCFH2 -DA probe and fenton reagent (B05-turquoise). 78

Figure A. 9- Histogram with FL1 and FL2 signal for cells treated for 2 hours with glutamate- 1 mM (CO2-pink), 2 mM (CO1- dark green) 4 mM (B06-green) and respective controls with cells treated (A03-red) or not treated (A04-blue) and fenton reagent (B04-orange) with the DCFH2-DA probe. 79

Figure A. 10- HT22-GFP cells treated with nanoparticles of TMC-PEG complexed with microRNA Dy547 (25 nM), at N/P ratios of 5 and 10. The right column exhibit the co-localization of nuclei (blue), F-actin (green) and micro-RNA Dy547 (red). In the left column is presented the same images with the nuclei and micro-RNA Dy547 signal. Images obtained by confocal microscopy. 80

Figure A. 11- HT22-GFP cells treated with nanoparticles of TMC-PEG complexed with microRNA Dy547 (25 nM), at N/P ratios of 5 and 10. The right column exhibit the co-localization of nuclei (blue), F-actin (green) and micro-RNA Dy547 (red). In the left column is presented the same images with the nuclei and micro-RNA Dy547 signal. Images acquired by confocal microscopy. 81

Table Index

Table 2. 1- Sense (S) and antisense (AS) primers sequences and respective Melting Temperatures (T_m). 33

Table 2. 2- Thermal cycling conditions of the RT-PCR reaction. 34

Table A. 1- Maximum absorption wavelength and respective absorbances of LM22A1, LM22A1-Cys and TMC-PEG-LM22A1 compounds 74

Abbreviations, Acronyms and Symbols

^{1}H-NMR- Proton Nuclear Magnetic Resonance

AKT- Protein kinase B

ATP- Adenosine triphosphate

BBB- Blood-brain barrier

BCA- Bicinchoninic acid

BDNF - Brain-derived neurotrophic factor

BSA- Bovine serum albumin

Cq- Cycle threshold

DAPI- 4',6'-diamino-2-phenylindole

dH2O- Deionized water

DIV- Days in vitro

DLS- Dynamic Light Scattering

DMEM complete medium- Dulbecco's Modified Eagle's Medium supplemented with 10% Fetal Bovine Serum and 1% Penicillin/Streptomycin antibiotic

DMEM- Dulbecco's Modified Eagle's Medium

DMF- N, N-Dimethylformamide

DMSO-Dimethyl sulfoxide

ELISA- Enzyme-linked Immunosorbent Assay

ERK 1/2- Signal-regulated kinases 1 and 2

FACS- Fluorescence-activated Cell Sorting

FBS- Fetal Bovine Serum

HBSS- Hank's Balanced Salt Solution

HEPES - 4-(2-hydroxyethyl)-1-piperazineethanesulfonic acid

HEPES-Glucose buffer- 20 mM HEPES buffer with 5% (w/v) glucose, pH = 7.4

ICC- Immunocytochemistry

IFN-β- Interferon- β

LM22A1-Cys- mimetic LM22A1 modified with a cysteine

MAL- Maleimide

MAL-PEG-NHS- Maleimide- poly(ethylene)glycol-N-Hydroxysuccimide

m-BDNF- Mature form BDNF

miRNA- micro-RNA

mRNA- messenger RNA

MW-Molecular weight

N/P molar ratios- molar stoichiometry between the positive ammonium groups (N) and the negative phosphate groups

NBM complete medium- NBM supplemented with 2% SM1 (StemCell Technologies), 0.5 mM L- glutamine, 0.025 mM glutamate and 50 µg/ml gentamycin

NBM- Neurobasal medium

NCCC- Primary mouse neuronal cortical cell cultures

O/N- Overnight

P/S- Penicillin/Streptomycin antibiotic

PBS- Phosphate-buffered saline

PBS-T- PBS containing 0.05%(v/v) Tween®-20

PDI-Polydispersity index

PDL- Poly-D-lysine

PEG- Poly(ethylene) glycol

PEI- Polyethyleneimine

PFA- Paraformaldehyde

ph-ERK- Phosphorylated ERK protein

ph-TrkB- Phosphorylated TrkB receptor

PI3K- Phosphoinositide 3-kinase

pro-BDNF- precursor BDNF

R^2 - Coefficient of determination

RES- Reticuloendothelial system

RIPA- Radioimmunoprecipitation Buffer

ROS- Reactive oxygen species

rpm- Revolutions per minute

RT- qPCR- Reverse Transcriptase Quantitative Polymerase Chain Reaction

RT- Room temperature

SOD2 - Superoxide dismutase 2

TBS- 1x Tris-buffered saline

TBS-T- 1x Tris-buffered saline with 0.1% (v/v) Tween®-20

TMC- N,N,N-trimethyl chitosan

TMC-PEG- TMC-PEG-MAL

TrkB- Tropomyosin receptor kinase B

UV/Vis- Ultraviolet Visible Light

λmax- Wavelength at maximum absorbance

1.Introduction

1.1 Stroke

Stroke is the second leading cause of death worldwide after ischemic heart disease, with approximately 5.5 million deaths per year. According to the *World Stroke Organization*, it is estimated that 13.7 million new cases occur each year and that 1 in 4 adults will suffer from this condition during their lifetime.[1-3] Moreover, stroke is also associated with a high morbidity rate, with over 50% of survivors having chronic disabilities and needing medical care for the rest of their lives. This in turn creates an enormous financial pressure on the healthcare system. In accordance, from 1990 to 2016, approximately 51.9 million years of healthy lives were lost due to its high mortality and morbidity rate.[1,3-4] In Portugal, the scenario is significantly worse and stroke ranks as the first cause of death.

Over the past decade, there has been an increase in research on this topic and an overall rising interest in the scientific community in order to find therapies that are more effective. Despite this, its importance is still not emphasized enough, nor is there a marked public awareness about its symptoms and risks, which has a huge impact on patients' late arrival at the hospital with a concomitant decreased treatment effectiveness.[5-6] In addition, given its complexity, stroke has been a challenge in therapeutic terms, requiring more research both for the treatment of this condition in the hospital *per se*, and for the secondary treatment during the recovery phase.[7]

Stroke is a result of several vascular disorders that cause an acute dysfunction of the brain that persist for longer than 24 hours. [8-10] A stroke can be divided into haemorrhagic stroke and ischemic stroke. The haemorrhagic stroke, which is caused by a rupture of a cerebral blood vessel, can be divided into two subtypes according to the location where the haemorrhage occurs, which could happen intracerebrally or in the subarachnoid space. Although they are less common than ischemic stroke, haemorrhagic strokes are associated with a higher rate of mortality and disability. Ischemic stroke, in which a decreased blood flow in the brain occurs as a result of arterial obstruction, represents 80% of all strokes.[2,8]

1.2 The Ischemic Stroke

1.2.1 Pathophysiology of Ischemic Stroke

An ischemic stroke is the result of the occlusion of a cerebral artery, caused by a thrombus formed in the brain arteries or by cardioembolism; after large artery atherosclerosis, in which plaque ruptures due to inflammatory processes, resulting in embolization. Small vessel disease, mainly lipohyalinosis, in which the vessel wall narrows and the diameter of small arteries and arterioles decreases can also be a cause.[2,10-11]

There are several factors that increase the risk of stroke, such as old age, hypertension, diabetes mellitus, heart and cardiovascular diseases, blood cholesterol, obesity among others.[2-3] Although the risk of stroke increases exponentially with age, there has been an increase in the incidence of ischemic stroke in the younger population, possibly due to an increase in sedentary life, drug use and stress.[12]

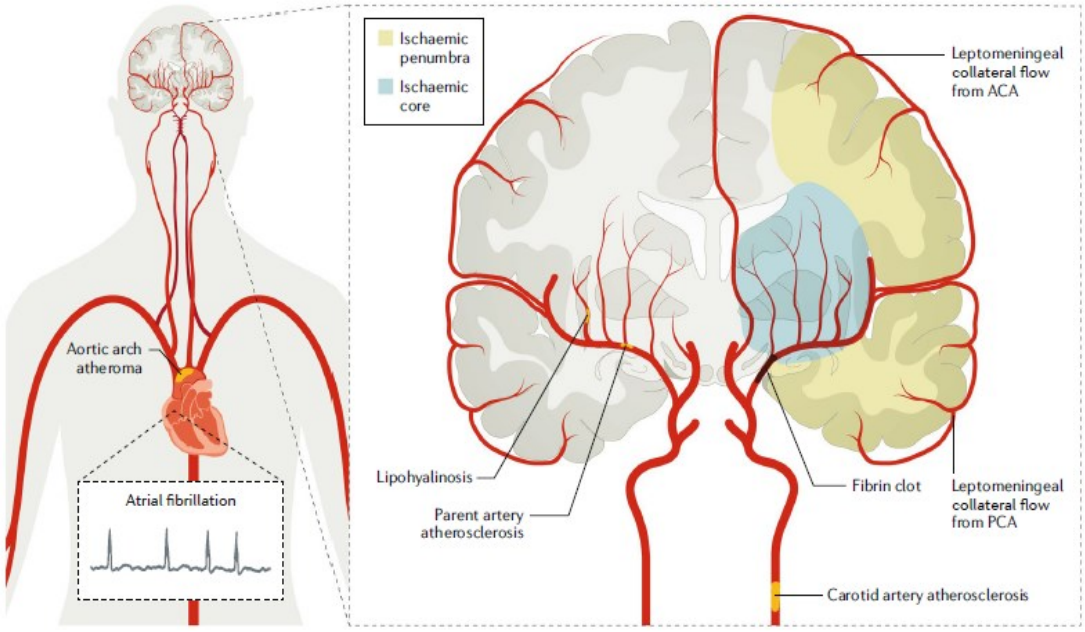

Figure 1. 1- Pathophysiology of Ischemic Stroke. Adapted [2]

Following an occlusion of a major cerebral artery, there is a decrease of blood flow in a specific area of the brain. Both the cerebral flow reduction and the pathophysiological changes in the tissue are heterogenous. Usually, in the centre of ischemic region there is a more severe reduction of blood flow and the tissue is irreversibly damaged. Therefore, this region, often called ischemic core, is considered to be the epicenter of brain ischemia.[2,13-14]

On the other hand, in the region surrounding the ischemic core, defined as ischemic penumbra, a residual level of perfusion is maintained due to the supply of blood flow by collateral blood vessels from non-ischemic regions. For this reason, brain tissue remains viable and can potentially be salvaged for variable period of time, despite being at a state of hypoxia and physiologically non-functional. The penumbra undergoes a dynamic process, where it suffers irreversible damage over time and a progressive reduction of its size.[2,9,13] This is the region that needs to be protected, so it does not turn into core region. It is important to note that resistance to ischemic damage is dependent on several factors such as the duration of artery occlusion, location of vascular lesion, anatomy of vasculature and extent of blood flow reduction.[9,13,15]

1.2.2 Molecular Mechanisms of Ischemic Stroke

Ischemic damage is the result of a sequence of complex and multifactorial molecular events, also known as the ischemic cascade. Under normal conditions, the brain requires high amounts of energy and depends almost exclusively on oxidative phosphorylation to produce the ATP needed to maintain the intracellular homeostasis and the membrane potential.[6,14,16] The brain by itself is already very susceptible to oxidative stress, due to its high oxygen consumption (20-25% of the body's oxygen consumption) and its increased reactive oxygen species (ROS) production when compared to other peripheral organs. It has relatively weak antioxidant mechanisms (low levels of catalase and glutathione peroxidase), high concentration of iron (catalyses the production of free radicals) and high content of unsaturated fatty acids which, in turn, easily undergo lipid peroxidation.[17]

In brain ischemia, cerebral perfusion decreases to such a level that the oxygen and glucose reaching the cells becomes insufficient to maintain oxidative phosphorylation. As glucose is the only source of energy in neuronal cells, a metabolic transition to anaerobic glycolysis occurs in order to maintain the production of ATP. However, the yielded ATP is low and an excess of lactic acid production occurs, causing intracellular acidosis. Such an energetic impairment leads to failure of cellular ionic pumps, such as sodium potassium-ATPase and a consequent increase in the concentration of extracellular K^+ and the influx of Na^+, Ca^{2+} and Cl^- into the intracellular medium. This disruption of transmembrane ionic gradients triggers the membrane depolarization of neurons and glial cells.[6,18-19]

Furthermore, anoxic depolarization results in the release of excitatory neurotransmitters, particularly glutamate. Under physiological conditions, glutamate is involved in several cognitive functions and its extracellular concentration is low due to

energy-dependent clearance mechanisms. In situations of ischemic stroke, the decrease in glutamate uptake along with the increasing exocytosis of glutamate vesicles from presynaptic terminals (presynaptic glutamate release) results in the accumulation of glutamate in the synaptic cleft. This causes the excessive activation of glutamate receptors which in turn provokes dysfunction and cell death by a destructive metabolic pathway referred as excitotoxicity.

Glutamate activates several types of post-synaptic receptors that are involved in the excitotoxicity mechanism, with NMDA ionotropic receptors being the most relevant. These receptors are selective for cations (Na^+, Ca^{2+} and K^+), having a higher permeability for the Ca^{2+} ions, leading to an overload of Ca^{2+} and K^+ in the intracellular medium. [16,18-19]

Due to the intracellular accumulation of ions (the influx of Na^+, Cl^- and Ca^{2+} is higher than the efflux of K^+), water moves from the extracellular to the intracellular medium to maintain osmotic equilibrium. As a result, swelling of neurons, endothelial cells and glial cells occurs, which constitutes the driving force in the formation of cerebral edema, vascular compression and herniation.[14,20]

The massive influx of Ca^{2+} resulting from the activation of glutamate receptors, has a severe impact on neuronal cells and leads to the activation of several molecular cascades including:

1) **The activation of digestive enzymes** such as proteases, nucleases and lipases that lead to the degeneration of intra and extracellular components;[6]

2) **Conversion of xanthine dehydrogenase to xanthine oxidase**. Following the decrease in the ATP production in ischemic stroke, there is an increase in the levels of AMP, which is metabolized to hypoxanthine. In turn, this product is converted to xanthine and uric acid by the enzyme xanthine oxidoreductase. This enzyme is composed by two interconvertible forms, xanthine dehydrogenase and xanthine oxidase, and only the latter has a high affinity for oxygen and catalyses the formation of the superoxide radicals;[19,21-22]

3) **Activation of phospholipase A2 and cyclooxygenase**. Both enzymes produce ROS and are involved in the metabolism of arachidonic acid. The phospholipase A2 enzyme is responsible for the cleavage of fatty acids and the consequent release of arachidonic acid, which is later converted into prostaglandins and thromboxanes by cyclooxygenase;[6,22-23]

4) **Activation calmodulin-dependent neuronal and endothelial nitric oxide synthases**. The overproduction of NO has a harmful effect on cells, since this molecule is thermodynamically unstable and combines with superoxide anions generating

peroxynitrite anions, which have a strong oxidizing power and cause protein oxidation and nitridation, breaking the DNA, among other processes.[6,14,19]

The decrease in oxygen availability in the cells and the absorption of Ca^{2+} by mitochondria, in an attempt to lower its levels in the cytosol, causes depolarization across the inner mitochondrial membrane, resulting in the decoupling of the electron transport respiratory chain and the exacerbated production of ROS, such as the superoxide anion, hydrogen peroxide and the hydroxyl radical.[6,16,19]

It is recognized that there is an attempt to lower ROS levels by enzymatic and non-enzymatic antioxidant defences such as superoxide dismutase, catalase, glutathione peroxidase, alpha-tocopherol, ascorbic acid, glutathione, among others.[22] However, when the blood flow is restored, a greater overproduction of ROS occurs, overwhelming the antioxidant defences and leading to an exacerbated increase in oxidative stress. Despite of this, as an overall balance, reperfusion has beneficial effects.[14,24]

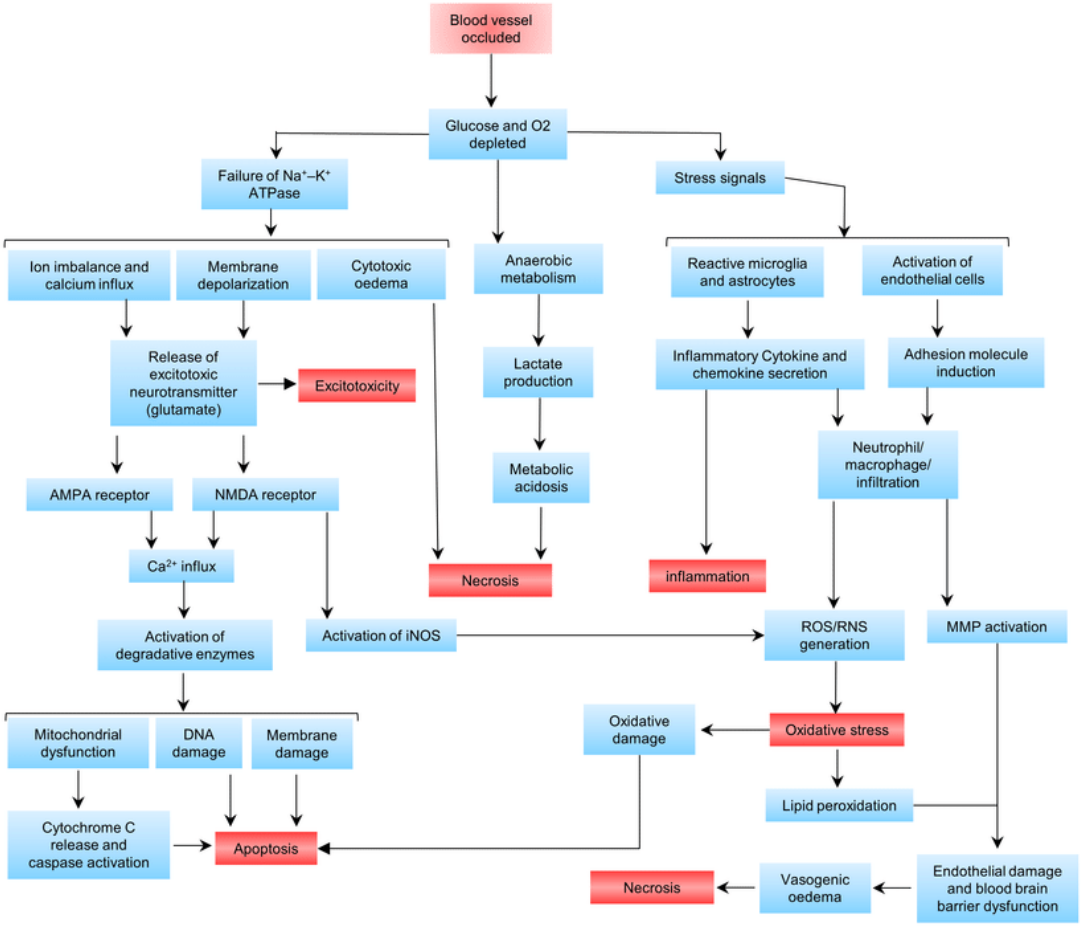

Figure 1. 2- Ischemic Cascade. Adapted[18]

Hypoxia also triggers an inflammatory response. Microglia cells and astrocytes are activated and lead to the production of inflammatory mediators such as cytokines,

chemokines, metalloproteins and ROS via NADPH oxidase, iNOS and cyclooxygenases.[16,25] In turn, metalloproteins and reactive oxygen species promote the disruption of blood-brain barrier (BBB) tight junctions that results in their increased permeability minutes after stroke. After several hours, the release of cytokines from cells and ROS will lead to the recruitment of leukocytes from blood vessels, which will adhere to the BBB wall and will contribute to its severe disruption through the production of neurotoxic factors. Thus, there is an even greater increase in BBB permeability and the transmigration of immune system cells from blood vessels to the brain parenchyma occurs, which leads to an exacerbated inflammatory response, and consequently to a more significant degree of brain damage.[25-28]

All the mechanisms described above ultimately results in cell death due to apoptosis or necrosis, depending on the severity and location of the injury, the occurrence of reperfusion, the type of cells affected and their stage in the life cycle.[29-30] Typically, in the ischemic core, occurs immediate cell death by necrosis due to the severe decrease in blood flow, whereas in the penumbra cell death occurs mainly by apoptosis, hours or days after acute brain ischemia.[6,18,30]

1.2.3 Current Treatments for Ischemic Stroke

The current clinical treatment of ischemic stroke is the salvation of the penumbra tissue and is based on the restoration of the blood flow to the ischemic area (reperfusion) through the dissolution of the arterial occlusion. There are two types of therapies implemented, intravenous thrombolysis and mechanical thrombectomy, that lead to the breakdown of thrombi by pharmacological or mechanical approaches, respectively.[2,13]

Intravenous thrombolysis with alteplase (recombinant tissue plasminogen activator) is the only pharmacological treatment approved by the FDA.[2] Alteplase is a protease that promotes the activation and conversion of plasminogen to plasmin, which in turn is a proteolytic enzyme that promotes the disruption of fibrin cross-links responsible for clot cohesion.[31-32] This enzyme acts mainly in the blood clot due to its high affinity for fibrin, which explains the fact that it does not induce a systemic plasminogen activation. Treatment with alteplase also has its drawbacks, such an increased risk of haemorrhage and the fact that it has a short therapeutic time window (3-4.5 h after symptom onset), being estimated that around 95-98% of patients cannot benefit from this treatment.[33] Due to the fact that it increases the risk of haemorrhage, this therapy is prohibited for patients with severe strokes, severe hyperglycemia, hypertension, head trauma and have undergone recent surgery.[5,34]

Alternatively, mechanical thrombectomy corresponds to a set of techniques used to remove the blood clots, using mechanical tools such as coil retrievers and aspiration devices.[2,13,35] This treatment has numerous advantages such as a broader therapeutic window (6-18 h after symptom onset), faster restoration of blood flow (especially if the blood clot is highly resistant to enzymatic degeneration) and it can be used as an adjunct to intravenous thrombolysis and increase the surface area accessible for alteplase.[2,6,13] However, mechanical thrombectomy is only recommended for large vessels occlusions, it can cause vascular damage and the circulation of mechanical devices can be difficult in the intracranial vasculature.[13,36]

It is estimated that 1 to 2 million of neurons die per each minute if reperfusion techniques are not administered, which makes time the worst enemy of ischemic stroke.[8,13,16] However, reperfusion therapies cannot be conducted for all patients due to their adverse side effects and, especially, for exceeding their therapeutic time window. The main reason for this, is the delayed hospitalization of the patient that may be the result of low public awareness of the symptoms, delays in emergency transportation and uncertainty about the onset of symptoms. Ischemic strokes follow a circadian pattern and occurs most often in the early morning. Thus, about 16 to 20% of patients already wake up with the symptoms of a stroke, failing to identify the exact time it occurred. [33,37-39]

Therefore, in addition to the techniques of reperfusion, it is important to develop alternative therapies that act on the cerebral parenchyma and directly prevent the damage resulting from the ischemic cascade. Hence, when used in conjunction with reperfusion techniques, these neuroprotective strategies can fill their gaps, reduce the deleterious effect of time and enhance their action, in order to minimize the death and disability of ischemic stroke patients.[40-42]

1.3 Neuroprotective Approaches

In the context of ischemic stroke, neuroprotective strategies aim to rescue the penumbra area and reduce the volume of the injury extension, through direct targeting of the cerebral parenchyma and antagonization of key ischemic events. Taking this definition into consideration, reperfusion approaches that act on the cerebral vasculature and have an indirect neuroprotective effect, are not considered neuroprotective strategies. [41,43]

For the development of neuroprotective therapies it is imperative to have a profound insight of the pathophysiology and dynamics of cerebral ischemia, the molecular events of the ischemic cascade and the endogenous neuroprotective

mechanisms stimulated in response to a stroke in an attempt to protect against injury.[41,44] Over the years, pharmacological and non-pharmacological neuroprotective therapies have been developed with the intent of modulating the inflammatory response, oxidative stress, cytotoxicity and cell death caused by ischemic stroke.[40,44-45] Pharmacological neuroprotective agents include ion channel blockers, glutamate receptor antagonists, free radical scavengers, calcium chelators, growth factors, anti-inflammatory agents, enzyme inhibitors, among others.[40,45-46]Some examples of non-pharmacological strategies correspond to hypothermia, hyperbaric therapy, photobiostimulation and gene and stem cells therapies.[40,47-48]

Although there is a wide range of neuroprotective agents that have proven to be effective in various animal models of ischemic stroke, none has been successful in clinical trials.[42-43,45] One of the possible reasons may be the lack of methodological rigor in some animal experiments that can lead to overestimated results in the effectiveness of neuroprotective therapy. In many of the animal studies the selected population is homogeneous, being mostly composed of healthy young male adults. However, these conditions are contrasting to those that occur in humans, since the risk of ischemic stroke and its associated morbidity and mortality are increased in older patients. Most of these patients also have other pathologies that must be taken into account, whose medication can influence the outcome of the neuroprotective therapy.[41-42,45]

Furthermore, *in vivo* models are unable to fully represent the human ischemic stroke due to its complexity, its spontaneous nature and the heterogeneity of atheologies.[41-42] There are also discrepancies between humans and other species regarding the composition, structural and functional organization of the brain, as well as its vascular anatomy.[49]

In addition, since *in vivo* trials are highly controllable, therapies are usually administered over a short time window or through a single dose, before or after stoke induction. Thus, in many cases, the administration and monitorization of treatment is not performed in long-term.[41,50] The effectiveness of neuroprotective therapy is assessed by analyzing the reduction of the infarction volume, which can be an unreliable method since different locations of the infarction have different relevance in the functional outcome. In contrast, in clinical trials the evaluation is performed after 3 to 6 months by functional improvement.[41-42,50] Many of the studied neuroprotective agents have a short therapeutic window, which is one the major problems of reperfusion approaches.[42]

Another factor that is involved in the failure of clinical trials is the fact that most neuroprotective therapies act against a single target in the ischemic cascade, which may not be sufficient to suppress the damage. However, it is important to take into consideration the temporal profile of the therapeutic intervention, since there are

detrimental mechanisms in the acute phase of the stroke that are fundamental in long-term repair.[41,43]

It is also important to have studies focused in the concurrent use of the reperfusion and neuroprotective approaches. The former approach allows an increase in neuroprotective agents' bioavailability at the damage site, and the latter provides protection against the damage cause by the reperfusion itself. For patients not eligible for the techniques of reperfusion, neuroprotection can be an alternative, reaching the damage site through the secondary vasculature.[41,43 51-52]

In the next section, some promising neuroprotective strategies will be described.

1.3.1 Neuroprotective effect of BDNF

The Brain-derived Neurotrophic Factor (BDNF) is the most expressed neurotrophin in the brain (especially in the cortex and hippocampus), playing a pivotal role in its development and homeostatic maintenance. Neurons are the major producers of this neurotrophin, but it can also be expressed in non-neuronal cells such as astrocytes, glial and endothelial cells or even in peripheral tissues.[51-52]

This neurotrophin is synthesized as a precursor (pro-BDNF) which can subsequently be cleaved intracellularly in trans Golgi network or secretory vesicles, resulting in the mature form of BDNF (m-BDNF). [53-54] In neurons, both forms of BDNF are secreted constitutively or in an activity-dependent manner through neuronal depolarization and Ca^{2+} influx. Additionally, at the extracellular level, the cleavage of pro-BDNF form can also occur by matrix metalloproteases and plasmin.[51]

The BDNF pro-form binds with high affinity to p75 neurotrophin receptors and sortilin receptors, which are involved in cell death by apoptosis and pain promoting effects. Furthermore, the mature form of BDNF has high affinity for tropomyosin receptor kinase B receptors (TrkB) and low affinity for p75 receptors. The TrkB receptors are widely distributed in the brain and its binding to BDNF promotes its dimerization and autophosphorylation of tyrosines in its cytoplasmic portion. This leads to the activation of several adapter proteins, which in turn induce the activation of the PI3K/AKT, MAPK/ERK signaling pathways, involved in neuronal survival, differentiation and synaptic plasticity.[51,53-54] The ratio between pro-BDNF and m-BDNF varies according to the stage of development. In adults, the m-BDNF form is predominant, which is advantageous given the opposite effects of the BDNF forms.[55] It has been shown in animal models that there is an increase in BDNF levels in the brain after ischemic stroke, especially in the penumbra area, and its knockdown is related to a greater volume of infarct. [56-57] On the other hand, in epidemiological studies it is also found that the levels

of circulating BDNF are lower in ischemic stroke victims when compared to healthy individuals and there is a correlation between low levels of circulatory BDNF and worse post-stroke outcomes.[58-59]

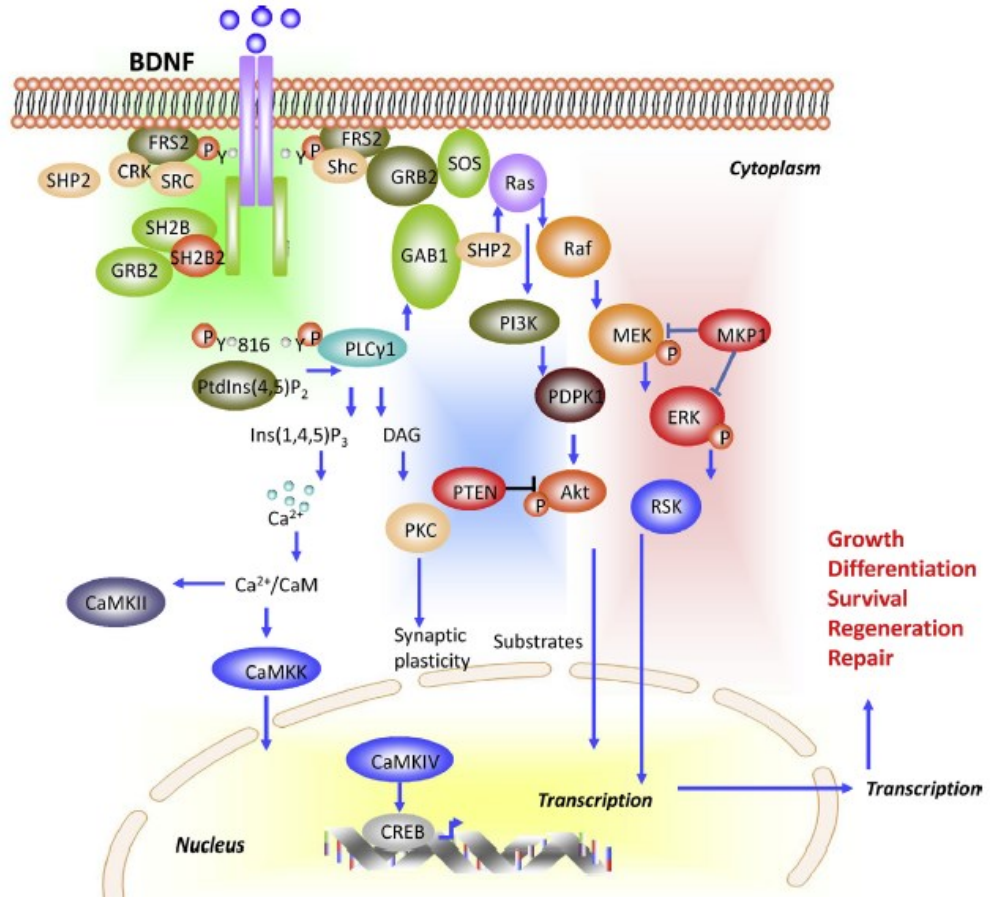

Figure 1. 3- Signaling pathway resulting from activation of the TrkB receptor by BDNF. Adapted [58]

Despite that this evidence suggests that BDNF may be a promising neuroprotective agent, this neurotrophin has not yet been approved for clinical use. Therapy with this neurotrophin was proven to be a failure in clinical trials, mostly due to pharmacokinetic and structural problems and the complexity of signaling pathways.[52,56] BDNF size, charge and hydrophilicity, lead to a short-life time (less than 10 minutes) and a low penetration in the BBB (even if disrupted as occurs during stroke) and in the cerebral parenchyma, which makes direct administration of BDNF challenging, both intravenously and intracranially. Thus, it is necessary to administer high amounts of BDNF in order to reach the therapeutic dose at the damage site.[60]

To increase the bioavailability of BDNF at the site of damage, several strategies have been developed that stimulate its endogenous production, such as the administration of drugs such as lithium, gene therapy, stem cell transplantation and

epigenetic manipulation. Alternatively, the transport of BDNF mediated by nanoparticles via systemic or intranasal administration has also been studied, which allows the use of lower concentrations of this neurotrophin and an efficient passage through BBB.[55-56,61] In ischemic stroke models, many of these approaches have resulted in beneficial effects such as mitigation of cell death, resistance to glutamate cytotoxicity, improved recovery of cognitive and motor functions and increased neurite outgrow, neuronal regeneration and neuroplasticity. [52,56,58]

Although BDNF binds with low affinity to the p75 receptor, this also constitutes a disadvantage to therapy with this neurotrophin and may therefore be involved in side effects such as pain promoting effects and cell death.[52,58] To overcome the non-selectivity of BDNF, there was an emphasis in the study of TrkB agonists with more advantageous characteristics such as low molecular weight and specificity for the TrkB receptor, with neuroprotective effects comparable to BDNF. There are a plethora of small molecules agonists under investigation, including natural compounds (7,8-DHF, deoxygedunin**)**, TrkB agonistic antibodies and compounds discovered through *in silico* methods.[52,56,58]

One of the most promising strategies is the production of mimetics based on BDNF loop II, involved in interaction with the TrkB receptor by studies of oligonucleotide site-directed mutagenesis and biological activity assays. Through the *in silico* screening of a library of compounds based on this structure, followed by *in vitro* neurotrophic activity assays, it was possible to select four promising compounds (LM22A1 to LM22A4), whose structure is shown in **Figure 1.4**. These mimetics have different chemical structures, with LM22A1 being a tripeptide (Pro-His-Trp), while the compounds LM22A2 to LM22A4 have no peptide bonds. All these mimetics exhibit specificity for the TrkB receptor, not promoting activation of other Trk family receptors or p75 receptors. Although there are differences in the activation kinetics of receptors when compared to BDNF, these compounds promote activation of the PI3K/AKT and MAPK/ ERK pathways and neuronal survival *in vitro*, with an efficiency comparable to BDNF. In addition, *in vivo* studies have shown that the intranasal administration of mimetic LM22A4 results in increased activation of the TrkB receptor and AKT and ERK enzymes in the hippocampal and striatal tissue. It is also theorized that this mimetic is associated with an improvement in cognitive function, since it has been verified in an animal model of traumatic brain injury that its administration results in an increase in motor performance.[62] This mimetic is also involved in the activation of the TrkB /AkT /ERK signaling pathways in non-neuronal cells, being associated, for example, with an increase in remyelination and oligodendroglial density, which are also compromised in the context of ischemic stroke. [63-64]

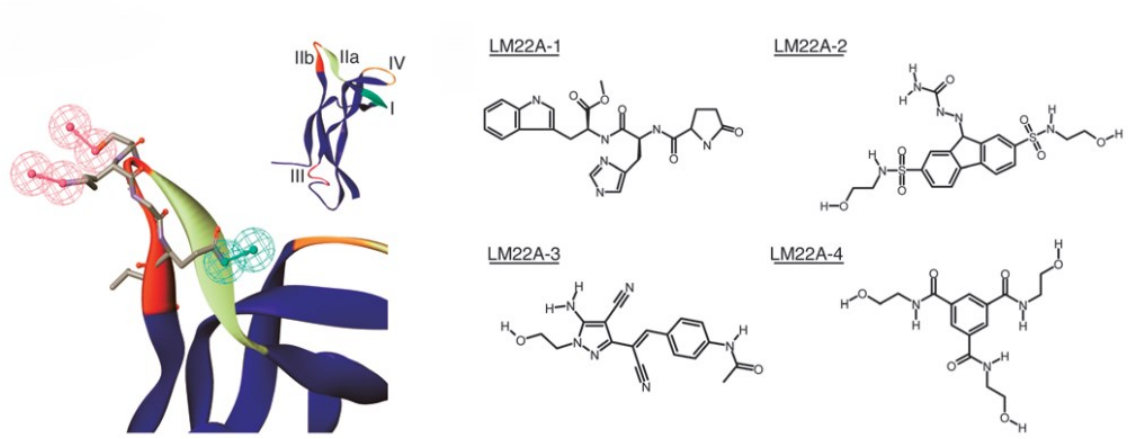

Figure 1. 4- Structure of BDNF loop II and its mimetics. Adapted [62]

1.4 Epigenetic Modifications in Ischemic Stroke: miRNA-145

When ischemic stroke occurs, it is accompanied by a deregulation of the epigenetic process, such as a significant alteration the DNA's methylation pattern, covalent modification of histones and alteration in the micro-RNA (miRNA) levels. All these factors are spatially and temporally dependent. Knowing which epigenetic mechanisms were altered in ischemic stroke allows the discovery of new therapeutical molecular targets to combat its effects. From the alterations previously mentioned, emphasis has been put in the miRNA pattern of alterations present in ischemic stroke.[65-67]

The process of biogenesis of miRNAs involves multiple steps. Usually, miRNA genes are found mostly in introns from intergenic regions or from protein coding genes and are transcribed by RNA-polymerase in the form of mono or polycistronic primary miRNA transcripts, encoding a single miRNA or several, respectively. [68]These primary miRNA (pri-miRNA) transcripts acquire a secondary structure when folding into a steam loop structure to form a hairpin structure and are recognized and cleaved by a complex microprocessor consisting of an RNase III enzyme Drosha and the cofactor DGCR8/Pasha. This complex is responsible for the asymmetric cleavage of both strands of the pri-miRNA near the base of the harpin, leading to the formation of what generates a miRNA precursor (pre-miRNA) with 60-80 nucleotides. The pre-miRNA is translocated from the nucleus to the cytoplasm through exportin 5 in which its terminal loop is cleaved by the cytoplasmatic RNase III dicer, originating a double stranded miRNA .This duplex miRNA is incorporated into the RNA inducing silencing complex (RISC) and the two strands separate, with the guide strand being retained in the complex, while the passenger strand is normally discarded.[68-70] The selection of the chain retained in the

complex is based on the thermodynamic stability of the 5’ ends of each chain, with the guide chain presenting a less stable 5’ end. In this way, the guide strand corresponds to the mature miRNA and gives the target specificity to the RISC complex directs the complex to the target through the base pairing of its seed region to the 3' UTR of the mRNAs. If there is total complementarity between these two sequences, the RISC complex mediates the degradation of the messenger RNA mRNA, whereas for partial complementarity the repression is achieved through the repression of translation and acceleration of the degradation through the destabilization of the mRNA structure.[70]

MiRNAs are found at high levels and have high activity in the human brain (about 70% of all known miRNAs are found in the brain), being central to their development and normal functioning.[71] Changes occur in its expression signature during its development and normal physiological functioning, as well as in pathological processes. After the onset of the ischemic stroke, there is an immediate deregulation of the expression pattern of the miRNA transcriptome, which extends over time. miRNAs provide additional complexity in understanding the ischemic cascade, as their levels vary according to the stroke's temporal profile, brain zone and cell type.[72] Dozens of miRNAs have been identified whose expression in brain tissue is increased or decreased along ischemic stroke, are implicated in pathogenic processes such as excitotoxicity, oxidative stress, inflammation and cell death. However, this change in the expression profile does not only translate into harmful effects as there are also miRNAs that alter the expression of its target genes in order to promote neuroprotection and angiogenesis.[72-74]

The miRNA-145 plays a fundamental role in the pathology of the ischemic stroke, being identified as a potential therapeutic target in neuroprotective approaches. In studies with rodents, it was found that this miRNA is significantly upregulated following focal ischemia, and that this change is maintained for days. It has also been shown that this miRNA has as molecular target SOD2 enzyme, inhibiting its protein expression after the ischemic stroke.[75]

The superoxide dismutase 2 (SOD2) is an antioxidant enzyme located in the mitochondrial matrix, responsible for the conversion of superoxide into H_2O_2 and H_2O. This enzyme is highly expressed in neuronal cells and is one of the first lines of defense against oxidative stress.[76] As oxidative stress is one of the hallmarks of cerebral ischemia and it has been proven that deficiency in SOD2 exacerbates brain injury, the inhibition of miRNA-145 in order to restore SOD2 levels, it could constitute a promising neuroprotective strategy. In fact, in the same study it was found that the application of an antagomir strategy against miRNA-145 resulted in a significant increase in the levels of SOD2 in neurons located in the penumbra area, as well as in the reduction of infarction.[75]

MiRNA-145 also presents other molecular targets, being demonstrated that in human monocytes-derived macrophages it contributes to the silencing of the expression of the Interferon-β (IFN-β) cytokine.[77] This cytokine is involved in a range of anti-inflammatory processes. As the ischemic stroke is also characterized by pathological neuroinflammation, its modulation through inhibition of miRNA-145 may also have therapeutic value. In this sense, it has been demonstrated in animal models of cerebral ischemia, that IFN-β treatment results in positive outcomes such as decreased volume of infarction and neurological deficit, attenuation of the release of inflammatory mediators, activation of microglia cells and recruitment of immune cells in the affected area, suppression of metalloprotein expression and consequent improvement in BBB integrity.[78]

1.5 MiRNAs-based gene-therapies

Taking into account the alterations in miRNA expression during ischemic stroke, the miRNA-based therapies can present an opportunity to modulate the pathological pathways associated with stroke and thus improve the clinical outcome. In these therapies two distinct strategies can be adopted: correction of miRNA alterations through the administration of nucleic acid-like molecules which can work as mimetics and restore the miRNA function; or the use of said mimetics to repress miRNA expression.[79]

The replacement approach with miRNA mimetics has the goal of reestablishing the biological function of the endogenous miRNA that has been downregulated. These mimetics are normally composed by two chains (double-stranded), with a guide chain similar to mature miRNA and a passenger chain with chemical modifications that will allow it to be incorporated in the RISC complex and also improve the pharmacokinetic of the duplex and the cellular uptake. The mimetics do not require processing, being directly incorporated in the RISC complex, and mediate the target mRNA's repression through mechanism endogenous to the cell.[70,79]

In contrast, the miRNA antagonists have complementary sequences to the guide strand of the target miRNA, thus preventing its interaction with the RISC complex. In this way, inhibition does not occur, the mRNA is not destroyed, and the biological component of interest is restored. One example of miRNA antagonist compounds are the antagomirs, which are designed to specifically interact with a single miRNA. These oligonucleotides are commonly modified with 3'-cholesterol e 2'-methoxy groups to increase their binding stability to the target miRNA, thus preventing nuclease mediated degradation. It is important to consider that this therapy might affect other mRNAs given the promiscuous nature of the miRNA. There are also other antagonists such as the RNA

sponges that interact with multiple miRNAs through the same seed region and miRNA-masks that bind to the 3'UTR of the mRNA, preventing the binding and repression of the target miRNA.[79-82]

Despite these miRNAs being subject of chemical modification to improve their stability in a biological medium, it is not enough and is not specific for the target cells which is an important factor for their possible incorporation into vectors.[83]

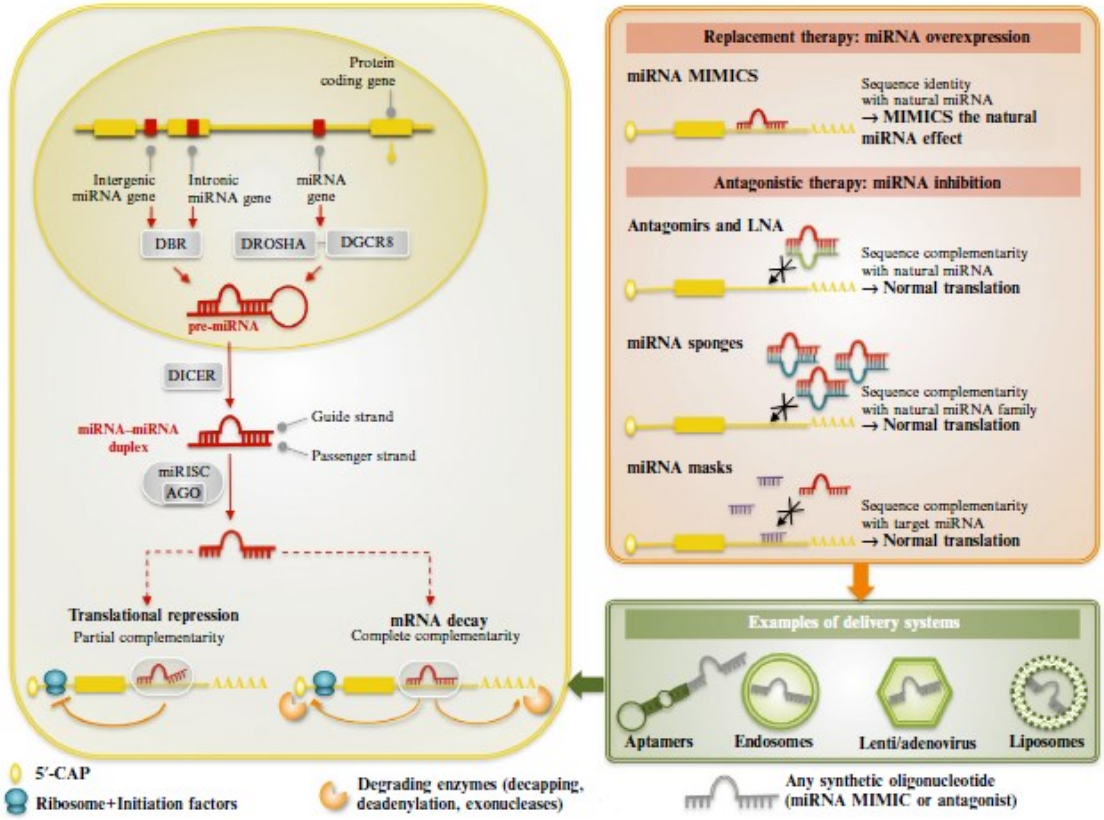

Figure 1. 5- Biogenesis of miRNA and examples of replacement and antagonistic therapies. Adapted[79]

1.6 Viral and non-viral delivery vectors in Gene Therapy

One the biggest challenges in modern therapy is the efficient delivery of biological cargo to a specific body tissue. The use of delivery vectors allows to mitigate conventional problems associated with drug delivery thus contributing to the improvement of multiple innovative therapeutical strategies such as gene therapy.[84-85] The delivery vectors used in gene therapy can be classified as viral or non-viral.

The innate characteristics of viruses, such as their nanometric size, their ability to cross biological barriers, to invade host cells, to escape the endosomal compartment and to hijack the cellular machinery makes viruses an appealing target for gene therapy delivery systems. The most common types of viral vectors used included retrovirus, adenovirus, adeno-associated virus, herpes simplex and lentivirus. Viral vectors have

the highest values of transfection efficiency, which explains why they are the most used vectors in gene therapy clinical trials. However, not many viral vector-based gene therapies have been approved and this type of vectors still remain controversial mainly due to safety concerns. Viral vectors present numerous limitations since they can trigger immunogenic and inflammatory responses, are cytotoxic, can suffer recombination with wild viruses and can sometimes have broad tropism. There are logistic issues as to their large scale production and they also possess a limited nucleic acid packaging capacity. For genome integrating virus there are additional limitations such as the possibility of insertional mutagenesis which can lead to carcinogenic events.[86-88]

In contrast, non-viral vectors also have attractive characteristics for drug delivery applications such a better safety profile, ease of production in large scale and an unlimited payload. However, they do not possess such a good ability of crossing cellular barriers as viral vectors do. This translates into pharmacokinetic problems which can then result in low bioavailability at the target site, low cellular uptake and, consequently, small transfection efficiency. However, their physicochemical properties can easily be tailored to improve their biological effect. The most common non-viral vectors are polymers, lipids and dendrimers.[86,89-90] Some vectors have the advantage of being stimuli sensitive responding to the biological environment, to magnetic fields and radiation. Additionally, these vectors have the ability of being tracked through optical imaging.[91] The non-viral vectors used in gene delivery are usually positively charged and when complexed with nucleic acids are designated as dendriplexes, polyplexes and lipoplexes, respectively.[90]

1.7 Biological barriers and non-viral vector design

Non-viral vectors have a lower delivery efficiency when compared to their viral counterparts, mostly due to their difficulties in crossing the biological barriers whether these are intra or extracellular. As such, to optimize non-viral gene delivery it is important to have a rational and innovative design for these vectors which must be tailored to the therapeutical parameters such as the chosen administration route, the targeted cells and the cargo. The physicochemical properties of these vectors such as size, morphology, hydrophobicity, cargo density and functional groups can be tuned so as to cross any challenges that might present before delivery.[86,92-94]

The compatibility between the nanocarriers and the biological milieu of the human body is an important factor to consider. When the nanoparticles contact with biofluids, like lymph, blood, interstitial fluid and cytoplasm, their surface is immediately covered by adsorbed biomolecules (proteins, lipids, sugars, among others). These biomolecules

create a dynamic layer designated as protein corona. The presence of the protein corona alters the intrinsic properties of nanoparticles and provides them with a new biological identity which has a profound impact in the nanoparticle's interaction with the immune system, stability, toxicity, bioavailability, and cellular recognition which in turn affects cellular uptake and interactions.[95-97] In the case of systemic administration, positive and hydrophobic nanoparticles are strongly absorbed by polyanionic blood proteins, such as serum albumin, that act as opsonins that can ultimately lead to the formation of large aggregates which are captured by the reticuloendothelial system (RES) composed by highly phagocytic cells. As a result, the nanoparticle's might not be able to reach the target in a therapeutically effective dosage.[88,98] A strategy to resolve this problem consists in the modification of the nanocarrier's surface through functionalization with non-ionic hydrophilic molecules which shield the positive charges found at the nanoparticle's surface such as the binding of a molecule of poly(ethylene) glycol (PEG). This hinders the adsorption of biological components, the formation of the protein corona, it shields from the immune system and prevents nanoparticle aggregation, which translates in increased stability and circulation time.[99]

The nanoparticle's size also strongly impacts their pharmacokinetic properties such as cellular uptake, circulation time and renal clearance. Small nanoparticles are quickly eliminated through glomerular filtration, while large nanoparticles can accumulate in specific organs such as the liver or spleen which could lead to chronic toxicity if these particles are not biodegradable.[88,93]

Another factor that significantly affects the biological performance of these systems is the bioavailability of the nanocarriers and their lack of target specificity. Therefore, there is a great interest in the exploration of target moieties that can be incorporated in the nanoparticles allowing a targeted delivery. The target ligands can include proteins, peptides, nucleic acids, antibodies, carbohydrates, among others. Besides adequate selection after thoroughly analyzing ligands characteristics, it is also necessary to chemically modify the nanoparticle's surface in order to attach the ligands. An optimized system would use a targeting molecule that also has therapeutical effect.[86,100]

Neurons are one of the most challenging cells for targeted delivery, which is not only due to the highly impermeable BBB, which impedes the passage of particles to the brain, but also due to morphological characteristics of these cells and their surrounding environment. Neurons have long axons, which results in the vector having to move across long distances before reach the cellular body and exerting its therapeutical effect.[86,92,101] Neurons are also non-phagocytic in nature and exists in much lower numbers than glial cells which makes it even more complicated for the nanoparticles to

reach their target. Additionally, it is also difficult to target specific neuron populations.[102] Two of the most explored ligands for neuronal delivery are neurotrophins and portions of toxins (ex. Tetanus and botulinum). Neurotrophins are used due to their specificity to certain neuronal populations while portions of toxins are used due to their ability of crossing the BBB and targeting neurons.[86,92]

When the nanocarriers reach the neighboring region of target cells, they must face additional challenges. First, their internalization by the cells, which implies crossing a highly selective cellular membrane. Several properties affect nanoparticle uptake such as their size, surface charge, hydrophobicity, presence of ligands, among others. The presence of positive charge in the particle's surface favors the electrostatic interaction with the negatively charged cellular membranes, thus contributing for internalization when compared to non-polar or negatively charged particles.[86,93,103]

The cellular uptake of nanocarriers occurs through endocytosis, which can be divided into phagocytosis and pinocytosis which depends on particle size. For particles with a diameter bigger than 500 nm phagocytosis is used, while smaller particles are internalized through pinocytosis. This mechanism is subdivided even further into pathways that are clathrin dependent or non-clathrin dependent. It is reported that particles smaller than 100nm haver a more efficient endocytic internalization.[93,103-104] Particles can only be named as nanoparticles when their diameter is between 1-100 nm.[105]

Many of the internalization pathways lead to vector entrapment in endosomes which will mature and fuse with lysosomes, the enzymes present and the acidic pH then leads to the destruction of the vector.[106] Therefore, it is imperative that the nanoparticles escape the endosome to fulfil their therapeutic goal. It is reported that liposomes can promote the escape through destabilization of the endosomal membrane, while polymers with a high buffer capacity, like polyethyleneimine (PEI), promote the translocation of protons and chloride ions to the endosomal interior which results in an influx of water that swells the endosome, ending in its destruction. This effect is referred to as the proton sponge effect.[106-108] Finally, it is important that the nucleic acid is capable of dissociating from the delivery vector when the therapeutical target is reached. To assure this, is important that the interaction between the nucleic acid and the delivery vector is not strong enough to prevent an effective release.[109]

1.8 Chitosan delivery vector

Chitosan is an example of a natural polymer that has a prominent role in drug delivery systems thanks to its desirable characteristics such as biodegradability,

physiological inertness, biocompatibility and low cytotoxicity and low cost. Moreover, it is easy to chemically alter. This polymer is composed by D-glucosamine and N-acetylglucosamine linked by β1-4 glycosidic bonds. Although, chitosan in present in nature, most of this polymer is man-made, being produced from by the deacetylation of chitin, which is one of the most abundant polysaccharides available in biological systems being present in the exoskeleton of crustaceans and in the cellular wall of fungi and algae. The source and processing of chitosan has a significant impact in its properties, such as the degree of deacetylation, molecular weight and charge distribution which in turn affect the polymer's performance in varied range of applications.[110-112] The presence of three reactive groups, that are the primary amines, resultant from the removal of the acetyl-N-glucosamine moiety, and the two OH groups, facilitates chemical induced structural modifications in the chitosan molecule through nucleophilic substitutions or ligand conjugation which enhance the polymer's properties.[112-114]

When the pH is lower than 6.5, the primary amine groups are protonated and consequently the chitosan molecule becomes positively charged and therefore it becomes polar, which allows it to be solubilized in an aqueous medium. The charge density and solubility of chitosan are also dependent in the degree of deacetylation and chain length.[110-111,114] The positive charge allows chitosan to form complexes with negatively charged nucleic acids which in turn protects them from enzymatic degradation.[112]

When it comes to the design of chitosan-based nanoparticles, it is important to take certain factors into account, not only an array of molecular properties, like molecular weight and degree of deacetylation, but also the molar stoichiometry between the positive ammonium groups (N) of chitosan and the negative phosphate groups (P) of nucleic acids, which is referred to as the N/P ratio.

It is reported that higher molecular weight chitosan polymers are associated with the formation of chitosan/nucleic-acid complexes with enhanced stability and protection from the endosomal and extracellular environment. However, these heavier polymers are also associated with larger nanoparticles.

The degree of deacetylation defines the percentage of available amines, and therefore, the number of positive charges that could be present in the chitosan polymer for the interaction with the nucleic acids. Higher the degrees of deacetylation contribute to improved electrostatic interaction between chitosan and the nucleic acid, forming complexes with a slower degradation rate. To complex with siRNA, the degree of deacetylation should be superior to 80%. The nanoparticle's stability also depends on the molecular weight, since a larger amount of polymer provides a larger protection from degradation. The N/P ratio can help balance the stability of smaller polyplexes, with a

higher N/P values being required than for larger molecular weight polyplexes at a given degree of deacetylation. However, it is important to denote that a balance must be found between all these factors since nanoparticles that are too stable are not capable of dissociating from nucleic acids which lowers their transfection efficiency.[111,114]

Despite all the desirable characteristics of chitosan, its biomedical application are limited due to its partial protonation at physiological pH, which lowers its solubility. To solve this, it is standard practice to chemically modify chitosan. The most effective modification consists in the trimethylation of the molecule's primary amine groups leading to the formation of N,N,N-trimethyl chitosan (TMC). Comparatively to chitosan, TMC has a wider range of pH values in which it is soluble, a better interaction with nucleic acids and higher transfection efficiency.[111,115-117] This modification is done in the chitosan's lateral groups thus preserving all the biologically favorable properties of the molecule such as biodegradability, biocompatibility and being non-imunogenic.[115,118]

Both chitosan and TMC present mucoadhesive properties, mostly due to their cationic nature which allows electrostatic interaction with negatively charged mucin glycoproteins that are a component of the mucous membranes. Besides ionic interactions, non-covalent hydrogen bonding with mucin has also a relevant role in mucoadhesion. Thus, the nanoparticles formed by chitosan and its derivatives can be administered intranasally, resulting a direct delivery into the brain, bypassing the BBB.[119-120]

Another popular modification of chitosan and its derivatives consists in the copolymerization with poly(ethylene) glycol.[111,116] PEG is an electrically neutral, highly flexible and biocompatible amphiphilic polymer. PEG creates a protective hydration layer around the polyplexes by establishing hydrogen bonds, which results in shielding of the nanoparticle's positive charge, prevents the adsorption to biological components and nanoparticle aggregation through electrostatic repulsion. PEG's molecular weight reflects its chain length and should be superior to 2kDa since small chains do not possess the necessary flexibility to exert its beneficial effects.[121-122]

PEG's molecular extremities can be conjugated with targeting molecules, which provide targeting specificity.[121,123] Another structural parameter that has impact in the performance of PEG is its density in the nanoparticle's surface. PEG chains, when at low density, tend to be located closer to the surface of nanoparticles with a "mushroom" configuration. At high density however, PEG chains tend to be extended away from the nanoparticle's surface displaying a "brush" configuration. This brush configuration may benefit the targeting molecule's ability to recognize its corresponding receptor.[122]

All these characteristics help TMC to arise as one of the best candidates for a nanocarrier system that maximizes the advantages of intranasal delivery of miRNA to the rain and couples BDNF mimetics as ligands at specific neurotrophin receptors. For these and the above reasons, we chose TMC for the present work functionalized with PEG and with LM22A1, complexed with an anti-microRNA145 for neuroprotection in stroke pathology.

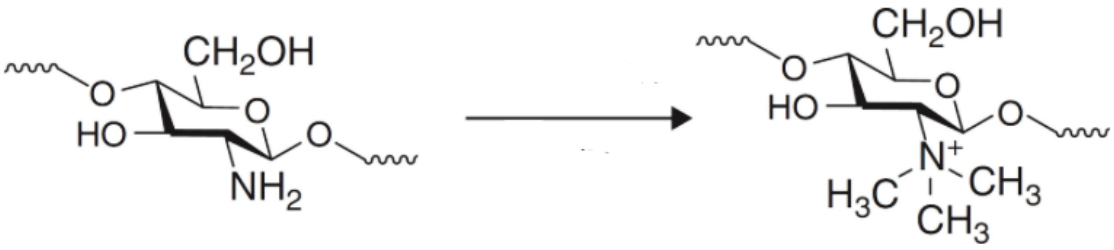

Figure 1. 6- Quaternization reaction of chitosan amino groups, giving rise to N, N, N-trimethyl chitosan. Adapted[117]

1.9 Aims

The main aims of the project were:

a) Explore the potential of TMC as a vector of nucleic acids to neurons, specifically an antagomir 145 or anti-microRNA145.
b) Evaluate the impact of a BDNF mimetic, namely the LM22A1 peptide as a specific TrkB receptor ligand and activator.

To attain these aims, different goals were established:

i) Functionalization of TMC
ii) Preparation of the different microRNA/TMC polyplexes
iii) Physicochemical characterization of the polyplexes
iv) *In vitro* assessment of the BDNF mimetic as an activator of TrkB receptor
v) Study of oxidative stress conditions that result in decreased SOD2 levels
vi) Evaluation of the TMC nanoparticles neuronal internalization

2. Materials and Methods

2.1 Synthesis of TMC-PEG-LM22A1 Copolymer

2.1.1 TMC functionalization with PEG linker

For the synthesis reaction, TMC polymer, derived from chitosan extracted from *Agaricus bisporus* mushrooms, was used. Previously, its molecular weight was determined to be 43.3 ± 5.0 kDa, and acetylation and quaternization degrees were 15.7 ± 0.9 % and 30.1 ± 4.6 %, respectively.[124-125]

The TMC polymer (25 mg) was solubilized in 5 mM HCl, overnight (O/N) under magnetic stirring, at a final concentration of 6 mg/ml. Afterwards, an equivalent volume of phosphate buffer (20 mM in Mili-Q water, pH = 6.5) was added, achieving a final concentration of 3 mg/ml. This solution was maintained under stirring for 2 hours at room temperature (RT). Concurrently, the Maleimide-poly(ethylene)glycol-N Hydroxysuccimide (MAL-PEG-NHS; Jenken, 5kDa) linker was weighed (25 mg) and subsequently solubilized in 1 ml of dimethyl sulfoxide (DMSO) in a glove box under argon atmosphere. Then, this solution was added drop by drop to TMC, followed by an overnight reaction at RT, under magnetic stirring and in light protective conditions.

The resultant solution was diluted in Mili-Q water (to reduce the percentage of DMSO) and dialyzed against 4 L deionized water (dH_2O) recurring to a membrane with a 10 kDa molecular weight cut-off (Spectra Por^{TM}) to exclude the free PEG from the final product. This method was performed during 48 hours at 4ºC under magnetic stirring, with the dH_2O being regularity replaced. The sample was frozen at -80ºC and subsequently freeze-dried at the same temperature for 48 hours. The TMC-PEG was kept at -20ºC under argon storage conditions.

Finally, the reaction yield was determined by mass and the PEGylation degree of the final product was accessed by Proton Nuclear Magnetic Resonance ^{1}H-NMR (400 MHz, Bruker). For this analysis, 2 mg of the TMC-PEG polymer were dissolved in D_2O for 24h under stirring at RT, in a final concentration of 3.3 mg/ml. The degree of functionalization was obtained through the ratio between the peak of the maleimide protons and the acetyl protons of the N-acetylglucosamine (performed by Victoria Leiro, nBTT, i3S).

2.1.2 TMC-PEG Bioconjugation with LM22A1 BDNF mimetic

The TMC-PEG-MAL (TMC-PEG) (10 mg) synthetized product, was dissolved in milli-Q H_2O at a final concentration of 3 mg/ml and maintained under stirring for 3 hours at RT. Then, a two-fold dilution was performed with the addition of 20 mM phosphate buffer at pH=7.

In turn, 3 mg of the mimetic LM22A1 modified with a cysteine (LM22A1-Cys; 5-Oxo-L-prolyl-L-histidil-L-trytophan-n-Cys; 96.02% purity; MW of 555.61 g/mol; LifeTein) was weighed and dissolved in N, N-Dimethylformamide (DMF) at a final concentration of 3.3 mg/ml. This solution was added to TMC-PEG, and kept reacting for 6 hours at RT, under stirring and protected from the light. Later, dialysis and lyophilization steps were performed for 48 hours, as previously described. The product was stored at -20ºC and under argon conditions. Reaction yield was calculated as aforementioned. The final product was dissolved in DMSO D6 (Eurisotop®) for 24 hours stirring at RT and the degree of functionalization with the LM22A1 was obtained by ^{1}H-NMR (600 MHz,Bruker).

2.1.3 TMC Quantification by Cibacron Method

Prior to the production of nanoparticles, the TMC, TMC-PEG and TMC-PEG-LM22A1 polymers were weighed and solubilized overnight in 5 mM HCl at a final concentration of 2 mg/ml, under magnetic stirring at RT. Subsequently, the same volume of 20 mM HEPES buffer with 5% (w/v) glucose, pH = 7.4 (HEPES-Glucose buffer), was added to obtain a concentration of 1 mg/ml. This solution was kept under stirring for 1 hour.

The polymers were filtered with a cellulose acetate membrane syringe filter (0.45 µM pore size; Q-Max®) and quantified using a colorimetric method based on its interaction with the dye Cibacron Brilliant Red (Sigma-Aldrich). This dye presents in its chemical structure sulfonic groups with negative charge that interact electrostatically with the protonated groups of the TMC, which results in a spectral red shift to 595 nm. For the calibration curve, several standard solutions with known concentrations of the unfiltered polymer were previously prepared (1, 0.8,0.6,0.4, 0.2 and 0 mg/ml in HEPES-Glucose buffer). The Cibacron dye was solubilized in milli-Q H_2O at a concentration of 1.5 mg/ml, followed by a 20-fold dilution in HEPES-Glucose buffer, in order to reach a concentration of 75 µg/ml. This final solution was added to the filtered and unfiltered samples of the polymers (500 µL), being subsequently vortexed and left under stirring at 800 rpm during an incubation period of 20 minutes at RT. Finally, 200 µL of each solution was added to a 96-well transparent plate (in duplicates), followed by absorbance measurement at 575 nm in a Synergy™ Mx microplate reader (BioTek).

The polymer concentration of the filtered samples was calculated using the linear regression equation of the calibration curve, in which the absorbance was plotted versus the concentrations of the respective unfiltered solutions.

2.1.4 Functionalization evaluation by Ultraviolet/Visible (UV/Vis) Spectroscopy

To further complement the NMR results, the reaction of TMC-PEG with LM22A1 was analyzed through UV/Vis Spectroscopy. To interpret and draw conclusions about the UV/Vis spectrum of TMC-PEG-LM22A1, the free LM22A1-Cys and LM22A1 peptides and the TMC and TMC-PEG polymers were also analyzed by this technique.

The original mimetic LM22A1 (2 mg/ml, 96.71% purity, LifeTein) and LM22A1-Cys (5 mg/ml, 95.77% purity, LifeTein) stock solutions were diluted to a final concentration of 0.01 mg/ml in 20 mM HEPES buffer, 5% glucose, pH = 7.4. Then a TMC-PEG-LM22A1 polymer solution was prepared with the same molar quantity as the LM22A1-Cys solution, by diluting a stock solution (0.90 mg/ml) previously filtered and quantified by the Cibacron method, in the same buffer. Finally, TMC and TMC-PEG solutions with a mass concentration equal to the free mimetics were also prepared, also diluted from formerly quantified concentrated solutions.

The absorbance spectra (190 to 800 nm range) of each compound was obtained by measuring with a UV/Vis Spectrophotometer (Perkin Elmer), in Hellma cuvettes (quartz Suprasil®, 10 nm, pathlength, 50µL chamber volume).

2.2 Production and physical characterization of TMC, TMC-PEG and TMC-PEG-LM22A1 Polyplexes

2.2.1 Production of TMC, TMC-PEG and TMC-PEG-LM22A1 Polyplexes

To form the nanoparticles, the TMC, TMC-PEG and TMC-PEG-LM22A1 polymers were solubilized, filtered and quantified by the Cibacron method as described above. The polymers were complexed with different oligonucleotides according to the purpose of the study. For the nanoparticle's physical characterization, the miRIDIAN microRNA Hairpin Inhibitor Negative Control (MW 18379 g/mol; Dharmacon™) was used, which corresponds to a non-functional oligonucleotide with a molecular weight equal to the functional antagomir 145 (18379 g/mol) as well as similar nucleotide size and structure. The non-functional and epifluorescent miRIDIAN microRNA Hairpin Inhibitor Transfection Control with Dy547 (MW 18871 g/mol; Dharmacon™) was selected for the polyplexes internalization assays. The stock solutions of these miRNAs had a concentration of 25μM and were prepared by resuspending the powder sample in nuclease free water (QIAGEN) and stirring at RT for 30 minutes.

In all assays involving the polyplexes, the molar ratios were established between quaternized amine groups of the polymer (positive charge) and the phosphate groups (negative charge) of the microRNAs (N/P molar ratios) of 3, 5 and 10. For the production of polyplexes, a fixed amount of 0.5 μg miRNA (equal number of moles of phosphate per N/P ratio) was used, with the concomitant adjustment of the amount of polymer added according to its calculated concentration, to achieve the desired ratio. The polymers were diluted in HEPES/Glucose buffer prepared in DEPC treated MiliQ-H_2O. Next, the polymer and miRNA solutions were pre-heated to 40ºC for 5 minutes without stirring (Thermomixer) and then equal volumes of each were mixed. In this step, the micro-RNA solution was added drop by drop to the polymer solutions, while vortexing. Complexation occurred by heating this mixture at 40ºC for 10 minutes under agitation (1000 rpm, Thermomixer). Finally, the complexes were stabilized for 30 minutes at room temperature, without agitation and subsequently subjected to a quick spin for 10 seconds at 1000 revolutions per minute (rpm).

2.2.2 Characterization of TMC, TMC-PEG and TMC-PEG-LM22A1 polyplexes by Dynamic Light Scattering (DLS)

The size, polydispersity index (PDI) and zeta potential of the polyplexes were accessed through the DLS technique, performed by the Zetasizer Nano ZS equipment (Malvern).

The size measurements were carried in a disposable solvent resistant micro-cuvettes (ZEN0040), at a temperature of 25ºC and scattering angle of 173º (backscatter). The samples were equilibrated for 60 seconds and for each analysis 3 measurements were made, with an automatic number of runs. The hydrodynamic mean diameter (Z-average) and PDI were determined by the cumulant analysis.

For the evaluation of the zeta potential, the high concentration quartz Zeta potential cell (ZEN1010) was used. The analysis was carried out at 25ºC, with an initial equilibration time of 30 seconds. Three measurements with 100 runs were performed per analysis, with a 60 seconds delay between them.

The DLS data was processed using the Zetasizer software (Malvern).

2.3 Cell Culture

2.3.1 HT22-GFP Cell line

The HT22-GFP strain was derived from the HT22 immortalized mouse hippocampal neuronal cell line, after transfection with a TrkB mEGFP plasmid, (Master project of Diana Bola, nBTT i3S). These cells are phenotypically similar to the precursor cells but present TrkB receptor expression, which is associated with fluorescence. The TrkB-EGFP cells were selected by a series of sorting cycles by the Fluorescence-activated Cell Sorting (FACS) technique and the population with a dim (low expression) were chosen.

The HT22-GFP cells were cultured in Dulbecco's Modified Eagle's Medium (DMEM) supplemented with 10% Fetal Bovine Serum (FBS) and 1% Penicillin/Streptomycin antibiotic (P/S) (DMEM complete medium) at 37ºC and 5% CO_2, being passaged every 3-4 days when reached a 70-80% confluency.

Throughout the various *in vitro* studies conducted, these cells were extensively used, having been plated with different densities, in several types of cell plates pre-treated or not with Poly-D-lysine (PDL). The conditions used for HT22-GFP cells are properly explained in each assay description.

For the plate surface coating, Poly-D-lysine with a final concentration of 10 µg/ml in sterilized Mili-Q H_2O was added with an appropriate volume that covered the whole surface for 1 hour at RT, followed by two washing steps with sterilized Mili-Q H_2O and leaving to dry in the laminar flow hood followed by storage at 4ºC until used.

2.3.2 Primary Cortical Cell Culture

The primary mouse neuronal cortical cell cultures (NCCC) were kindly supplied by Marília Torrado (nBTT group, i3S). The NCCC cells were derived from the cortices of E16.5 C57BL/ 6 mice embryos. These were processed through trypsin digestion (1.5 mg/ml), followed by two washing steps with Hank's Balanced Salt Solution (HBSS) containing 10% FBS and HBSS, respectively. The tissue was dissociated in Neurobasal medium (NBM; Gibco, Life Technologies) with a pipette and the cells were filtered. The cells were then cultured in PDL coated sterilized coverslips in 24 multi-well plates at a density of $15x10^4$ cells/well, in NBM supplemented with 2% SM1 (StemCell Technologies), 0.5 mM L- glutamine, 0.025 mM glutamate and 50 µg/ml gentamycin (Gibco, Life Technologies) (NBM complete medium), with a final volume per well of 1 mL. Besides, for pre-coated PDL 12 well chamber slide Ibidi®, $5x10^4$ cells/well were plated in a volume of 300 µL of the same medium. The cells were cultured for 7 days *in vitro* (7 DIV) at 37 ° C with 5% CO2, with no medium exchange. For the 14 DIV experiments, half of the medium was removed on the seventh day and replaced with supplemented NBM without glutamate.

2.4 Evaluation of TrkB Phosphorylation

2.4.1 Immunocytochemistry

The immunocytochemistry assays were performed in HT22-GFP cell line and in NCCC primary neuronal culture.

HT22-GFP cells were plated onto PDL coated 12 well Ibidi® chamber slide at a density of $2x10^4$ cells per well in a final volume of 200 µL of DMEM complete. After 24 hours, the cells were subjected to starvation for 1 hour, by changing the medium to DMEM without supplements. Then, the stimulus was proceeded with BDNF (100 ng/ml) and the mimetics LM22A1, LM22A1-Cys and LM22A4 (500 ng/ml) diluted in DMEM without supplements, during 1 hour.

The NCCC cells were plated on PDL coated 12 well Ibidi® chamber at a density of $5x10^4$ cells per well in a final volume of 300 µL in Neurobasal complete medium. After

one week in culture, the cells were starved for 1 hour with fresh NBM medium and the culture media was used as conditioned media to dilute the stimuli. The incubation was similar to HT22-GFP cells.

For both cell types, the stimuli was removed and a washing step was performed with PBS, followed by fixation with 4% paraformaldehyde (PFA) for 10 minutes at RT. After washing twice with PBS for 10 minutes, the cells were permeabilized with Triton X-100 0.1% in PBS for 5 minutes at RT. Following two washes with PBS and incubation with a blocking solution composed of 4% FBS, 1% bovine serum albumin (BSA) and 0.1% Triton X-100 0.1% in PBS, for 1 hour at RT.

For HT22-GFP cells, the polyclonal rabbit anti-phospho-TrkB (Ty816), (α-pTrkB, EMD Milipore), diluted 1:300 in blocking solution was used as the primary antibody. Additionally, NCCC cells were stained with a mouse anti-tubulin β3 antibody (TUBB3, BioLegend), diluted 1:500 in blocking solution. The incubation with the primary antibodies was performed O/N at 4ºC in a humidified chamber.

The following day, another washing step was done with PBS as described above, followed by incubation with the secondary antibodies for 1 hour, in the dark at RT. The secondary antibodies Alexa Fluor 568 donkey anti-rabbit IgG (Invitrogen) and the Alexa Fluor 647 donkey anti-mouse IgG (Invitrogen), diluted 1:1000 in blocking solution, were incubated in NCCC cells. Whereas, the HT22 cells were only incubated with Alexa Fluor 568 donkey anti-rabbit IgG (Invitrogen), with the same dilution factor. The cell nuclei were stained with 4',6'-diamino-2-phenylindole (DAPI) at a concentration of 0.1 µg/ml in PBS for 10 minutes. The microscopy slides were mounted in Fluoromount™ Aqueous Mounting Medium (Sigma-Aldrich) and stored at 4ºC until further analysis. The immunostained HT22-GFP cells were visualized in the inverted fluorescence microscope Axiovert 200M, while the NCCC cells were analyze by the confocal SP5 microscope (Leica). The images were processed recurring to Fiji Software.

2.4.2 Sandwich Enzyme-linked Immunosorbent (ELISA) Assay

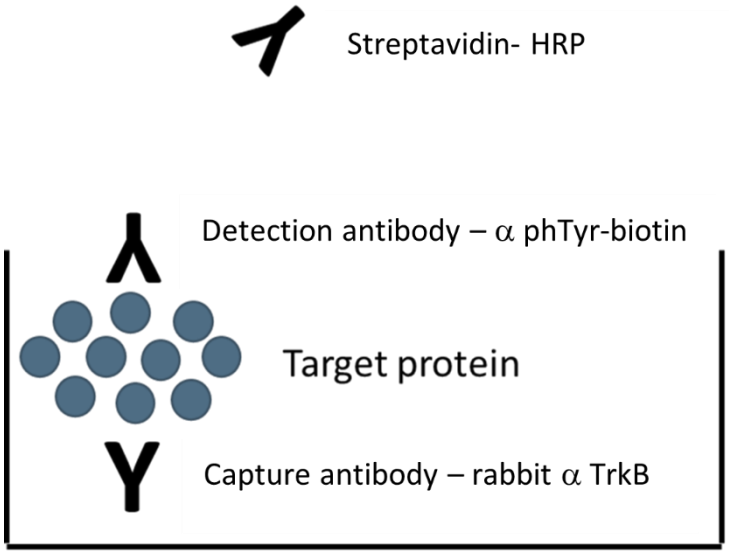

Figure 2. 1- Schematic representation of the assembly of the ELISA assay set up.

The cell culture conditions and stimulation procedure for HT22-GFP and NCCC cells was similar to that performed for immunocytochemistry assays, except the density and cell culture plates and volumes of media used. HT22-GFP cells were plated in 24 well plates at a density of $20x10^4$ cells per well in DMEM complete (final volume of 500 ml) for 24 hours. In turn, NCCC cells were plated in pre-coated 24 multi-well plates at a density of $15x10^4$ cells per well.

After stimulation with BDNF (100 ng/ml) and the mimetics LM22A1, LM22A1-Cys and LM22A4 (500 ng/ml) for 1 hour, the cell medium was removed and a washing step was performed with PBS. Then, both cell types were incubated with 110 µL of lysis buffer on ice, for 5 minutes. The lysis buffer was composed of 100 mM Tris at pH=7.4, 150 mM NaCl, 0.5% Triton X-100 and freshly added proteases (1:100; Bimake) and phosphatase inhibitor cocktail (1: 100; Bimake) in PBS. Cell lysates were collected and sonicated for 5 minutes and placed on ice again. Subsequently, the lysates were centrifuged at 14000 rpm for 10 minutes at 4°C and the supernatant protein extract was collected for assaying.

An ELISA 96 well plate (MaxiSorp™) was incubated overnight at 4ºC with the capture antibody rabbit anti-TrkB antibody (rbt αTrkB; Merck) diluted 1:1000 in coating buffer (0.014 mM Na_2CO_3, 0.035 mM $NaHCO_3$; pH 9.6). Afterwards, the plate was washed three times with PBS containing 0.05%(v/v) Tween®-20 (PBS-T) and twice with PBS. Plate surface blocking was performed through the incubation with 0.5% BSA in PBS for 1 hour at RT. Then, the plate was washed again, and the protein samples were

added to the ELISA wells (100 µL per well), for 90 minutes at RT. As a control in some wells, lysis buffer was added instead of the protein sample. Following a washing step, the detection antibody diluted 1:2000 in PBS-T containing 0.5% of BSA (anti-Phosphotyrosine, clone 4G10®, Biotin Conjugate, phTyr; Merck) was incubated overnight at 4º.

The next day, Horse-radish Peroxidase Streptavidin ELISA grade (Vector Laboratories) diluted 1:200 in PBS-T containing 0.5% of BSA, was incubated for 1 hour at RT. After the last wash, the plate was incubated with 3.3',5.5'-tetramethylbenzidine (TMB, BioLegend) for 20 minutes under gentle shaking, followed by the addition of 0.2M H_2SO_4 (as stop solution). Absorbance at 450 nm was measured using Synergy ™ Mx Microplate Reader.

To analyze the fold-changes in phosphorylation of the TrkB receptor in samples treated with BDNF and mimetics, their respective absorbance values were divided by those obtained for untreated cells in the GraphPad Prism program.

2.4.3 Western Blot

The phosphorylated TrkB receptor and extracellular signal-regulated kinases 1 and 2 (ERK 1/2) were quantified in protein extracts of HT22-GFP and NCCC by western blot. HT22-GFP cells were seeded in a 24 multi-well plates at a density of $14x10^4$ cells per well and cultured for 24 hours. NCCC cells were prepared as previously reported and maintained *in vitro* for 7 or 14 days. For both cell types, stimuli with BDNF and the mimetics LM22A4, LM22A1 and LM22A1-Cys was proceeded as described above.

After 1 hour of incubation with the stimuli, the medium was removed and the cells were washed with PBS at RT. Afterwards, cell lysis was performed by adding 30 µL of cold radioimmunoprecipitation assay (RIPA) lysis buffer, composed by 50 mM Tris HCl, pH = 8.0, 150 mM NaCl, 1% IGEPAL® (NP-40, Sigma-Aldrich), 0.5% Sodium Deoxycholate, 0.1% SDS and freshly added proteases (1:100; Bimake) and phosphatases inhibitors cocktail (1:100; Bimake) in dH_2O. The plate was immediately placed on ice and the cells were detached using cell scrapers. After, these samples were sonicated for 5 minutes and centrifuged at 14000 rpm at 4ºC for 15 minutes. The protein concentration of the supernatant was calculated and the remaining supernatant conserved at -80ºC until further use. For that, a Bicinchoninic acid (BCA) assay was performed, using bovine serum albumin (BSA) as protein standard. This procedure is based on the reduction of Cu^{2+} in Cu^{+} by proteins in an alkaline solution, followed by the chelation of Cu^{+} with two BCA molecules, forming a complex with an absorbance at 562 nm. For this purpose, several standard solutions with known BSA concentration were

prepared through serial dilution (2000, 1500, 1000 ,750, 500, 250, 125, 25, 0 µg/mL in RIPA buffer). Then 25 µL of the standard or unknown samples were added to a 96 well microplate in duplicate, to which 200 µL of BCA working reagent (Pierce™ BCA Protein Assay kit, Thermo Scientific) was added. The plate was sealed and incubated at 37 ºC for 30 minutes. After cooling to RT, the absorbance was measured at 562 nm in the Synergy ™ Mx Microplate Reader. The concentration of the samples was obtained through linear regression equation of the standard curve.

The frozen samples were allowed to unfreeze in ice and processed for western blot. 20 µg of total protein were loaded per well in a final volume of 25 µL after denaturing in the presence of the reducing reagent β-mercaptoethanol (Sigma-Aldrich) in 1x Bolt ® LDS sample buffer (Alfagene). The samples were heated to 70ºC for 10 minutes, spin down and then placed on ice.

The final volume of the samples (50 µL) was loaded into the gel (Bolt™ 4-12% Bis-Tris Plus Gel, 10-well), placed in a Mini Gel Electrophoresis Tank (Invitrogen™) filled with MOPS running buffer (1x; Thermo Fisher Scientific) previously cooled at 4ºC. 5 µL of a ladder was loaded (Precision Plus Protein Dual-color Standards, BioRad).

The gel electrophoresis was performed at 80 mV during 20 minutes, followed by an voltage increase to 110 mV for 75 minutes. The proteins were electrotransferred with the iBlot ™ 2 Dry Blotting System (Invitrogen™) to a nitrocellulose membrane (iBlot ™ Transfer Stack; Thermo Fisher Scientific) for 9 minutes (20 V for 1 minute, 25 V for 8 minutes). After an washing step with 1x Tris-buffered saline (TBS), the membranes were incubated with Ponceau for 5 minutes at RT under slowly shaking, in order to stain the total protein transferred. The excess of dye was removed with TBS and was acquired a colorimetric image with Chemidoc XRS+ Imaging system.

Afterwards, the membranes were washed twice in TBS with 0.1% Tween 20 (TBS-T) in order to remove the ponceau staining. The membranes were cut horizontally according to the molecular weight of the proteins of interest, followed by the blocking with filtered 5% BSA(NZYTech) in TBS-T solution, for 1 hour at RT, with gentle agitation. The sections were incubated with the respective primary antibody overnight at 4 °C. For the detection of the phosphorylated TrkB receptor, the antibody Phospho-TrkB (Tyr816) Rabbit mAb (Cell Signalling Tecnology), diluted 1:1000 in 1% BSA in TBS-T, was used. Whereas, the Phospho-p44/42 MAPK (ERK1/2) antibody diluted 1:2000 (HT22-GFP cells) or 1:4000 (NCCC cells) in 1% BSA in TBS-T was also used to identify the phosphorylated enzymes ERK1/2. After washing three times with TBS-T (5+10+5 minutes), the blots were incubated with the secondary antibody Donkey Anti-Rabbit IgG (H+L) (Jackson ImmunoResearch) diluted 1: 5000 in 0.5% BSA in TBS-T, for 1 hour at

RT under gentle agitation. The membrane was rinsed again in TBS-T with gentle agitation.

The blots were incubated with WesternBright Quantum (Advansta) components 1:1 for 2 minutes and the chemiluminescent signal was detected on the ChemiDoc XRS + Imaging System (BioRad). For the densiometric analysis and semi-quantification of the blots, Image Lab software 6.0.1 (BioRad) was used, where adjustments were made in order to guarantee the same width in each lane and in the bands of interest, as well as an appropriate subtraction of the background disk equal for each lane. The analysis of the intensity of each band, measured by the sum of the total volume under each curve (three-dimensional peak), was performed in relation to the reference band (untreated cells). To guarantee an equal loading between the different samples, the relative quantification of a certain band in the various conditions was made in relation to the control on the membrane with the total protein stained with ponceau, and these values were subtracted to the fold changes obtained on the same membrane analyzed by chemiluminescence.

2.5. Glutamate-induced Oxidative Stress

2.5.1 Quantification of SOD2 Expression

The one-step Reverse Transcriptase Quantitative Polymerase Chain Reaction technique (one-step RT-qPCR) was executed in order to quantify the levels of mRNA of the SOD2 enzyme in HT22-GFP cells, when subjected to conditions of oxidative stress induced by glutamate. Initially, the selection of the best primers was done, through the analysis of real time-PCR amplification efficiency. The sequence and melting temperature of the primers are presented in the **Table 2.1**. The primers YWHAZ and HPRT (mouse) were tested as housekeeping genes, while for the quantification of SOD2, three primers were designed using the Primer-BLAST tool, using the mitochondrial mRNA of the *Mus musculus* SOD2 as input template sequence. The off-target complementarity of these primers was also evaluated using the Blast-n tool.

Table 2. 1- Sense (S) and antisense (AS) primers sequences and respective Melting Temperatures (T_m).

Primer	Sequence (5' to 3')	T_m (°C)
SOD2- A	S: ACA CAT TAA CGC GCA GAT CA AS: AGT TGT AAC ATC TCC CTT GGC	54.9 54.9
SOD2- B	S:GCT GGC TTG GCT TCA ATA AG AS: GCG GAA TAA GGC CTG TTG T	54.4 52.6
SOD2- C	S: GTT ACA ACT CAG GTC GCT CT AS: CAA CTC TCC TTT GGG TTC TCC	50.0 52.4
HPRT	S: GTA ATG ATC AGT CAA CGG CGG AC AS: CCA GCA AGC TTG CAA CCT TAA CCA	57.4 60.3
YWHAZ	S: GAT GAA GCC ATT GCT GAA CTT G AS: GTC TCC TTG GGT ATC CGA TGT C	54.8 56.8

For the evaluation of the amplification efficiency, cDNA prepared from a mixture containing total RNA was obtained from HT22-GFP cells. For that, cells were plated in a 96-well plate at a density of 7500 cells per well in DMEM complete medium and maintained in culture for 24 hours without any stimulus. Two washing steps with PBS were performed, followed by incubation with 30 µL of filtered Cell Lysis buffer (10 mM Tris-HCl, pH = 7.4; 0.25% IGEPAL CA-630, 150 mM NaCl) for 10 minutes on ice. The lysates were pipetted up and down twice, followed by their collection to 0.6 mL maximum recovery microtubes (Axygen) and centrifugation at 700G, for 5 minutes at 4ºC. Later, the supernatant was subjected to a 10-fold serial dilution in cell lysis buffer (1:10; 1:100; 1:1000).

In a 384 PCR plate, it was added per well: 5 µL of One Step SYBR RT-PCR Buffer 4, 0.4 µL of PrimeScript 1 step Enzyme Mix 2 (One Step SBYR® PrimeScript™ RT PCR Kit II, Takara), 3 µL of RNase Free dH2O and 0.3 µL of each reverse and forward primer (final concentration of each 300 µM). After adding this mixture, 1 µL of the original sample and the various dilutions were added to the respective wells. Each condition was analyzed in triplicate. The plate was analyzed in the Real time PCR CFX384 (BioRad) equipment and the thermal cycling conditions were established as represented in **Table 2.2**. To calculate the reaction amplification efficiency for each primer under study, a calibration curve was created with the obtained cycle threshold values (Cq) versus the logarithm of the starting quantities of RNA, in the Bio-Rad CFX Maestro Software. The most suitable primers were selected based on the linear regression slope of the standard curve.

Thereafter, HT22-GFP cells were plated under the same conditions as previously described in this section, and subsequently incubated for 24 hours with glutamate (0.25,1,2,4,8 mM) and menadione (4 and 8 µM), which was used as a possible positive control. The lysis protocol of the were the same as mentioned above. The fold change values of the SOD2 mRNA levels were analyzed using the $2^{-\Delta\Delta Cq}$ method. Initially, the SOD2 Cq means were subtracted by the values of the housekeeping genes (ΔCq). Then, the difference between the ΔCq of the treated samples and the ΔCq of the control sample (ΔΔCq) was calculated, followed by the determination of the value of $2^{-\Delta\Delta Cq}$ to obtain the fold change value in relation to the control.

Table 2. 2- Thermal cycling conditions of the RT-PCR reaction.

Cycle Step	Temperature (°C)	Time	Cycles
Reverse Transcription	42	5 min	1
Initial Denaturation	95	10 sec	1
Denaturation Annealing Extension	95 55 72	10 sec 30 sec 30 sec	40

2.5.2 Quantification of ROS production by Flow Cytometry

The intracellular ROS were measured by FACS in HT22-GFP cells treated with glutamate, using the 2 ', 7'-Dichloroflourescein diacetate ($DCFH_2$-DA) probe. This probe is commonly applied in *in vitro* oxidative stress assays, being converted into a highly fluorescent product (DCF) when oxidized by intracellular ROS.

For this purpose, HT22-GFP cells were plated with a density of $2.7x10^4$ cells per well in DMEM and maintained in culture for 24 hours at 37ºC. Then, were stimulated with glutamate or Fenton reagent (as positive control) for two different incubation periods, 2 and 24 hours. For the 24-hour incubation period, concentrations of 4, 2, 1, 0.5 and 0.25 mM of glutamate were tested, whereas for 2 hours of incubation only the concentrations of 4 and 2 mM were analyzed. The different concentrations of glutamate were prepared from a stock solution of 50 mM in sterilized Mili-Q H_2O, diluted in DMEM medium without

supplements. It is described that the Fenton reagent promote the production of reactive hydroxyl radicals, therefore was used as a positive control in this assay. In both conditions under study, this reagent was added in a concentration of 2 mM, being prepared by mixture $FeSO_4$ and H_2O_2 solutions.

After the incubation periods with the aforementioned stimuli, the medium was removed and the cells were washed with PBS, followed by the addition of the $DCFH_2$-DA probe for 90 minutes at 37ºC, prepared by diluting a 100 mM in DMSO stock solution of DCFH2-DA (MW 487.3 g/mol), to a final concentration of 0.1 mM in HBSS, in conditions protected from light. Then, the medium was again removed and the cells were washed with PBS, followed by their trypsinization for 5 minutes and inactivation by the addition of PBS with 10% (v/v) FBS. The cells were harvested onto eppendorfs and centrifuged for 3 minutes at 400G. The supernatant was removed, a washing step with PBS was performed and the pellet was resuspended in 100 µL of 4% PFA for 10 minutes. The samples were centrifuged at 1500 rpm for 5 minutes, followed by resuspension in 200 µL ice-cold PBS. The cells were kept in the dark at 4ºC until analysis by the Accuri Flow Cytometer. The data was processed using the Flow Jo software.

2.6 Nanoparticles Cellular Internalization Assays

In these assays the HT22-GFP cells were plated on PDL coated 12 well Ibidi® chamber with a density of $2x10^4$ cells per well (final volume 200 µL) and maintained in culture for 24 hours in DMEM complete medium.

Next, nanoparticles of TMC, TMC-PEG and TMC-PEG-LM22A1 complexed with miRIDIAN microRNA Hairpin Inhibitor Transfection Control with Dy547 were produced in sterile conditions, following the protocol mentioned above. The fluorescent labelling present in the microRNA permitted the monitoring of the nanoparticle's cellular internalization. The nanoparticles were added to the cells at a final concentration for miRNA at either 25 or 12.5 nM in DMEM without supplements.

Upon 6 hours of incubation with the nanoparticles and the positive control, the medium was removed and the same volume of DMEM complete was added in HT22-GFP cells. 24h after the addition of nanoparticles, a washing step was performed with PBS and the cells were fixed with 4% PFA (Merck) for 10 minutes. The cells were washed three times with PBS and the cell membranes permeabilized with 0.1% Triton-X 100 in PBS at RT for 10 minutes. An incubation step was performed with Alexa Fluor-647 phalloidin (Invitrogen) diluted 1:50 in PBS during 20 minutes in order to stain the F-actin,

followed by PBS washing. Then, cell nuclei staining was accomplished by the incubation with Hoechst 33342 (Thermofisher) diluted 1:2000 in PBS for 10 minutes. The cells were washed again with PBS. This entire procedure was carried out protected from light.

The Fluoromount ™ Aqueous Mounting Medium (Sigma-Aldrich) was used to mount the microscopic slides. These were stored at 4ºC until their visualization by fluorescence microscopy with a SP5 confocal microscope (Leica). The obtained images were analyzed using Fiji Software.

3 Results and Discussion

3.1 Synthesis of TMC-PEG-LM22A1 Copolymer

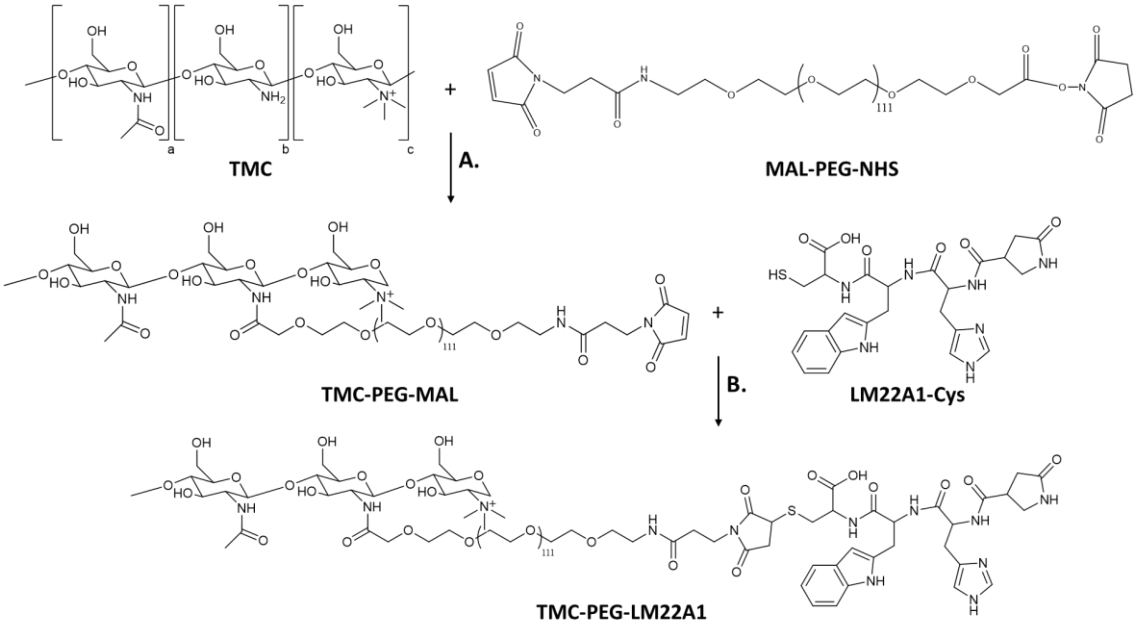

Figure 3. 1- Schematic representation of the two-step synthesis reaction of TMC-PEG-LM22A1. A. Functionalization of TMC with the heterobifunctional N-hydroxysuccinimide-PEG-maleimide linker. B. Bioconjugation reaction of TMC-PEG-MAL copolymer with the LM22A1-Cys peptide.

The synthesis reaction of the TMC-PEG-LM22A1 copolymer was performed in two steps, as schematized in **Figure 3.1**. Initially, the TMC polymer was functionalized via amide bonds with the 5 kDa heterobifunctional PEG linker (MAL-PEG-NHS), through the reaction between the NHS ester group and the primary amines of the TMC glucosamine residues. The resulting product from this reaction had a degree of PEGylation of 3.3%, that was accessed by Proton Nuclear Magnetic Resonance (^{1}H-NMR) (**Figure A.1**) through the calculation of the ratio between the peak of the maleimide protons and the acetyl protons of the N-acetylglucosamine. A reaction yield of 91.36% was obtained (determined by mass).

In a second step, the TMC-PEG-MAL product (TMC-PEG) was bioconjugated with the BDNF mimetic LM22A1, whose structure was modified with a cysteine - LM22A1-Cys. The maleimide of TMC-PEG reacts selectively with the thiol group present in the side chain of cysteine, forming thioester bonds. The final copolymer TMC-PEG-LM22A1 was obtained with a yield of 66.9%. The functionalization of the mimetic was also analyzed by ^{1}H-NMR, being accomplished a degree of functionalization of 8.6% (**Figure A.2**).

Additionally, the TMC-PEG-LM22A1 polymer was also analyzed by Ultraviolet/Visible (UV/VIS) Spectroscopy, along with the TMC-PEG, TMC and the free mimetics LM22A1 (original) and LM22A1-Cys (modified). A wavelength scanning (190 nm-800 nm) was performed for each compound in order to produce their respective spectra and identify absorption peaks (**Figure A.3 and Table A1**).

As shown in **Figure A.3**, the LM22A1 and TMC-PEG-LM22A1 exhibited similarities in their absorbance spectra, with a peak at the maximum absorption wavelength (**λ**max) in the region of 225-234 nm. This peak is expected to result from the contribution of the peptide bond, since close to 190–230 nm is the zone where the protein's peptide backbone absorbs. This was reinforced, as for TMC and TMC-PEG compounds (i.e. without the mimetic) no such peak exists. Moreover, the obtained spectra of TMC and TMC-PEG-MAL were similar, though quite different from TMC-PEG-LM22A1. This confirms once again that the mimetic was effectively bound to TMC-PEG. There was also a small increase in absorbance in the region of 280 nm for TMC-PEG-LM22A1 and LM22A1-Cys possibly due to the disulfide bond in the first case and to the presence of the tryptophan's aromatic ring in both cases. However, this need to be further explored.

3.2 Structural Characterization of TMC, TMC-PEG and TMC-PEG-LM22A1 Nanoparticles

After the chemical synthesis process, the next step consisted in the production and characterization of polyplexes formed with the different TMCs and the microRNAs. A rational structural physicochemical characterization of the polyplexes is fundamental since it consists of a preliminary process to predict their biological behavior, safety and effectiveness, as well as to interpret and establish correlations of *in vitro* biological data.[126]

In this sense, polyplexes were produced through the complexation of TMC, TMC-PEG and TMC-PEG-LM22A1 with non-functional micro-RNA (miRIDIAN microRNA Hairpin Inhibitor Negative Control) with N/P ratios of 3, 5 and 10, followed by characterization of its size, polydispersity and charge through Dynamic Light Scattering (DLS). This technique is based on the Brownian motion of the particles in suspension, which causes intensity fluctuations of the scattered light over time, when irradiated by a monochromatic beam of light. This motion is caused by the collision of the nanoparticles with the solvent molecules and is dependent on their size, medium viscosity and temperature. The detection of intensity fluctuations allow to extract the diffusion

coefficient of the nanoparticles, which in turn is a parameter used to calculate the hydrodynamic radius of the nanoparticles using the equation Stokes-Einstein. The smaller nanoparticles move at a higher speed and promote faster intensity fluctuations of scattered light compared to larger particles.[127-128]

3.2.1 Nanoparticle's size and polydispersity

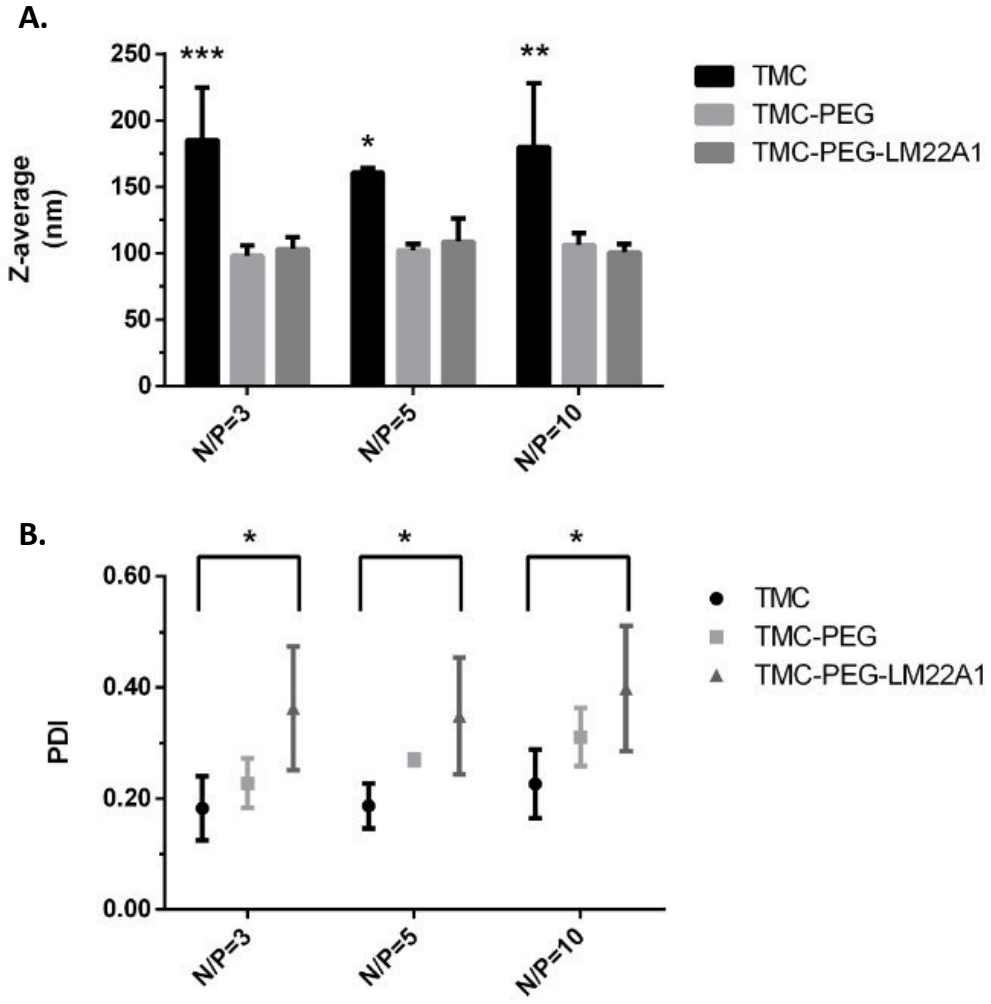

Figure 3. 2- DLS analysis of TMC, TMC-PEG and TMC-PEG-LM22A1 nanoparticles with N/P ratio of 3,5 and10. A. Results of the Z-average (Mean hydrodynamic diameter, based on the size distribution by intensity). B. Polydispersity index. Data from n=3 independent experiments with triplicate measurements each. Asterisks represent statistically significant differences calculated from the two-way ANOVA test. *(*** $p<0.01$, ** $p\leq0.01$, * $p\leq0.05$)*.

In **Figure 3.2,** the Z-average (mean hydrodynamic diameter) and the PDI of the TMC, TMC-PEG and TMC-PEG-LM22A1 nanoparticles are presented.

Regarding its hydrodynamic diameter, it appears that overall, the polyplexes of the analyzed polymers were within a range of 140-230 nm for unPEGylated and 90-110

nm for PEGylated TMC. For all the polyplexes studied, no significant variations were found between the different N/P ratios. The TMC polyplexes had the largest size in comparison to the other polymers, with an average size between the various NPs of 175.4 ± 31.1 nm. After PEGylation, the TMC size decreased, indicating that it improves the polyplexes condensation. Due to the similarity of the results obtained for TMC-PEG and TMC-PEG-LM22A1, it was possible to conclude that the incorporation of the LM22A1 peptide in the polymer structure does not affect the nanoparticles size. Furthermore, both (sizes) were in the order of 100 nm, which is within the range postulated as appropriate for an efficient cell uptake and associated to prolonged blood circulation, although there are other factors besides size that influence these properties.[93,104] The reduction in size after PEGylation could be due to the hydrophilic and flexible nature of the PEG chains, that collectively function as an stabilizing electrostatic shield and lead to the formation of a tightly interfacial hydration layer around the nanoparticles, that may result in their compaction. [121-123] Nevertheless, it is described in the literature that this size reduction effect by PEG is not ubiquitous, being dependent on the type of nanoparticle associated and physical-chemical properties of the PEG itself such as its molecular weight, chains conformation and chemical modifications. It is even reported that high molecular weights of PEG generally promote an increase in the nanoparticles size. [121,123,129]

The polydispersity index characterizes the size distribution of the nanoparticles. It is commonly considered that PDI values greater than 0.7 indicate a high polydispersity and values less than 0.1 correspond to a narrow size distribution.[127,130] However, for polymer nanoparticles, a PDI equal to or less than 0.3 is considered quite acceptable and indicates a relatively homogeneous distribution population.[131]

In the **Figure 3.2 B** it is noted that, as occurred for the Z-average results, there were also no significant variations in the PDI values between the different N/Ps within each polymer. It was possible to conclude that the TMC and TMC-PEG nanoparticles presented a moderately monodisperse size distribution, with mean PDI values in the order of 0.198 ± 0.048 and 0.262 ± 0.047, respectively. Moreover, for the different N/Ps analyzed, there were no statistically significant differences between these two polymers.

Regarding the TMC-PEG-LM22A1 nanoparticles, there was a high variability in the PDI values, with mean of 0.369 ± 0.091 and with a statistically significant increase in comparison to the PDI values obtained for the TMC counterpart at all N/Ps. It would be important to further evaluate the TMC-PEG-LM22A1 nanoparticles to confirm if these variations in PDI values between different synthesis and experiments are maintained.

3.2.2 Zeta Potential

The zeta potential corresponds to the electrostatic potential in the double layer interfacial formed by oppositely charged counterions around the nanoparticles in solution and in DLS it is obtained through the velocity which the nanoparticle moves to the electrode with opposite charge in the cell. This property indicates the surface charge of the nanoparticles and its magnitude allows to predict their stability in solution. It is considered that nanoparticles with an absolute zeta potential greater than ± 30 mV are stable in solution due to repulsive electrostatic interactions between them, whereas for values within this range, can suffer aggregation phenomena (if they are not sterically protected).[132-133]

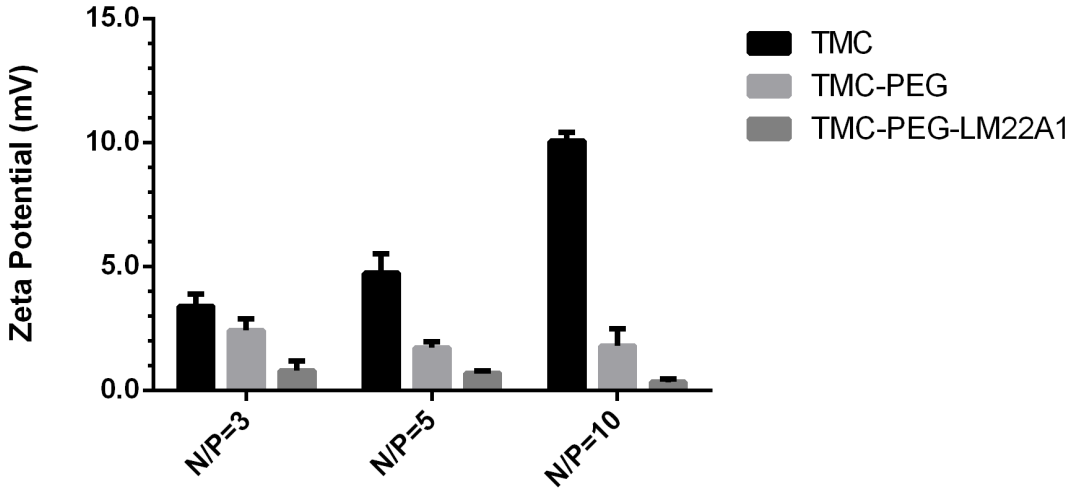

Figure 3. 3- Zeta potential analysis of TMC, TMC-PEG and TMC-PEG-LM22A1 polyplexes with N/P ratios of 3, 5 and 10, determined by DLS. Results from n= 2 independent experiments with triplicate measurements each.

Figure 3.3 demonstrates that the zeta potential of the nanoparticles was positive as expected considering the polymers under study, although in different magnitudes. For the TMC nanoparticles, there was an increase in the zeta potential along with the N/P ratios, which was already expected, since there was an increase in the amount of positive charged polymer present. While, for TMC-PEG and TMC-PEG-LM22A1, this parameter decreased, with no pronounced alterations between the N/P ratios. These effects might be due to the shielding provided by the PEG chains. This surface charge reduction does not necessarily imply a greater probability or tendency to experience aggregation, at least for TMC-PEG nanoparticles. In fact, it is reported that PEG provides stability against aggregation in manner other than electrostatic repulsions. This polymer is known to decrease the aggregation of nanoparticles through steric repulsion.[134]

For TMC-PEG-LM22A1 nanoparticles, the reduced zeta potential is evident. These results, along with the PDI increase, may indicate that aggregation may have occurred, although possibly on a small scale since there were no significant fluctuations in the average size compared to the other polymers. Another possibility could be that the mimetic confers an additional complexity to the nanoparticle and may alter its surface properties.

3.3 Evaluation of TrkB Phosphorylation

In this section, the effect of the free mimetic LM22A1 and LM22A1-Cys on activation of TrkB receptors, in comparison to BDNF and the commercial mimetic LM22A4, was studied in primary mouse neuronal cortical cell cultures (NCCC) and in HT22-GFP cell lines. For this purpose, three different methodologies were performed: 1) Immunocytochemistry (ICC), 2) ELISA and 3) Western Blot, which underwent several optimizations of the experimental conditions over time.

The NCCC cells were derived from the brain cortex of E16.5 C57BL6 mouse embryos and HT22-GFP cell strain resulted from the transfection of the immortalized neuronal hippocampal mouse HT22 cell line with a purified plasmid with a coding sequence for the TrkB receptor fused to a GFP gene (TrkB mEGFP). These last cells present a low expression of TrkB-EGFP (dim), having been selected through successive sorting cycles, by Fluorescence-activated Cell Sorting (FACS) technique. The dim cells were selected over high fluorescent cells in order to prevent activation of the receptor under unstimulated conditions.

3.3.1 Immunocytochemistry

Immunocytochemistry was used as a qualitative approach to investigate the presence, distribution, and co-localization of phosphorylated TrkB receptors, as well as to identify the differences between the different stimuli.

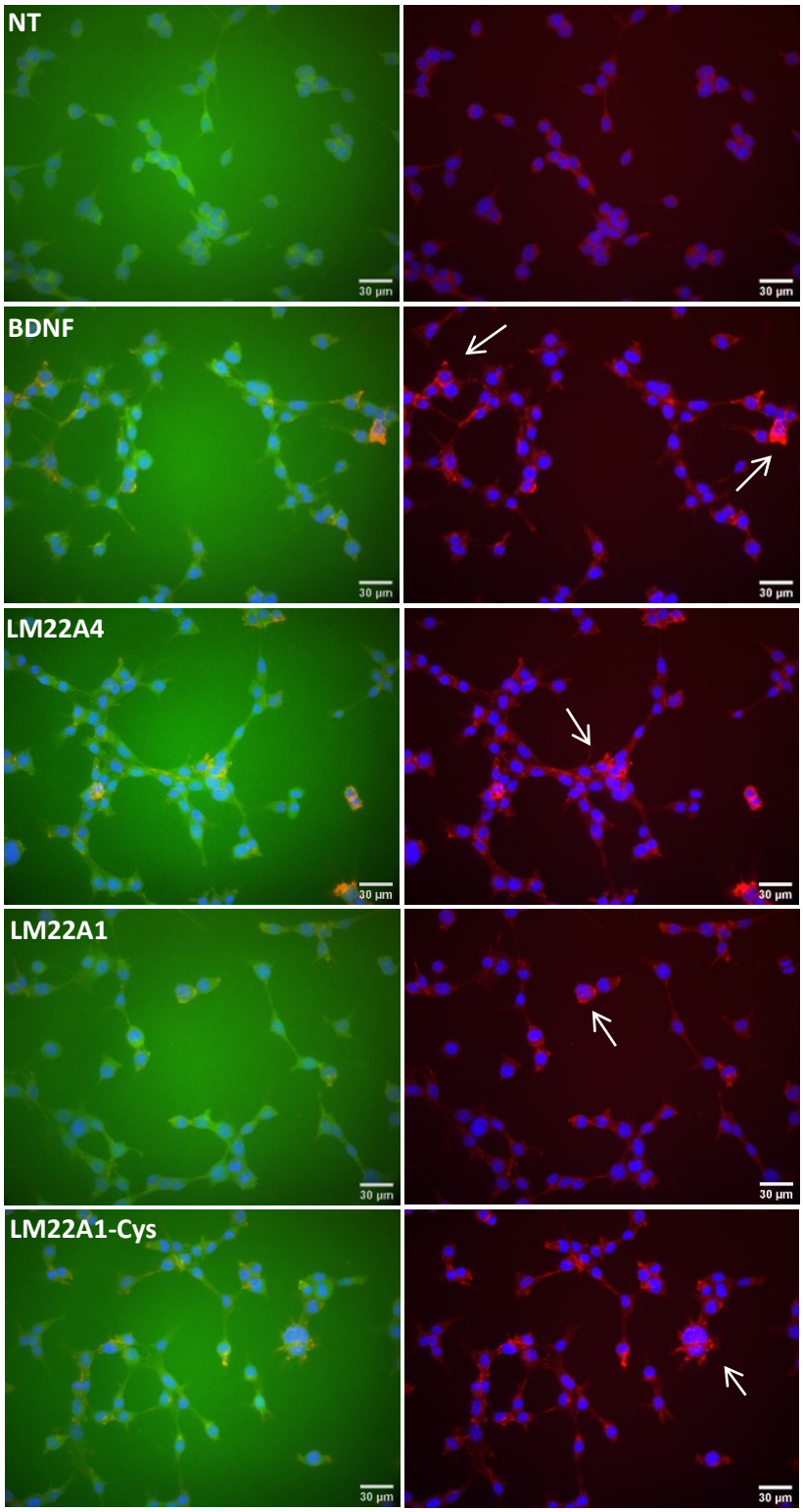

Figure 3. 4- HT22-GFP cells non treated (NT), or treated with BDNF, LM22A4, LM22A1 and LM22A1-Cys. The left column shows the merged images with the EGFP signal (green; recombinant TrkB receptors), DAPI (blue; nuclei) and alexa fluor 488 (red; phosphorylated TrkB receptors). The right column presents the same images with the nuclei (blue) with phosphorylated TrkB receptors (red). The images were acquired by fluorescence microscopy.

Figure 3.4 the images of the stimulated HT22-GFP cells are presented. It was observed that the EGFP signal was low, which is consistent with the cell strain selected for analysis. Although the exposure time was increased, the signal is still low. Nevertheless, for all conditions it was also possible to observe the co-localization between the phosphorylated form of TrkB receptors (in red) and the recombinant TrkB receptors (EGFP fluorescence).

In the non-treated cells, it appears that there is a basal level of phosphorylation of the TrkB receptor, which indicates that cells may have internal stimulus that induce the activation of the receptor. Regarding cells treated with BDNF (positive control), there was a pronounced increase in phosphorylation of TrKB receptors compared to the control showing a high-density fluorescent signal (represented by arrows). However, for mimetic induced stimuli, a qualitative analysis, showed a variable increase for the TrkB receptor. While in some cells there were no observable differences in comparison to NT, in others there was an increase in phosphorylated receptor (**Figure 3.4**) although not as high as BDNF, since they are partial agonists. When comparing the different mimetics we can denote that LM22A4 (commercial) and the modified LM22A1-Cys (used in TMC functionalization synthesis) had more distinguishable increase than the unmodified LM22A1 mimetic (original as in Massa et al, 2010).

Immunocytochemistry was also performed for NCCC primary cells, which were subjected to the same stimuli used for HT22-GFP cells. In addition to the staining of the phosphorylated TrkB receptors, antibodies against β3-tubulin were also used. This protein is present almost exclusively in neuronal microtubules, being important for analyzing the overall morphology of NCCC cells, as well as for assessing the distribution of ph-TrkB receptors throughout the cytoskeleton. [135]

Observing the **Figure 3.5**, it can be concluded that there were no significant changes in the cell's morphology for the different stimuli. Moreover, for all the conditions under study, it was observed that ph-TrkB receptors present a punctate distribution along the neurites and the soma.

The untreated NCCC cells also have a basal level of phosphorylation of the TrkB receptor. In cells stimulated with BDNF, there was an evident increase in the phosphorylation of the receptor compared to the NT control, with an increase of the red fluorescent signal (arrows). These results are consistent with those obtained for HT22-GFP cells. However, it was difficult to distinguish differences between non-treated and those stimulated with the mimetics.

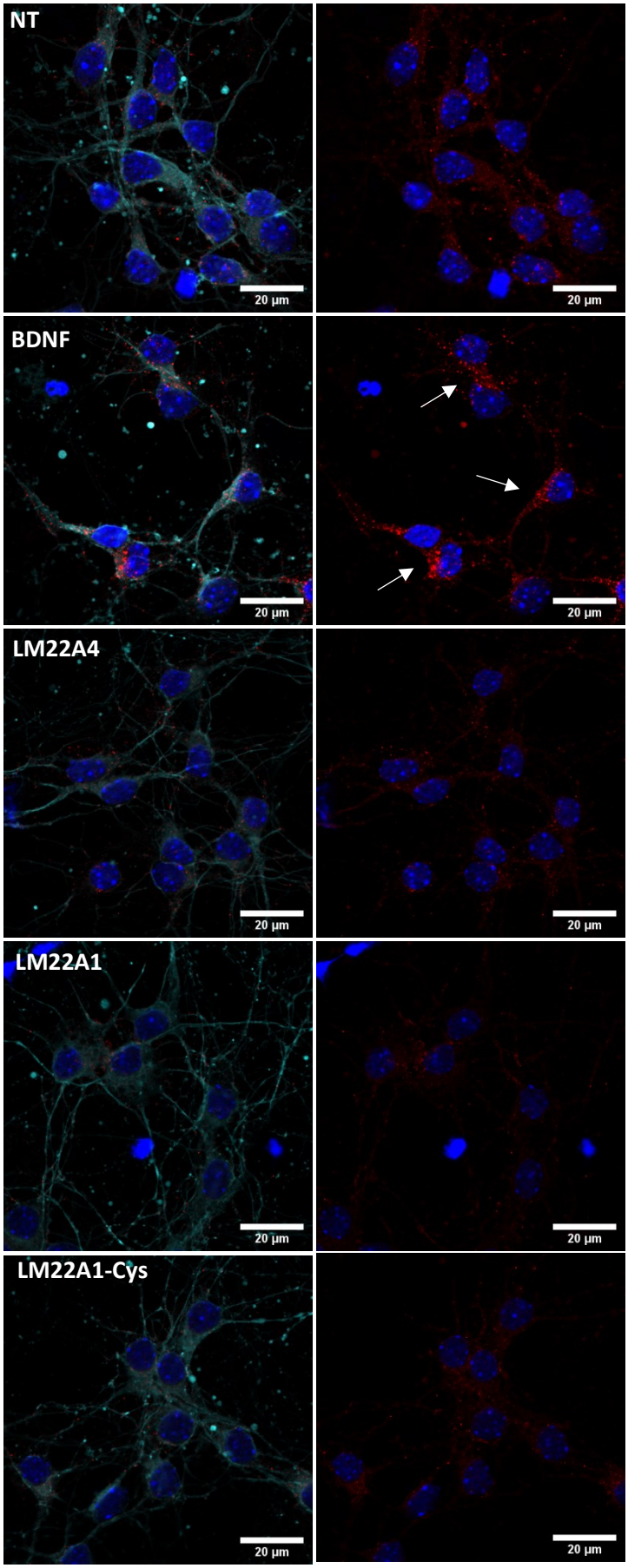

Figure 3. 5-NCCC cells non treated (NT), or treated with: BDNF, LM22A4, LM22A1 and LM22A1-Cys. The left column exhibits the co-localization of ph-TrkB receptors (red), nuclei (blue; nuclei) and β3-tubulin (turquoise). The right column presents the same images with the nuclei and the ph-TrkB receptors. The images were acquired by confocal microscopy.

3.3.2 ELISA Sandwich with Direct Detection

After the qualitative analysis by immunocytochemistry, the quantification of the phosphorylated TrkB receptors in response to stimuli with BDNF and mimetics, was performed with an ELISA Sandwich with Direct Detection assays. This technique is considered a powerful analytic tool for the quantification of proteins, presenting a higher sensitivity than immunocytochemistry.

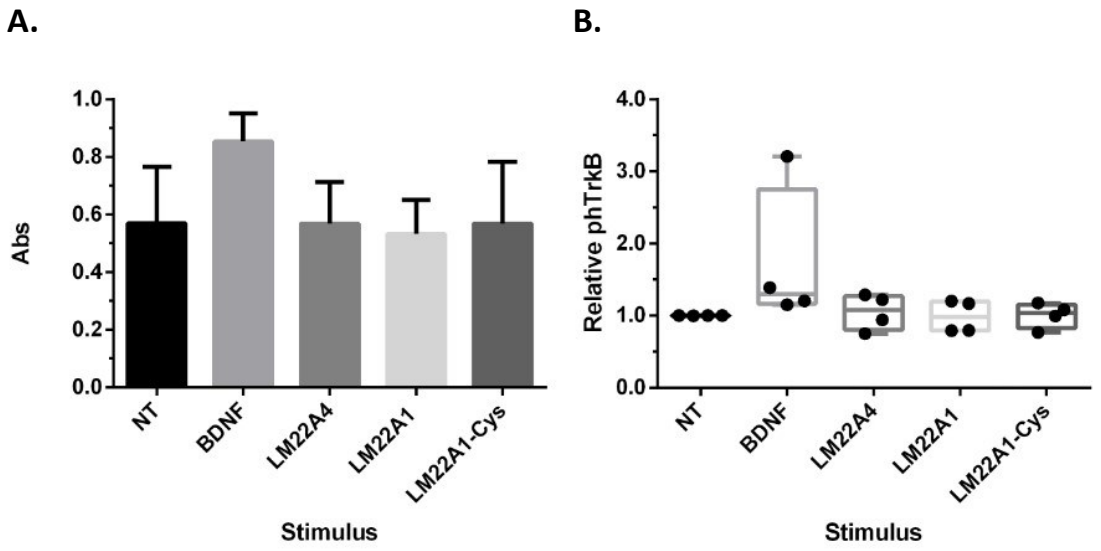

Figure 3. 6- ELISA results for HT22-GFP cells non-treated or stimulated with BDNF or its mimetics: LM22A4, LM22A1, LM22A1-Cys. A. Absorbance values at 370 nm for the detection of the phosphorylated TrkB receptor. B. Fold-change of the TrkB receptor phosphorylation for each condition, calculated in relation to the NT cells absorbance value. Data from n=4 independent experiments with 2 to 4 technical replicates

In **Figure 3.6** the average absorbance values at 370 nm for the detection of phosphorylated TrkB is presented for HT22-GFP cells from 4 independent experiments (A, left chart), and the respective fold changes (B, right chart).

In these experiments, there were no statistically significant differences in the levels of phosphorylation of the TrkB receptor between treated and untreated cells. For the BDNF stimulus, this result was not expected, since it is described as an agonist with high affinity for the TrkB receptor.

In addition, there was a variable distribution of the fold change values for cells treated with BDNF due to the existence of an independent experiment that showed a 3.2-fold increase in TrkB receptor phosphorylation relatively to the control. This particular experiment was performed under the same conditions as the previous ones. A possible explanation for the observed result was the number of cell passages, which was lower for the referred experiment.

If the influence is in fact the lower cell passages, a possible reason would be a lower basal phosphorylation level of the receptor during cell culturing, making cells more responsive when stimuli was added. However, it is necessary to conduct further studies regarding the influence of the cell passages number and their responsiveness to BDNF in order to confirm this hypothesis. Nevertheless, there were no differences for mimetics in that particular experiment, presenting no significant fold change in comparison to NT.

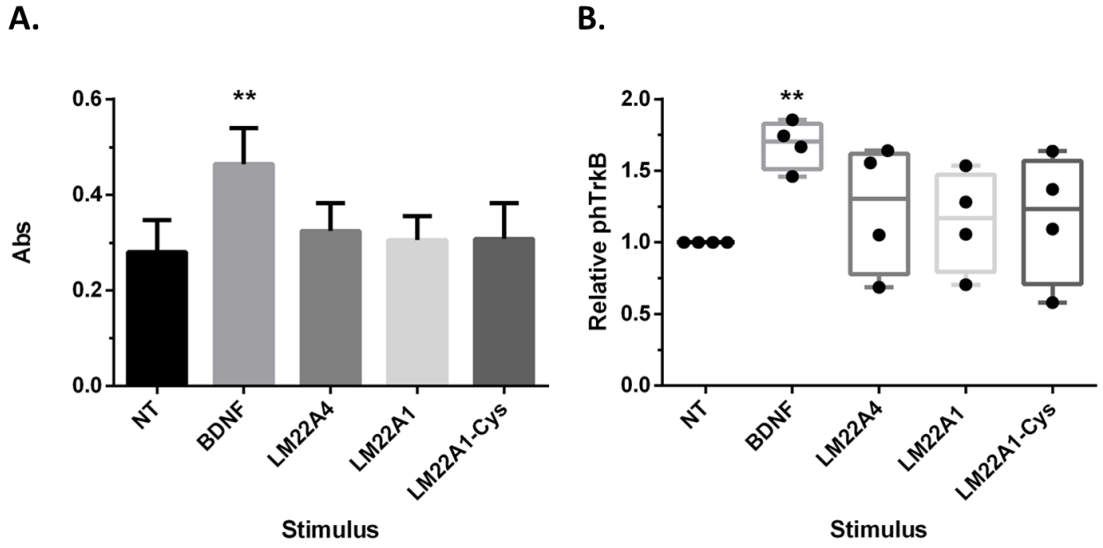

Figure 3. 7- ELISA results for NCCC cells non-treated (NT) or stimulated with BDNF or its mimetics: LM22A4, LM22A1, LM22A1-Cys. A. Absorbance values at 370 nm for the detection of the phosphorylated TrkB receptor. B. Fold-change of the TrkB receptor phosphorylation for each condition, obtained in relation to NT cells. Data from n=4 independent experiments with 2 to 4 technical replicates. Asterisks represent statistically significant differences between treated versus NT cells (**, p≤0.01)

The same assay was also performed for NCCC cells, obtaining different results from those observed for HT22-GFP cells. From **Figure 3.7**, it is possible to verify that there was a statistically significant increase in phosphorylation of the TrkB receptor with the treatment with BDNF compared to untreated cells, with an average fold increase of 1.68.

Furthermore, there were no significant differences among the different mimetics, nor in their relation to control, although with some variability between experiments. Even though there is no statistically significant difference in the phosphorylation of TrkB for the mimetics, there were independent experiments where a small response to the mimetics was observed, with a fold change of 1.4-1.5. These results may be indicative that there may be a lack of robustness in the response to mimetics, in the ELISA technique itself or even in the experimental design and more optimizations could be needful. It was reported in the literature that there were no alterations in the phosphorylation levels of

the TrkB receptor in primary cortical neurons stimulated for different periods of time with the LM22A4 mimetic, through the analysis by ELISA Sandwich.[136]

3.3.3 Western Blot

Considering that in the previous methodologies there were no significant changes in the effect of mimetics on the phosphorylation of the TrkB receptors, we performed the Western Blot technique, which may be more sensitive. Additionally, in these assays, it was also quantified the phosphorylation of the extracellular signal-regulated kinases 1 and 2 (ERK 1/2), phosphorylation, which is described as a molecular downstream event after the TrkB receptors activation.[137]

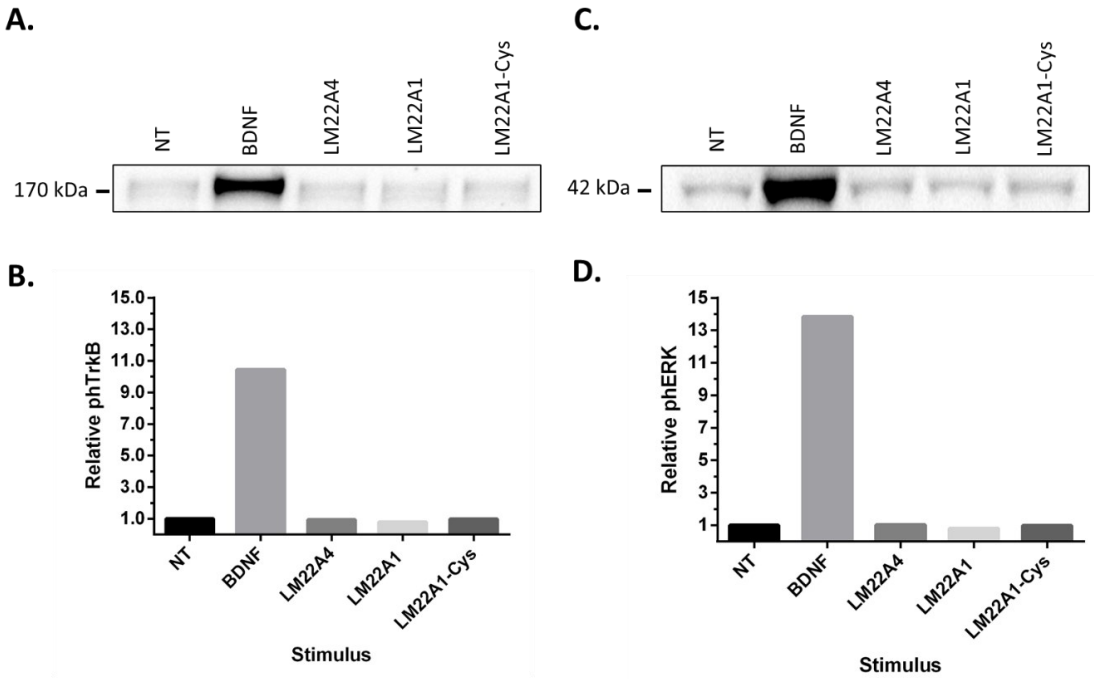

Figure 3. 8- Immunoblot analysis for HT22-GFP cells non treated (NT) or incubated with BDNF or LM22A4, LM22A1 and LM22A1-Cys compounds. A. Bands of the phosphorylated TrkB-receptor (170 kDa) and B. Quantified fold changes compared to NT cells. C. Phosphorylated ERK2 protein band and D. Quantification represented as fold variations. Data obtained from n=1 independent experiment.

In the Western blot assay, some optimizations were made in the HT22-GFP cells conditions. Cells were analyzed at a lower passage (P5), with a density lower than that used in ELISA. Low-density cells may be more responsive to the stimuli.

The immunoblots of the phosphorylated proteins TrkB (170 kDa) and of ERK 2 (42 kDa) are represented in **Figure 3.8**. The ph-ERK1 bands (44 kDa) are not shown, as these were less pronounced. The respective values of the fold increase (stimuli relative to the untreated sample) were normalized by dividing the volume of each band

of the phosphorylated proteins by the volume of total proteins with a selected band with in ponceau stained membrane blots (**Figure A.4**)

For the HT22 cells stimulated with BDNF, there was a fold increase of 10.5 for phosphorylated TrkB receptors compared to the NT control, which demonstrates the sensitivity of this technique. Concomitantly, there was also an increase in ERK2 phosphorylation, which is consistent with the described mechanism of action of BDNF in binding and activating the TrkB receptor, which consequently induces intracellular signaling pathways such as MAPK/ERK.

Regarding the stimulus with mimetics, the levels of these phosphorylated proteins remained unchanged. Although only one independent experiment was carried out, these particular results were in conformity with those obtained by ELISA.

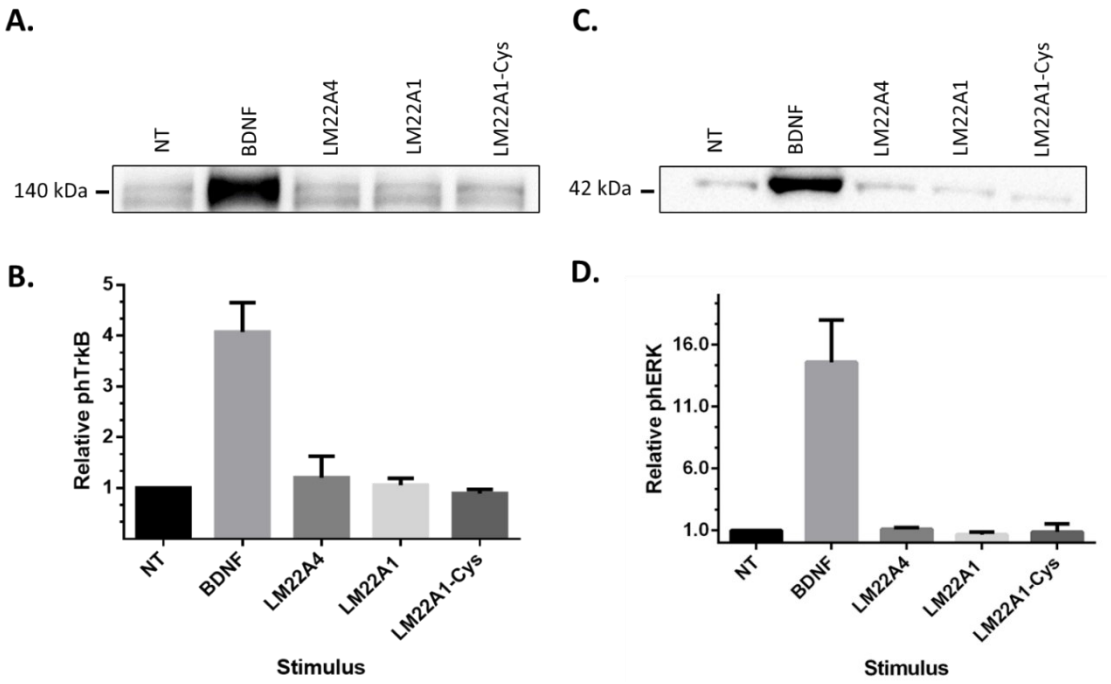

Figure 3. 9 -Exemplificative Immunoblot analysis for NCCC cells cultured for 7 days *in vitro*, non-treated or incubated with BDNF or LM22A4, LM22A1 and LM22A1-Cys compounds. A. Detection of the phosphorylated TrkB receptor (140 kDa) and respective quantified fold changes compared to NT cells (B.). C. Identification of phosphorylated ERK2 protein and its signal quantification represented as fold variations (D.). Results obtained from n=2 independent experiments.

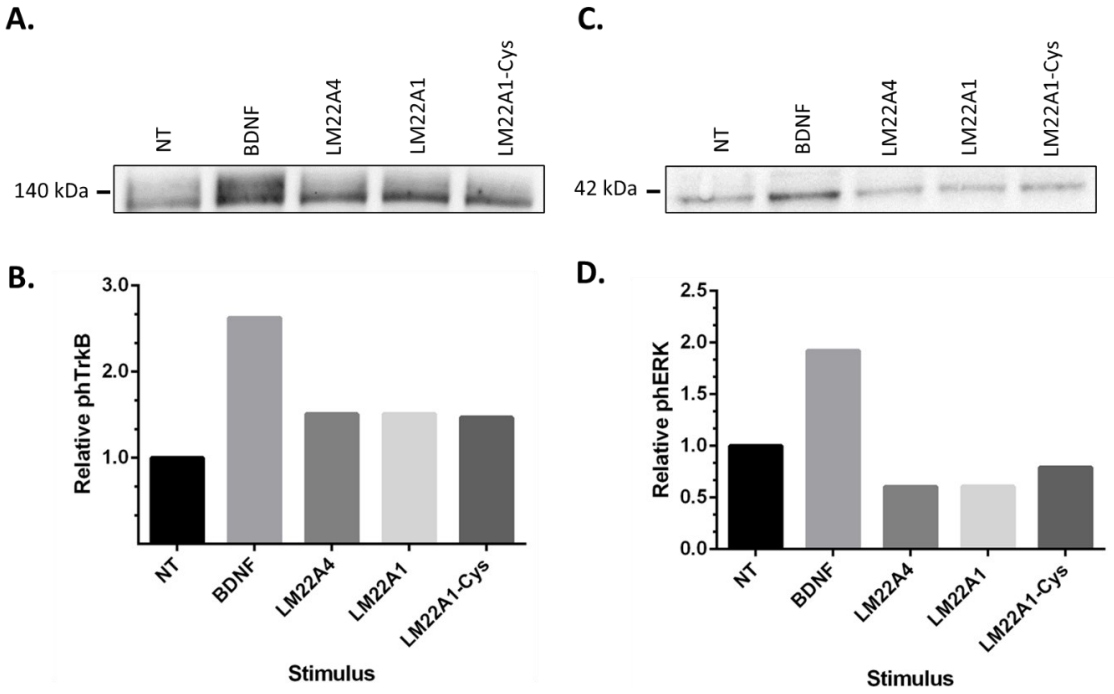

Figure 3. 10- Immunoblot analysis for NCCC cells cultured for 14 days *in vitro*, non-treated or incubated with BDNF or LM22A4, LM22A1 and LM22A1-Cys compounds. A. Detection of the phosphorylated TrkB receptor (140 kDa) and respective quantified fold changes compared to the untreated cells (B.). C. Identification of phosphorylated ERK2 protein and its signal quantification represented as fold variations (D.). Data from n=1 independent experiment**.**

The western blot assay was also performed for NCCC cells, cultured for different periods of time (7 or 14 DIV), before the stimuli addition. The cell stimulation by BDNF and its mimetics was the same as for the HT22-GFP cell strain. For the 7 DIV NCCC (**Figure 3.9**), it was found that the increase in phosphorylation levels of TrkB receptors after BNDF stimulus, was higher when compared to the response for the 14 DIV NCCC cells (**Figure 3.10**) (4 fold and 2.5 fold respectively). For ph-ERK levels, this difference was confirmed and even more pronounced at 7 DIV. These differences may be due to the fact that NCCC cells are derived from embryos, being more responsive to neurotrophic factors such as BDNF in the first week in culture to undergo maturation. However, more experiments must performed to statistically confirm this correlation.

For 14 DIV, there is a slight increase in phosphorylation levels for all mimetics (average fold of 1.4). However, it was not accompanied by alterations in ERK levels. This is not expected, as it is described that with treatment with mimetics, small increases in phosphorylation of the TrkB receptor are reflected in a robust increase in ERK phosphorylation.[62]

In the case of 7 DIV, surprisingly, there were no changes in phosphorylation for both TrkB and ERK2 proteins, despite the increased sensitivity to the stimulus with

BDNF. In one of the experiments, there was a fold increase of 1.5 in ph-TrkB for the treatment with LM22A4 (**Figure A.6**), indicating that there may be variability in mimetics response, as observed by ELISA.

Comparing the Western Blot results of HT22-GFP cells and NCCC cells, a higher phosphorylation level of TrkB with the BDNF stimulus was observed for the cell strain. For the mimetics stimuli, only a sligh increment ocurred for the NCCC. Additional experiments are needed to confirm if these are significant. Overall, it was expected that the increase with the mimetics would occur to a different extent since it is described in the literature that the commercial mimetic LM22A4 leads to a more effective response compared to LM22A1.[62]

New optimizations of the experimental procedure should be carried out for both the HT22-GFP cells and NCCC primary culture., such as increasing the starvation period to 2 hours and analyzing other concentration of mimetics.

3.4 Glutamate-induced Oxidative Stress

3.4.1 Quantification of SOD2 Expression

Oxidative stress is one of the main mechanisms responsible for neuron injury associated with ischemic stroke. One of the main goals of this thesis was to attempt to prevent this neuronal damage by using nanoparticles capable of inhibiting mir 145, which is responsible for the reduction of SOD2 expression in a pos-ischemic context. Yet, before the neuroprotective effect of the anti-mir 145 of the nanoparticles can be evaluated, it is essential to establish the conditions for the ischemic cascade *in vitro*, more precisely to increase oxidative stress by the reduction of SOD2 levels. For this purpose, SOD2 mRNA expression was analyzed in HT22-GFP cells treated with varying concentrations of glutamate for 24h.

Besides triggering the excitotoxicity through the activation of ionotropic receptors, the glutamate in high extracellular concentrations also promotes the inhibition of cysteine uptake by a glutamate/cysteine antiporter. This results in severe repercussions at molecular level such as depletion of the antioxidant glutathione synthesis and consequent accumulation of ROS, depolarization of mitochondrial membrane potential and mitochondrial influx of calcium and ultimately oxidative stress. As HT22-GFP cells do not express functional glutamate ionotropic receptors, they represent a model for studying exclusively the oxidative stress induced by glutamate. In addition, it was proven for HT22 cells that SOD2 has a crucial role in the protection against the glutamate-induced oxidative stress.[138-139]

Initially, the validation of the three specific primers designed for SOD2 and the housekeeping genes YHWAZ and HPRT was pursued, through the evaluation of real time-PCR amplification efficiency. For this purpose, a 10-fold serial dilution of a control sample of untreated HT22-GFP cells was analyzed by RT-qPCR, followed by the generation of a standard curve with the logarithm of the starting quantities of RNA target, in function of the obtained cycle threshold values (Cq). The efficiency (E) was calculated from the linear regression slope, according to the Equation 3.1:

$$E = -1 + 10^{(-1/slope)} \qquad \text{(Eq. 3.1)}$$

Ideally, the amplification efficiency should be 100%, which would correspond to the product duplication for each replication cycle (exponential replication cycle). Nevertheless, a range between 90-110% of efficiency (-3.10 ≤slope≤ -3.58) is commonly accepted. The values of the coefficient of determination (R^2) must be included in the range of 0.98-1.0. In addition to an adequate efficiency, it is crucial that the primers selected for the RT-qPCR experiment have similar values for this parameter for an accurate quantification.

In **Figure 3.11**, the standard curves obtained for the different primers under study are represented - SOD2 primers (A, B, C) and YHWAZ and HPRT housekeeping genes. As shown in **Figure 3.11**, the SOD2 primers had amplification efficiencies that were within the acceptable range. The SOD2 C primer was selected for the subsequent RT-qPCR assays since it had an efficiency value closer to 100%, accompanied with a good R^2 value. In relation to the housekeeping genes, the YHWAZ was the only with adequate efficiency (101.4%), with a similar performance relatively to SOD2 C.

SOD2-A (E=93.1%, R^2=0.996)

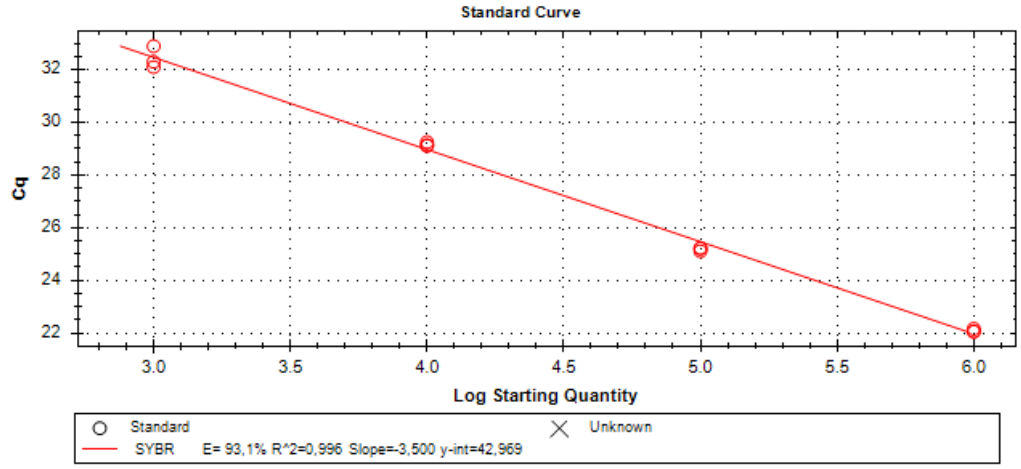

SOD2-B (E=95.5%, R^2=0.993)

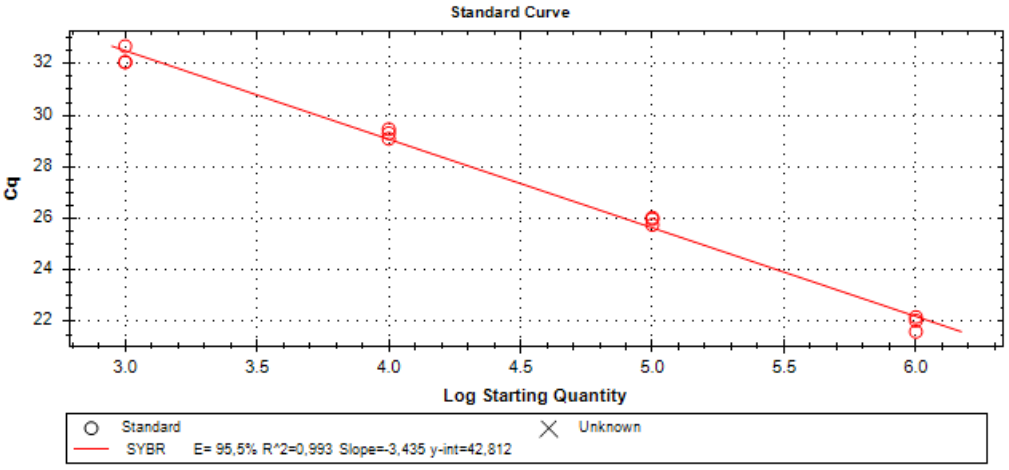

SOD2-C (E=98.0%, R^2=0.995)

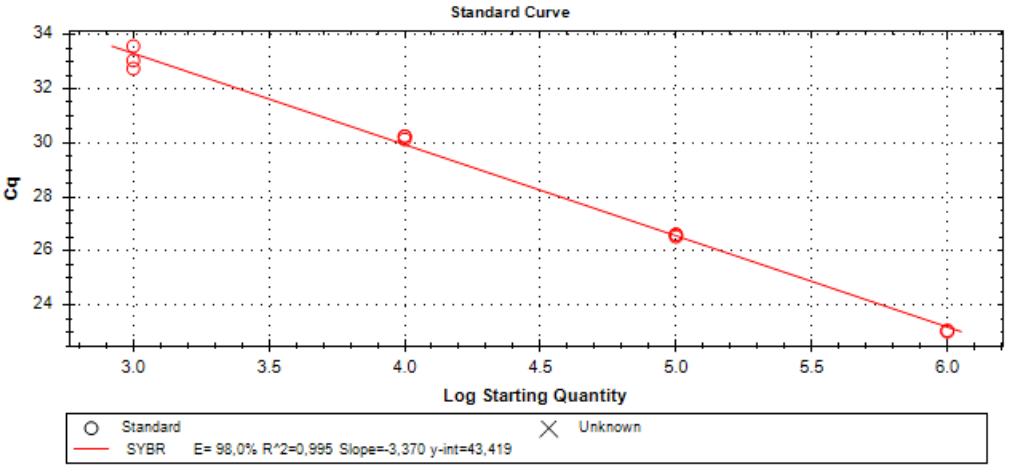

HPRT (E=112.1%, R^2=0.996)

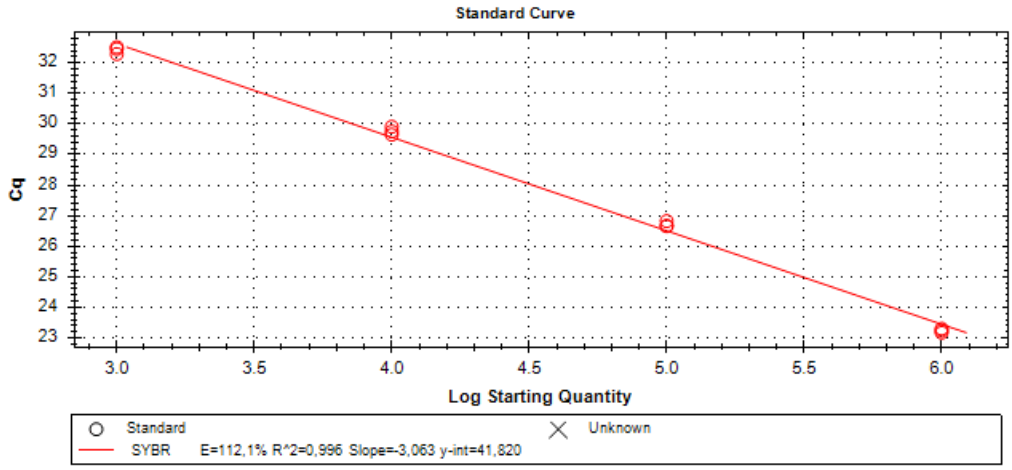

YHWAZ (E=95.5%, 0.995)

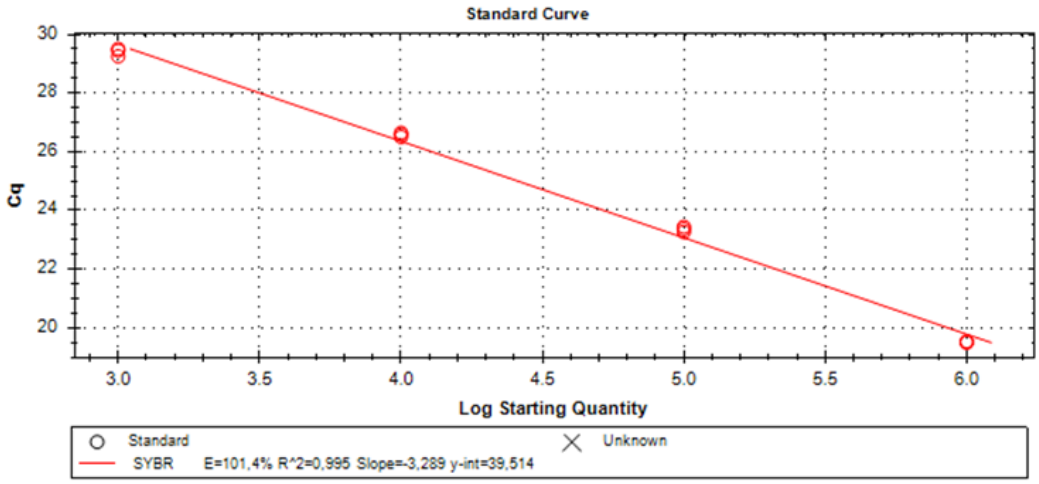

Figure 3. 11 Standard curves for the evaluation of primers of the RT-qPCR reaction efficiency for SOD2 primers (A, B, C) and housekeeping genes (YHAWZ and HPRT). The values of efficiency and the respective coefficient of determination are located on top of each graph. Results obtained from CFX Maestro Software.

After primer selection, relative quantification of SOD2 mRNA levels was performed in HT22-GFP cells treated with glutamate (8,4,2,1,0.5 and 0.25 mM) and menadione (8 and 4 µM), which was tested as a possible positive control. The concentrations chosen were based on those used for HT22 described in the literature and from previous studies done by our research group.

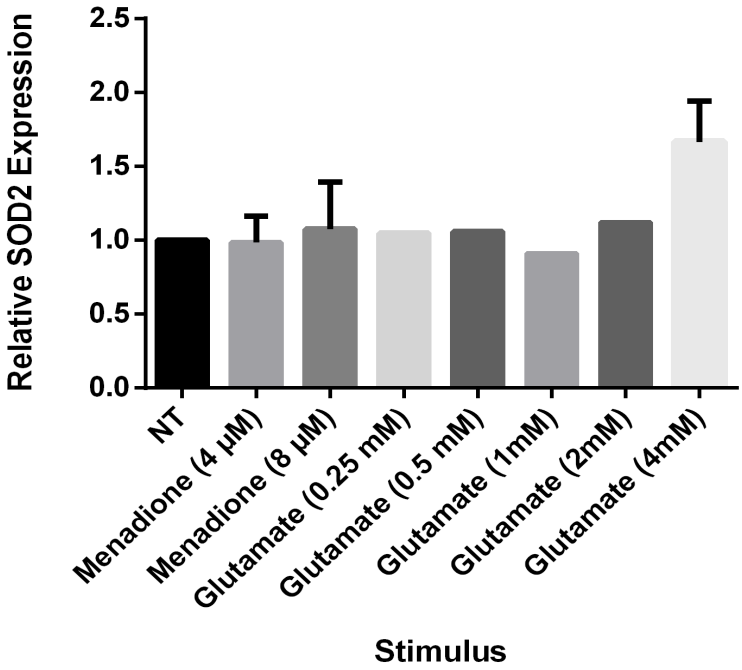

Figure 3. 12- Relative SOD2 expression in HT22-GFP cells not treated (NT) or treated with menadione (4 and 8µM) or glutamate (4,2,1,0,5,0.25 mM) for 24 hours, obtained by RT-qPCR. Two independent experiments were performed for stimuli with menadione (4 and 8µM) and 4 mM glutamate, each with 3 technical replicates. For the remaining concentrations, an independent experiment was carried out with also 3 technical replicates. The data were processed using the $2^{-\Delta\Delta Cq}$ method.

Following the incubation with glutamate at 8 mM for 24 hours, a high loss of cells occurred and a pronounced alteration in morphology of the remaining cells was observed, more precisely in the loss of neurites (data not shown). For this reason, this concentration is not shown in the graph of **Figure 3.12**. For the 4 mM glutamate stimulation these responses were also verified, although in a lower severity. Thus, we have observed a rise in the SOD2 mRNA levels as represented in the graph. These morphological changes of neurites and cell death are described in the literature for HT22 cells, more precisely for higher glutamate concentrations (greater than 4 mM for at least 8 hours of treatment).[139-141]

For the remaining concentrations tested, there were no alterations in the SOD2 mRNA levels compared to the control group. Since only one independent experiment was performed, more analysis are needed to draw solid conclusions. Moreover, later time points ought to be analyzed in order to evaluate late response to the glutamate stimulus. Another hypothesis is that for the same incubation time, SOD2 levels will decline later, requiring further study.

Menadione is also described in the literature as a strong oxidative stress inducer in several cell types. This compound is converted by reducing enzymes such as cytochrome P450 reductase and mitochondrial NADH-ubiquinone oxidoreductase into

an unstable semiquinone radical, which can undergo reoxidation in the presence of oxygen, with a rapid production of mitochondrial superoxide. In HT22 cells it is described that menadione promotes mitochondrial dysfunction, ATP levels reduction and that SOD-2 has a protective effect against the oxidative effect induced by this compound.[142-143] In another cell line it is associated with the augmentation of SOD2 expression.[142] For this reason, it was decided to test its ability to increase the mRNA SOD2 levels in HT22-GFP cells. Two different concentrations were selected that are expected to lead to a significant increase in mitochondrial ROS in HT22 cells.[143]

As it is depicted in **Figure 3.12**, in the two independent experiments there was no change in SOD2 levels with the stimulus with menadione at 4 and 8 μM. Therefore, it is possible that this compound is not suitable as a positive control, at least for the concentrations and the incubation time tested.

However, as menadione has a very similar biological effect on cells compared to glutamate, it can also be used in an oxidative stress model. In fact, there are studies that investigate the antioxidant effect of ROS scavenging nanoparticles under oxidative stress conditions induced by menadione.[144] Either way, it is important to find a suitable positive control for future SOD2 expression quantifications by RT-qPCR.

3.4.2 Quantification of ROS Production

Considering that for an incubation period of 24 hours, higher concentrations of glutamate resulted in cell death and for lower concentrations no alterations in SOD2 mRNA levels were verified, it would be important to study the production of ROS which in turn should interfere with SOD2 expression. This is important to understand the oxidative stress environment that the cell experiences after glutamate oxidative stress. With this in mind, we decided to measure ROS formation by the use of the $DCFH_2$-DA probe, quantified by flow cytometry. This would allow us to study various concentrations at different time points and define the conditions in which a greater production of ROS occurs, so that SOD2 levels could be tested later.

The DCFH2-DA probe is commonly used to detect intracellular oxidative stress. DCFH2-DA is a non-florescent hydrophobic compound, which when internalized in cells is hydrolyzed by cellular esterases into a non-fluorescent polar derivative $DCFH_2$, whose subsequent oxidation by ROS and other oxidizing agents results in a highly fluorescent DCF product.[145]

The production of ROS in HT22-GFP cells stimulated for 24 hours with glutamate with concentrations of 4, 2, 1, 0.5 and 0.25 mM was analyzed. In addition, the highest

concentrations (4, 2 mM) were also tested for an incubation period of 2 hours. The Fenton's reagent (H2O2 solution with FeSO4) was used as positive control, since it leads to the production of highly reactive hydroxyl radicals. However, the probe used could not be clearly distinguished from the fluorescent spectra of the GFP expressed by the cells. Although there is an increase in the signal intensity with the glutamate stimuli, it is not possible to take clear conclusions with confidence. It was also found that the Fenton's reagent modified the cells morphology. The flow cytometry data is presented in **Figure A.8 and A.9.**

In the future, these assays will have to be repeated using a suitable probe, such as MitoSOX red or the Cellular ROS Assay (Deep Red) (Abcam). This reagent is selective for mitochondria, where it is quickly oxidized by superoxide, forming a fluorescent red product. As its oxidation is prevented by SOD2, this probe is especially useful to verify in the future the neuroprotective effect of the nanoparticles' antagomir 145 in increasing SOD2 levels and consequent decrease in oxidative stress induced by glutamate.

In addition to the evaluation of SOD2 expression by RT-qPCR, it would also be important to quantify the protein levels by techniques like Western Blot and to perform SOD2 activity assays. Other conditions that elicit oxidative stress apart from glutamate can also be tested, such as induction of oxygen glucose deprivation. In fact, there is a study that demonstrated a decrease in SOD2 expression after 3 hours of oxygen glucose deprivation, followed by 24 hours of reoxygenation.[146]

3.6 Cellular Internalization of Polymeric Nanoparticles: TMC, TMC-PEG and TMC-PEG-LM22A1

The cellular internalization capacity of the nanoparticles resulting from the complexation of the TMC-PEG and TMC-PEG-LM22A1 polymers with the epifluorescent miRIDIAN microRNA Hairpin Inhibitor Transfection Control with Dy547 (25 and 12.5 nM) with the N / P ratios of 5 and 10, was also evaluated. This assay was performed in HT22-GFP cells in contact with the nanoparticles for 6h. After the cells were stained with Hoechst (nuclei) and Alexa Fluor-647 phalloidin (F-actin).

In figures **3.13 and 3.14** the results from the internalization experiment are presented for the micro-RNA concentration of 12.5 nM, while for the 25 nM concentration the confocal images are attached in annex (**Figure A.10 and A.11**).

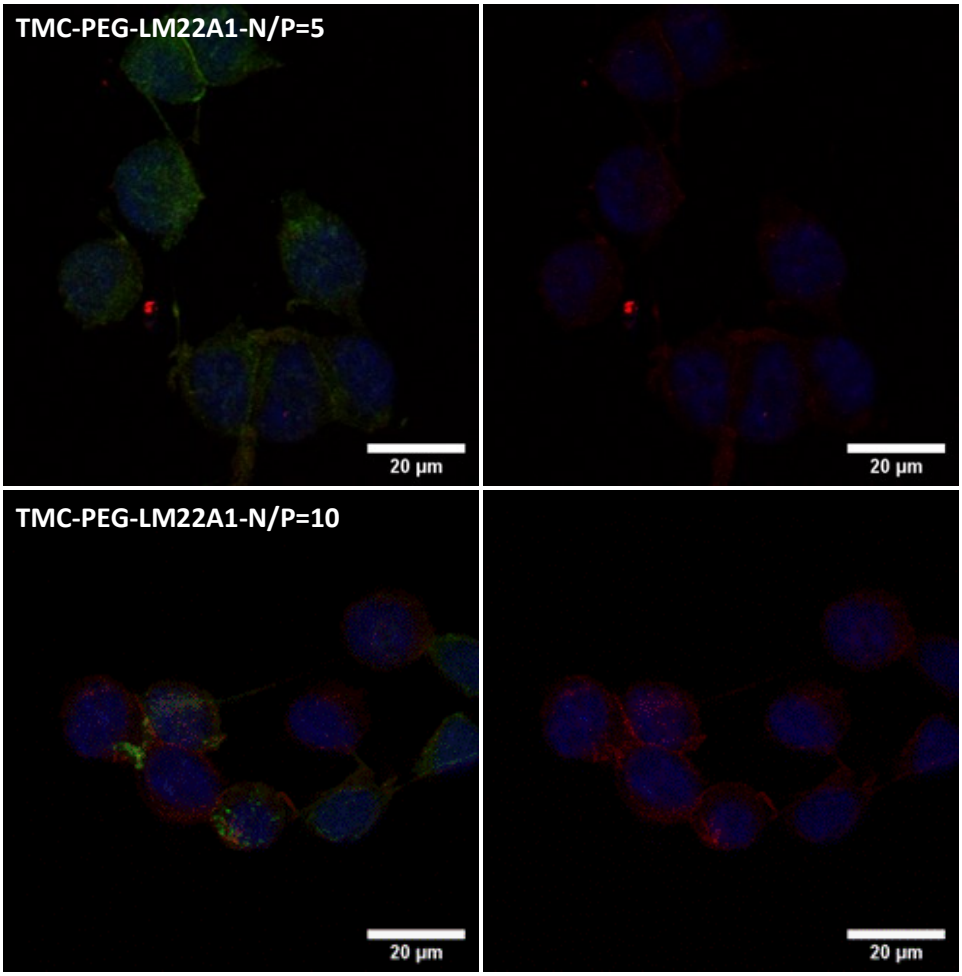

Figure 3. 13- HT22-GFP cells treated with nanoparticles of TMC-PEG-LM22A1 complexed with microRNA Dy547 (12.5 nM), at N/P ratios of 5 and 10. The left column exhibit the co-localization of nuclei (blue), F-actin (green) and micro-RNA Dy547 (red). In the right column is presented the same images with the nuclei and micro-RNA Dy547 signal. Images were acquired by confocal microscopy.

For a micro-RNA concentration of 12.5 nM, it seems that there was a higher internalization of TMC-PEG-LM22A1 nanoparticles with N/P = 10 than those with N/P = 5, while for TMC-PEG the opposite occurred. Comparing both concentrations of microRNA under study, it appears that for the higher concentration (25 nM) there was a greater uptake efficiency. It was noticeable that TMC-PEG with N/ P = 5 had a more pronounced internalization than the other nanoparticles. Moreover, the TMC-PEG-LM22A1 nanoparticles appear to have a similar effect for both N/P ratios analyzed. However, it is important to emphasize that in this assay needs to be repeated and further confirmed. Furthermore, due some technical difficulties, such as cell loss, the cell density was not uniform and the NT control and lipofectamin control are missing. It would be important to repeat these experiments also in NCCC cells, since the cell internalization of these nanoparticles is essential to achieve their possible therapeutic effect. It should

also be noted that all comparisons are qualitative analysis, and it is also necessary to proceed with quantitative methods such as FACS.

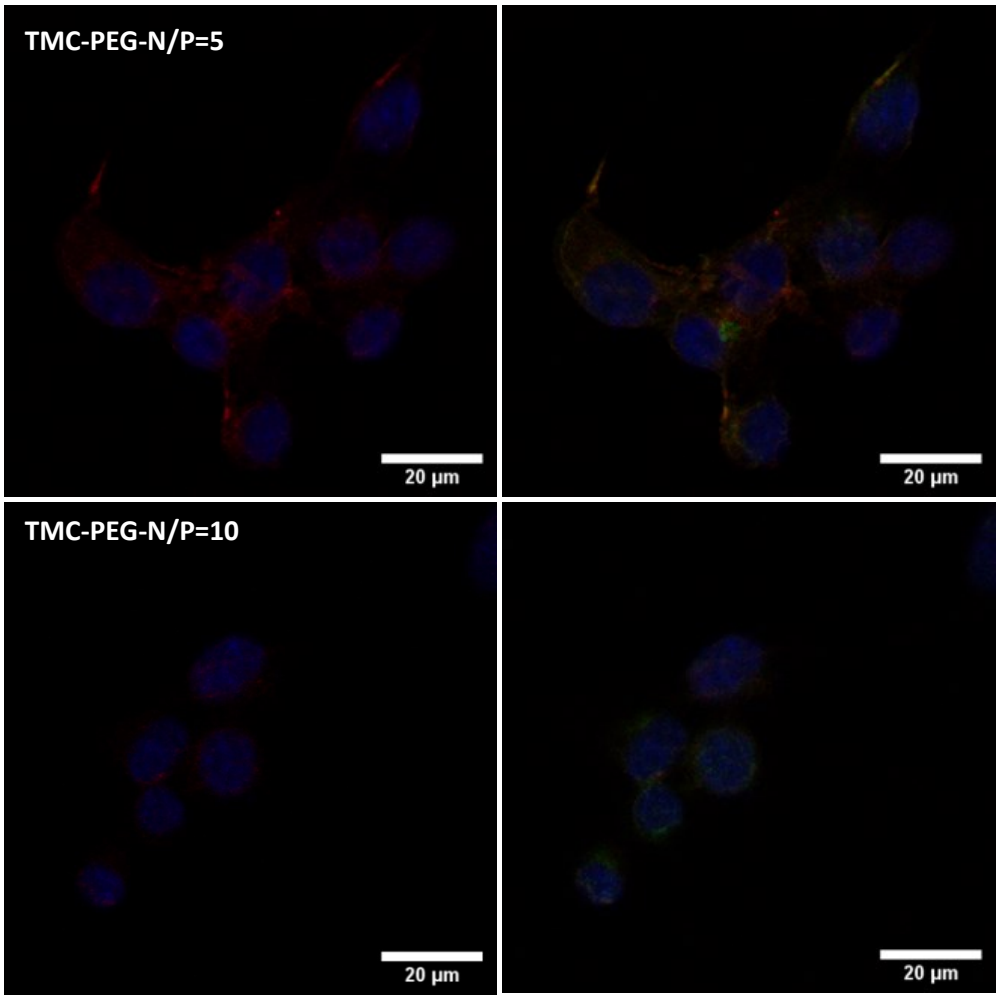

Figure 3. 14- HT22-GFP cells treated with nanoparticles of TMC-PEG complexed with microRNA Dy547 (12.5 nM), at N/P ratios of 5 and 10. The right column exhibit the co-localization of nuclei (blue), F-actin (green) and micro-RNA Dy547 (red). In the left column is presented the same images with the nuclei and micro-RNA Dy547 signal. Images obtained by confocal microscopy.

4 Conclusion and Future Prospects

The present work demonstrated a successful synthesis for TMC-PEG-LM22A1 copolymer synthesis. Using ^{1}H-NMR analysis, it was confirmed that the LM22A1 peptide was successfully functionalized to the TMC-PEG polymer. The analysis by UV/Vis spectroscopy allowed to reinforce this result, which will be further explored in the future. It would be interesting additionally verify the peptide linkage by the measurement of tryptophan fluorescence, or even by an indirect analysis after quantification of the free thiol groups (of the unbound peptide) by Elman´s assays prior to the dialysis process.

Among the studied polymers, the TMC polyplexes had an hydrodynamic size higher than 100 nm, as measured using DLS. It was also verified that with PEGylation, the reduction of this parameter has also occurred. The studied polyplexes presented a relatively homogeneous size distribution, with exception of TMC-PEG-LM22A1 that exhibited variability between experiments. If this result remains in future experiments, it is important to test different experimental conditions for the complexation process such as temperature, buffer, ionic strength or even coacervation agent to improve this parameter. It can be hypothesized that for the TMC-PEG-LM22A1 polyplexes the aggregation phenomena could have occurred to a small extent or in turn this could be a result of peptide contribution to the surface of the nanoparticle. It would be also interesting to analyze the properties of nanoparticles in terms of size, polydispersity and zeta potential to see if these are maintained over time, so as to have information about their long-term stability. In addition, its ability to protect the miRNA within the polyplex for a long period should also be accessed through the treatment of nanoparticles with RNase, followed by stopping the reaction and promoting the degradation of TMC with chitosanase enzymes, and finally, evaluation of the miRNA presence by agarose gel electrophoresis. Additionally, the nanoparticles could also be studied using other techniques, such as transmission electron microscopy.

Regarding the immunocytochemistry, ELISA and Western blot assays of HT22-GFP and NCCC cells, did not confirm the effect of BDNF mimetics regarding the increase in phosphorylation of the TrkB receptor. In the future, optimizations in the experimental stimulus can be optimized such as performing the analysis with different starvation and stimulation time-points and other concentrations of mimetics. Nevertheless, the impact of the mimetic may be pursued in a functional assay with neuronal cells, such as by studying the neuroprotective role after excitotoxicity.

The RT-qPCR assays revealed that for most of the studied glutamate concentrations, there was no significant variation in the SO2 mRNA levels. In the future, HT22-GFP cells

should be incubated with glutamate for a longer period or even, for the same stimulus time, perform an evaluation at different time points to test if SOD2 repression did occur. These tests must be accompanied with measurement of ROS, in order to have information about the severity of oxidative stress induced by glutamate. If positive results are not obtained, other conditions that trigger oxidative stress, such as oxygen glucose deprivation, can also be used alternatively.

Finally, in the internalization assays, robust results were not obtained due to technical difficulties. Thus, it is essential to repeat these procedures for HT22-GFP and for NCCC cells. It would also be important to perform their quantitative analysis by FACS in the case of the cell line and by fluorescence spectroscopy for the primary neuronal culture.

The activation of the TrkB receptor by the TMC-PEG-LM22A1 will be tested when the optimal conditions for free mimetics are optimized.

In turn, the neuroprotective effect of the nanoparticle's cargo - the miR-145 may be tested after determining the appropriate conditions that lead to decreased SOD2 levels. It is also crucial that the nanoparticles have a suitable transfection efficiency to exert their therapeutic effect.

These results are the basis for carrying out more complex studies, such as the nanoparticle performance in organotypic hippocampal cultures, application in BBB *in vitro* models, exploration of mucoadhesive properties and translating into *in vivo* models.

5 Bibliography

1. Organization, W. S. Global Stroke Fact Sheet. https://www.world-stroke.org/publications-and-resources/resources/global-stroke-fact-sheet.

2. Campbell, B. C. V.; De Silva, D. A.; Macleod, M. R.; Coutts, S. B.; Schwamm, L. H.; Davis, S. M.; Donnan, G. A., Ischaemic stroke. *Nat Rev Dis Primers* **2019,** *5* (1), 1-22.

3. Donkor, E. S., Stroke in the 21(st) Century: A Snapshot of the Burden, Epidemiology, and Quality of Life. *Stroke Res Treat* **2018,** *2018*, 1-10.

4. Rajsic, S.; Gothe, H.; Borba, H. H.; Sroczynski, G.; Vujicic, J.; Toell, T.; Siebert, U., Economic burden of stroke: a systematic review on post-stroke care. *Eur J Health Econ* **2019,** *20* (1), 107-134.

5. Lee, S. H., *Stroke Revisited: Diagnosis and Treatment of Ischemic Stroke*. 1 ed.; Springer Singapore: Singapore, 2017; p 377

6. Warlow, C.; Gijn, J. V.; Dennis, M.; Wardlaw, J.; Bamford, J.; Hankey, G.; Sandercock, P.; Rinkel, G., *Stroke:Practical Management* 3ed.; Blackwell Publishing: Massachusetts, 2008; p 998.

7. Barthels, D.; Das, H., Current advances in ischemic stroke research and therapies. *Biochimica et Biophysica Acta (BBA) - Molecular Basis of Disease* **2020,** *1866* (4), 165260.

8. Martini, S. R.; Kent, T. A., Ischemic Stroke. In *Cardiology Secrets*, 5 ed.; Levine, G., Ed. Elsevier: 2018; pp 493-504.

9. Tziotzios, C. D., J.; Walters, M.;, *Stroke in Practice: From Diagnosis to Evidence-Based Management*. 1 ed.; Radcliffe Publishing Ltd: 2011; p 151.

10. Hankey, G. J., Stroke. *The Lancet* **2017,** *389* (10069), 641-654.

11. Sonderer, J.; Katan Kahles, M., Aetiological blood biomarkers of ischaemic stroke. *Swiss Med Wkly* **2015,** *145*, 1-15.

12. Hathidara, M. Y.; Saini, V.; Malik, A. M., Stroke in the Young: a Global Update. *Curr Neurol Neurosci Rep* **2019,** *19* (11), 91.

13. Greer, D. M., *Acute Ischemic Stroke: An Evidence-based Approach*. 1 ed.; John Wiley & Sons, Inc.: New Jersey, 2007; p 248.

14. Hemmen, T. M.; Zivin, J. A., Molecular Mechanisms of Ischemic Brain Disease. In *Molecular Neurology*, 1 ed.; Waxman, G. S., Ed. Elsevier: 2007; pp 177-186.

15. Paciaroni, M.; Caso, V.; Agnelli, G., The concept of ischemic penumbra in acute stroke and therapeutic opportunities. *Eur Neurol* **2009,** *61* (6), 321-30.

16. Lapchak, P. A. Z., J. A., *Neuroprotective Therapy for Stroke and Ischemic Disease*. 1 ed.; Springer, Cham: 2017; p 795.

17. Popa-Wagner, A.; Mitran, S.; Sivanesan, S.; Chang, E.; Buga, A. M., ROS and brain diseases: the good, the bad, and the ugly. *Oxid Med Cell Longev* **2013,** *2013*, 1-14.

18. Khoshnam, S. E.; Winlow, W.; Farzaneh, M.; Farbood, Y.; Moghaddam, H. F., Pathogenic mechanisms following ischemic stroke. *Neurol Sci* **2017,** *38* (7), 1167-1186.

19. Qureshi, G. A.; Parvez, S. H., *Oxidative Stress and Neurodegenerative Disorders* 1ed.; Elsevier: 2007; p 795.

20. Stokum, J. A.; Gerzanich, V.; Simard, J. M., Molecular pathophysiology of cerebral edema. *J Cereb Blood Flow Metab* **2016,** *36* (3), 513-38.

21. Nakka, V. P.; Gusain, A.; Mehta, S. L.; Raghubir, R., Molecular mechanisms of apoptosis in cerebral ischemia: multiple neuroprotective opportunities. *Mol Neurobiol* **2008,** *37* (1), 7-38.

22. Margaill, I.; Plotkine, M.; Lerouet, D., Antioxidant strategies in the treatment of stroke. *Free Radic Biol Med* **2005,** *39* (4), 429-43.

23. Muralikrishna A, R.; Hatcher, J. F., Phospholipase A2, reactive oxygen species, and lipid peroxidation in cerebral ischemia. *Free Radic Biol Med* **2006,** *40* (3), 376-87.

24. Campbell, B. C. V. B., C.F.; Donnan, G. A.; Davis, S. M., Acute Ischemic Stroke. In *Handbook of Neuroemergency Clinical Trials*, 2 ed.; Skolnick, B.; Alves, W., Eds. Elsevier: 2018; pp 3-21.

25. Jayaraj, R. L.; Azimullah, S.; Beiram, R.; Jalal, F. Y.; Rosenberg, G. A., Neuroinflammation: friend and foe for ischemic stroke. *J Neuroinflammation* **2019,** *16* (1), 142.

26. Vetrovoy, O. V.; Rybnikova, E. A.; Samoilov, M. O., Cerebral Mechanisms of Hypoxic/Ischemic Postconditioning. *Biochemistry (Mosc)* **2017,** *82* (3), 392-400.

27. Brouns, R.; Wauters, A.; De Surgeloose, D.; Marien, P.; De Deyn, P. P., Biochemical markers for blood-brain barrier dysfunction in acute ischemic stroke correlate with evolution and outcome. *Eur Neurol* **2011,** *65* (1), 23-31.

28. Sandoval, K. E.; Witt, K. A., Blood-brain barrier tight junction permeability and ischemic stroke. *Neurobiol Dis* **2008,** *32* (2), 200-19.

29. Radak, D.; Katsiki, N.; Resanovic, I.; Jovanovic, A.; Sudar-Milovanovic, E.; Zafirovic, S.; Mousad, S. A.; Isenovic, E. R., Apoptosis and Acute Brain Ischemia in Ischemic Stroke. *Curr Vasc Pharmacol* **2017,** *15* (2), 115-122.

30. Yuan, J., Neuroprotective strategies targeting apoptotic and necrotic cell death for stroke. *Apoptosis* **2009,** *14* (4), 469-77.

31. Bivard, A.; Lin, L.; Parsonsb, M. W., Review of stroke thrombolytics. *J Stroke* **2013,** *15* (2), 90-98.

32. Dhillon, S., Alteplase: a review of its use in the management of acute ischaemic stroke. *CNS Drugs* **2012,** *26* (10), 899-926.

33. Ge, X.; Li, C., Savaging brain ischemia by increasing brain uptake of neuroprotectants. In *Brain Targeted Drug Delivery System*, 1 ed.; Gao, H.; Gao, X., Eds. Elsevier: 2019; pp 357-374.

34. Rabinstein, A. A., Treatment of Acute Ischemic Stroke. *Continuum* **2017,** *23* (1), 62-81.

35. Raychev, R. S., J., Mechanical thrombectomy devices for treatment of stroke. *Neurol. Clin. Pract.* **2012,** *2* (3), 231-35.

36. Ganesh, A.; Goyal, M., Thrombectomy for Acute Ischemic Stroke: Recent Insights and Future Directions. *Curr Neurol Neurosci Rep* **2018,** *18* (9), 59.

37. Pulvers, J. N.; Watson, J. D. G., If Time Is Brain Where Is the Improvement in Prehospital Time after Stroke? *Front Neurol* **2017,** *8*, 617.

38. Rubin, M. N.; Barrett, K. M., What to do With Wake-Up Stroke. *Neurohospitalist* **2015,** *5* (3), 161-72.

39. Karmarkar, S. W.; Tischkau, S. A., Influences of the circadian clock on neuronal susceptibility to excitotoxicity. *Front Physiol* **2013,** *4*, 313.

40. Patel, R. A. G.; McMullen, P. W., Neuroprotection in the Treatment of Acute Ischemic Stroke. *Prog Cardiovasc Dis* **2017,** *59* (6), 542-548.

41. Moretti, A.; Ferrari, F.; Villa, R. F., Neuroprotection for ischaemic stroke: current status and challenges. *Pharmacol Ther* **2015,** *146*, 23-34.

42. Sutherland, B. A.; Minnerup, J.; Balami, J. S.; Arba, F.; Buchan, A. M.; Kleinschnitz, C., Neuroprotection for ischaemic stroke: translation from the bench to the bedside. *Int J Stroke* **2012,** *7* (5), 407-18.

43. Xiong, X. Y.; Liu, L.; Yang, Q. W., Refocusing Neuroprotection in Cerebral Reperfusion Era: New Challenges and Strategies. *Front Neurol* **2018,** *9*, 1-11.

44. Majid, A., Neuroprotection in stroke: past, present, and future. *ISRN Neurol* **2014,** *2014*, 1-17.

45. Chamorro, Á.; Dirnagl, U.; Urra, X.; Planas, A. M., Neuroprotection in acute stroke: targeting excitotoxicity, oxidative and nitrosative stress, and inflammation. *The Lancet Neurology* **2016,** *15* (8), 869-881.

46. Auriel, E.; Bornstein, N. M., Neuroprotection in acute ischemic stroke--current status. *J Cell Mol Med* **2010,** *14* (9), 2200-2.

47. Craig, A. J.; Housley, G. D., Evaluation of Gene Therapy as an Intervention Strategy to Treat Brain Injury from Stroke. *Front Mol Neurosci* **2016,** *9*, 1-9.

48. Xu, W.; Zheng, J.; Gao, L.; Li, T.; Zhang, J.; Shao, A., Neuroprotective Effects of Stem Cells in Ischemic Stroke. *Stem Cells Int* **2017,** *2017*, 1-7.

49. Sommer, C. J., Ischemic stroke: experimental models and reality. *Acta Neuropathol* **2017,** *133* (2), 245-261.

50. Cheng, Y. D. A.-K., L; Zivin, J. A., Neuroprotection for Ischemic Stroke: Two Decades of Success and Failure. *NeuroRX* **2004,** *1* (1), 36-45.

51. Miranda, M.; Morici, J. F.; Zanoni, M. B.; Bekinschtein, P., Brain-Derived Neurotrophic Factor: A Key Molecule for Memory in the Healthy and the Pathological Brain. *Front Cell Neurosci* **2019,** *13*, 1-25.

52. Chen, A.; Xiong, L. J.; Tong, Y.; Mao, M., The neuroprotective roles of BDNF in hypoxic ischemic brain injury. *Biomed Rep* **2013,** *1* (2), 167-176.

53. De Vincenti, A. P.; Rios, A. S.; Paratcha, G.; Ledda, F., Mechanisms That Modulate and Diversify BDNF Functions: Implications for Hippocampal Synaptic Plasticity. *Front Cell Neurosci* **2019,** *13*, 1-7.

54. Kowianski, P.; Lietzau, G.; Czuba, E.; Waskow, M.; Steliga, A.; Morys, J., BDNF: A Key Factor with Multipotent Impact on Brain Signaling and Synaptic Plasticity. *Cell Mol Neurobiol* **2018,** *38* (3), 579-593.

55. Nagahara, A. H.; Tuszynski, M. H., Potential therapeutic uses of BDNF in neurological and psychiatric disorders. *Nat Rev Drug Discov* **2011,** *10* (3), 209-19.

56. Liu, W.; Wang, X.; O'Connor, M.; Wang, G.; Han, F., Brain-Derived Neurotrophic Factor and Its Potential Therapeutic Role in Stroke Comorbidities. *Neural Plasticity* **2020,** *2020*, 1-13.

57. Ploughman, M.; Windle, V.; MacLellan, C. L.; White, N.; Dore, J. J.; Corbett, D., Brain-derived neurotrophic factor contributes to recovery of skilled reaching after focal ischemia in rats. *Stroke* **2009,** *40* (4), 1490-5.

58. Zhao, H.; Alam, A.; San, C. Y.; Eguchi, S.; Chen, Q.; Lian, Q.; Ma, D., Molecular mechanisms of brain-derived neurotrophic factor in neuro-protection: Recent developments. *Brain Res* **2017,** *1665*, 1-21.

59. Bejot, Y.; Mossiat, C.; Giroud, M.; Prigent-Tessier, A.; Marie, C., Circulating and brain BDNF levels in stroke rats. Relevance to clinical studies. *Plos One* **2011,** *6* (12), 1-6.

60. Numakawa, T.; Odaka, H.; Adachi, N., Actions of Brain-Derived Neurotrophin Factor in the Neurogenesis and Neuronal Function, and Its Involvement in the Pathophysiology of Brain Diseases. *Int J Mol Sci* **2018,** *19* (11), 1-23.

61. Houlton, J.; Abumaria, N.; Hinkley, S. F. R.; Clarkson, A. N., Therapeutic Potential of Neurotrophins for Repair After Brain Injury: A Helping Hand From Biomaterials. *Front Neurosci* **2019,** *13*, 1-23.

62. Massa, S. M.; Yang, T.; Xie, Y.; Shi, J.; Bilgen, M.; Joyce, J. N.; Nehama, D.; Rajadas, J.; Longo, F. M., Small molecule BDNF mimetics activate TrkB signaling and prevent neuronal degeneration in rodents. *J Clin Invest* **2010,** *120* (5), 1774-85.

63. Nguyen, H. T. H.; Wood, R. J.; Prawdiuk, A. R.; Furness, S. G. B.; Xiao, J.; Murray, S. S.; Fletcher, J. L., TrkB Agonist LM22A-4 Increases Oligodendroglial Populations During Myelin Repair in the Corpus Callosum. *Front Mol Neurosci* **2019,** *12*, 1-12.

64. Fletcher, J. L.; Murray, S. S.; Xiao, J., Brain-Derived Neurotrophic Factor in Central Nervous System Myelination: A New Mechanism to Promote Myelin Plasticity and Repair. *Int J Mol Sci* **2018,** *19* (12), 1-16.

65. Hu, Z.; Zhong, B.; Tan, J.; Chen, C.; Lei, Q.; Zeng, L., The Emerging Role of Epigenetics in Cerebral Ischemia. *Mol Neurobiol* **2017,** *54* (3), 1887-1905.

66. Stanzione, R.; Cotugno, M.; Bianchi, F.; Marchitti, S.; Forte, M.; Volpe, M.; Rubattu, S., Pathogenesis of Ischemic Stroke: Role of Epigenetic Mechanisms. *Genes (Basel)* **2020,** *11* (1), 1-13.

67. Uzdensky, A. B.; Demyanenko, S. V., Epigenetic Mechanisms of Ischemic Stroke. *Biochemistry (Moscow), Supplement Series A: Membrane and Cell Biology* **2020,** *13* (4), 289-300.

68. Bartel, D. P., Metazoan MicroRNAs. *Cell* **2018,** *173* (1), 20-51.

69. Setten, R. L.; Rossi, J. J.; Han, S. P., The current state and future directions of RNAi-based therapeutics. *Nat Rev Drug Discov* **2019,** *18* (6), 421-446.

70. Baumann, V.; Winkler, J., miRNA-based therapies: strategies and delivery platforms for oligonucleotide and non-oligonucleotide agents. *Future Med Chem* **2014,** *6* (17), 1967-84.

71. Chen, W.; Qin, C., General hallmarks of microRNAs in brain evolution and development. *RNA Biol* **2015,** *12* (7), 701-8.

72. Khoshnam, S. E.; Winlow, W.; Farbood, Y.; Moghaddam, H. F.; Farzaneh, M., Emerging Roles of microRNAs in Ischemic Stroke: As Possible Therapeutic Agents. *J Stroke* **2017,** *19* (2), 166-187.

73. Khoshnam, S. E.; Winlow, W.; Farzaneh, M., The Interplay of MicroRNAs in the Inflammatory Mechanisms Following Ischemic Stroke. *J Neuropathol Exp Neurol* **2017,** *76* (7), 548-561.

74. Eyileten, C.; Wicik, Z.; De Rosa, S.; Mirowska-Guzel, D.; Soplinska, A.; Indolfi, C.; Jastrzebska-Kurkowska, I.; Czlonkowska, A.; Postula, M., MicroRNAs as Diagnostic and Prognostic Biomarkers in Ischemic Stroke-A Comprehensive Review and Bioinformatic Analysis. *Cells* **2018,** *7* (12), 1-34.

75. Dharap, A.; Bowen, K.; Place, R.; Li, L. C.; Vemuganti, R., Transient focal ischemia induces extensive temporal changes in rat cerebral microRNAome. *J Cereb Blood Flow Metab* **2009,** *29* (4), 675-87.

76. Flynn, J. M.; Melov, S., SOD2 in mitochondrial dysfunction and neurodegeneration. *Free Radic Biol Med* **2013,** *62*, 4-12.

77. Witwer, K. W.; Sisk, J. M.; Gama, L.; Clements, J. E., MicroRNA regulation of IFN-beta protein expression: rapid and sensitive modulation of the innate immune response. *J Immunol* **2010,** *184* (5), 2369-76.

78. Androvic, P.; Kirdajova, D.; Tureckova, J.; Zucha, D.; Rohlova, E.; Abaffy, P.; Kriska, J.; Valny, M.; Anderova, M.; Kubista, M.; Valihrach, L., Decoding the Transcriptional Response to Ischemic Stroke in Young and Aged Mouse Brain. *Cell Rep* **2020,** *31* (11), 107777.

79. Atri, C.; Guerfali, F. Z.; Laouini, D., MicroRNAs in diagnosis and therapeutics. In *AGO-Driven Non-Coding RNAs*, Mallick, B., Ed. Academic Press: 2019; Vol. 1, pp 137-177.

80. Broderick, J. A.; Zamore, P. D., MicroRNA therapeutics. *Gene Ther* **2011,** *18* (12), 1104-10.

81. Lennox, K. A.; Behlke, M. A., Chemical modification and design of anti-miRNA oligonucleotides. *Gene Ther* **2011,** *18* (12), 1111-20.

82. Wang, Z., The principles of MiRNA-masking antisense oligonucleotides technology. *Methods Mol Biol* **2011,** *676*, 43-9.

83. Fu, Y.; Chen, J.; Huang, Z., Recent progress in microRNA-based delivery systems for the treatment of human disease. *ExRNA* **2019,** *1*, 1-14.

84. Wong, J. K. L.; Mohseni, R.; Hamidieh, A. A.; MacLaren, R. E.; Habib, N.; Seifalian, A. M., Will Nanotechnology Bring New Hope for Gene Delivery? *Trends Biotechnol* **2017,** *35* (5), 434-451.

85. Parveen, S.; Misra, R.; Sahoo, S. K., Nanoparticles: a boon to drug delivery, therapeutics, diagnostics and imaging. *Nanomedicine* **2012,** *8* (2), 147-66.

86. Spencer, A. P.; Torrado, M.; Custodio, B.; Silva-Reis, S. C.; Santos, S. D.; Leiro, V.; Pego, A. P., Breaking Barriers: Bioinspired Strategies for Targeted Neuronal Delivery to the Central Nervous System. *Pharmaceutics* **2020,** *12* (2).

87. Nayerossadat, N.; Maedeh, T.; Ali, P. A., Viral and nonviral delivery systems for gene delivery. *Adv Biomed Res* **2012,** *1* (2), 1-11.

88. Chen, R., Polymers in Drug Delivery: Concepts, Developments and Potential. In *Drug Delivery Systems: Advanced Technologies Potentially Applicable in Personalised Treatment*, 1 ed.; Coelho, J., Ed. Springer: 2013; Vol. 4, pp 1-34.

89. Gáscon, R. A.; Rodríguez-Pozo, A.; Solínis, A. M., Non-Viral Delivery Systems in Gene Therapy. In *Gene Therapy: Tools and Potential Applications*, Molina, M. M., Ed. Intech: 2013; Vol. 1, pp 3-33.

90. Ramamoorth, M.; Narvekar, A., Non viral vectors in gene therapy- an overview. *J Clin Diagn Res* **2015,** *9* (1), 1-6.

91. Shim, M. S.; Kwon, Y. J., Stimuli-responsive polymers and nanomaterials for gene delivery and imaging applications. *Adv Drug Deliv Rev* **2012,** *64* (11), 1046-59.

92. Pêgo, P. A.; Oliveira, H.; Moreno, M. P., Biomaterial-Based Vectors for Targeted Delivery of Nucleic Acids to the Nervous System. In *Drug Delivery Systems: Advanced Technologies Potentially Applicable in Personalised Treatment*, 1 ed.; Coelho, J., Ed. Springer, Dordrecht: 2013; Vol. 4, pp 185-224.

93. Blanco, E.; Shen, H.; Ferrari, M., Principles of nanoparticle design for overcoming biological barriers to drug delivery. *Nat Biotechnol* **2015,** *33* (9), 941-51.

94. Jones, C. H.; Chen, C. K.; Ravikrishnan, A.; Rane, S.; Pfeifer, B. A., Overcoming nonviral gene delivery barriers: perspective and future. *Mol Pharm* **2013,** *10* (11), 4082-98.

95. Rampado, R.; Crotti, S.; Caliceti, P.; Pucciarelli, S.; Agostini, M., Recent Advances in Understanding the Protein Corona of Nanoparticles and in the Formulation of "Stealthy" Nanomaterials. *Front Bioeng Biotechnol* **2020,** *8*, 1-19.

96. Kharazian, B.; Hadipour, N. L.; Ejtehadi, M. R., Understanding the nanoparticle-protein corona complexes using computational and experimental methods. *Int J Biochem Cell Biol* **2016,** *75*, 162-74.

97. Neagu, M.; Piperigkou, Z.; Karamanou, K.; Engin, A. B.; Docea, A. O.; Constantin, C.; Negrei, C.; Nikitovic, D.; Tsatsakis, A., Protein bio-corona: critical issue in immune nanotoxicology. *Arch Toxicol* **2017,** *91* (3), 1031-1048.

98. Gustafson, H. H.; Holt-Casper, D.; Grainger, D. W.; Ghandehari, H., Nanoparticle Uptake: The Phagocyte Problem. *Nano Today* **2015,** *10* (4), 487-510.

99. Berrecoso, G.; Crecente-Campo, J.; Alonso, M. J., Unveiling the pitfalls of the protein corona of polymeric drug nanocarriers. *Drug Deliv Transl Res* **2020,** *10* (3), 730-50.

100. Friedman, A. D.; Claypool, S. E.; Liu, R., The Smart Targeting of Nanoparticles. *Curr Pharm Des* **2013,** *19* (35), 6315-29.

101. Krol, S., Challenges in drug delivery to the brain: nature is against us. *J Control Release* **2012,** *164* (2), 145-55.

102. Zhang, F.; Lin, Y. A.; Kannan, S.; Kannan, R. M., Targeting specific cells in the brain with nanomedicines for CNS therapies. *J Control Release* **2016,** *240*, 212-226.

103. Behzadi, S.; Serpooshan, V.; Tao, W.; Hamaly, M. A.; Alkawareek, M. Y.; Dreaden, E. C.; Brown, D.; Alkilany, A. M.; Farokhzad, O. C.; Mahmoudi, M., Cellular uptake of nanoparticles: journey inside the cell. *Chem Soc Rev* **2017,** *46* (14), 4218-4244.

104. Murugan, K.; Choonara, Y. E.; Kumar, P.; Bijukumar, D.; du Toit, L. C.; Pillay, V., Parameters and characteristics governing cellular internalization and trans-barrier trafficking of nanostructures. *Int J Nanomedicine* **2015,** *10*, 2191-206.

105. Khan, I.; Saeed, K.; Khan, I., Nanoparticles: Properties, applications and toxicities. *Arab J Chem* **2019,** *12* (7), 908-931.

106. Liu, C.; Zhang, N., Nanoparticles in gene therapy principles, prospects, and challenges. *Prog Mol Biol Transl Sci* **2011,** *104*, 509-62.

107. Vermeulen, L. M. P.; De Smedt, S. C.; Remaut, K.; Braeckmans, K., The proton sponge hypothesis: Fable or fact? *Eur J Pharm Biopharm* **2018,** *129*, 184-190.

108. Alex, S. M.; Sharma, C. P., Nanomedicine for gene therapy. *Drug Deliv Transl Res* **2013,** *3* (5), 437-45.

109. Lostalé-Seijo, I.; Montenegro, J., Synthetic materials at the forefront of gene delivery. *Nature Reviews Chemistry* **2018,** *2* (10), 258-277.

110. Barbosa, A. M.; Gonçalves, C. I.; Moreno, D. M. P.; Gonçalves, R. M.; Santos, G. S.; Pêgo, P. A.; Amaral, F. F., Chitosan In *Comprehensive Biomaterials II*, Elsevier: 2017; Vol. 2, pp 279-305.

111. Jennings, A. J.; Bumgardner, D. J., *Chitosan Based Biomaterials: Tissue Engineering and Therapeutics*. 1 ed.; Elsevier: 2017; Vol. 2, p 296.

112. Kim, K. S., *Chitin and Chitosan Derivaties: Advances in Drug Discovery and Developments*

1ed.; CRC Press: 2014; Vol. 1, p 527.

113. Lai, W. F.; Lin, M. C., Nucleic acid delivery with chitosan and its derivatives. *J Control Release* **2009,** *134* (3), 158-68.

114. Cao, Y.; Tan, Y. F.; Wong, Y. S.; Liew, M. W. J.; Venkatraman, S., Recent Advances in Chitosan-Based Carriers for Gene Delivery. *Mar Drugs* **2019,** *17* (6).

115. Kulkarni, A. D.; Patel, H. M.; Surana, S. J.; Vanjari, Y. H.; Belgamwar, V. S.; Pardeshi, C. V., N,N,N-Trimethyl chitosan: An advanced polymer with myriad of opportunities in nanomedicine. *Carbohydr Polym* **2017,** *157*, 875-902.

116. Mourya, V. K.; Inamdar, N. N., Trimethyl chitosan and its applications in drug delivery. *J Mater Sci Mater Med* **2009,** *20* (5), 1057-79.

117. Goy, C. R.; Morais, T. B. S.; Assis, B. G. O., Evaluation of the antimicrobial activity of chitosan and its quaternized derivative on E. coli and S. aureus growth. *Rev Bras Farmacogn* **2016,** *26* (1), 122-127.

118. Andreica, B. L.; Cheng, X.; Marin, L., Quaternary ammonium salts of chitosan. A critical overview on the synthesis and properties generated by quaternization. *Eur Polym J* **2020,** *139*, 1-16.

119. Ways, M. M. T.; Lau, M. W.; Khutoryanskiy, V. V., Chitosan and Its Derivatives for Application in Mucoadhesive Drug Delivery Systems. *Polymers (Basel)* **2018,** *10* (3), 1-37.

120. Aderibigbe, A. B.; Naki, T., Chitosan-Based Nanocarriers for Nose to Brain Delivery. *Appl Sci* **2019,** *9* (11), 1-27.

121. Jokerst, J. V.; Lobovkina, T.; Zare, R. N.; Gambhir, S. S., Nanoparticle PEGylation for imaging and therapy. *Nanomedicine (Lond)* **2011,** *6* (4), 715-28.

122. Owens, D. E.; Peppas, N. A., Opsonization, biodistribution, and pharmacokinetics of polymeric nanoparticles. *Int J Pharm* **2006,** *307* (1), 93-102.

123. Suk, J. S.; Xu, Q.; Kim, N.; Hanes, J.; Ensign, L. M., PEGylation as a strategy for improving nanoparticle-based drug and gene delivery. *Adv Drug Deliv Rev* **2016,** *99* (Pt A), 28-51.

124. Gomes, C. P.; Varela-Moreira, A.; Leiro, V.; Lopes, C. D. F.; Moreno, P. M. D.; Gomez-Lazaro, M.; Pego, A. P., A high-throughput bioimaging study to assess the impact of chitosan-based nanoparticle degradation on DNA delivery performance. *Acta Biomater* **2016,** *46*, 129-140.

125. Moreno, P. M.; Santos, J. C.; Gomes, C. P.; Varela-Moreira, A.; Costa, A.; Leiro, V.; Mansur, H.; Pego, A. P., Delivery of Splice Switching Oligonucleotides by Amphiphilic Chitosan-Based Nanoparticles. *Mol Pharm* **2016,** *13* (2), 344-56.

126. McNeil, E. S., Challenges for Nanoparticle Characterization. In *Characterization of Nanoparticles Intended for Drug Delivery* 1ed.; Walker, M. J., Ed. Humana Press: 2011; Vol. 1, pp 9-15.

127. Stetefeld, J.; McKenna, S. A.; Patel, T. R., Dynamic light scattering: a practical guide and applications in biomedical sciences. *Biophys Rev* **2016,** *8* (4), 409-427.

128. Yang, G.; Wang, Y., Dynamic Light Scattering of DNA-Ligand Complexes. In *Bacterial Chromatin*, 1 ed.; Dame, T. R., Ed. Humana Press: 2018; pp 161-176.

129. Gref, R.; Lu, M.; Harnish, S.; Quellec, P.; Marchand, M.; Blunk, T.; Muller, H. R.; Dellacherie, E., 'Stealth' corona-core nanoparticles surface modified by polyethylene glycol (PEG): influences of the corona (PEG chain length and surface density) and of the core composition on phagocytic uptake and plasma protein adsorption

Colloid Surface B **2000,** *18* (3-4), 301-13.

130. Danaei, M.; Dehghankhold, M.; Ataei, S.; Hasanzadeh, D. F.; Javanmard, R.; Dokhani, A.; Khorasani, S.; Mozafari, M. R., Impact of Particle Size and Polydispersity Index on the Clinical Applications of Lipidic Nanocarrier Systems. *Pharmaceutics* **2018,** *10* (2), 1-17.

131. Shao, X. R.; Wei, X. Q.; Song, X.; Hao, L. Y.; Cai, X. X.; Zhang, Z. R.; Peng, Q.; Lin, Y. F., Independent effect of polymeric nanoparticle zeta potential/surface charge, on their cytotoxicity and affinity to cells. *Cell Prolif* **2015,** *48* (4), 465-74.

132. Raval, N.; Maheshwari, R.; Kalyane, D.; Youngren-Ortiz, R. S.; Chougule, B. M.; Tekade, K. R., Importance of Physicochemical Characterization of Nanoparticles in Pharmaceutical Product Development. In *Basic Fundamentals of Drug Delivery*, 1 ed.; Tekade, K. R., Ed. Academic Press: 2019; pp 369-400.

133. Fonte, P.; Andrade, F.; Araujo, F.; Andrade, C.; Neves, J.; Sarmento, B., Chitosan-coated solid lipid nanoparticles for insulin delivery. *Methods Enzymol* **2012,** *508*, 295-314.

134. Gutoaia, A.; Schuster, L.; Margutti, S.; Laufer, S.; Schlosshauer, B.; Krastev, R.; Stoll, D.; Hartmann, H., Fine-tuned PEGylation of chitosan to maintain optimal siRNA-nanoplex bioactivity. *Carbohydr Polym* **2016,** *143*, 25-34.

135. Janke, C.; Magiera, M. M., The tubulin code and its role in controlling microtubule properties and functions. *Nat Rev Mol Cell Biol* **2020,** *21* (6), 307-326.

136. Boltaev, U.; Meyer, Y.; Tolibzoda, F.; Jacques, T.; Gassaway, M.; Xu, Q.; Wagner, F.; Zhang, Y. L.; Palmer, M.; Holson, E.; Sames, D., Multiplex quantitative assays indicate a need for reevaluating reported small-molecule TrkB agonists. *Sci Signal* **2017,** *10* (493), 1-10.

137. Huang, E. J.; Reichardt, L. F., Trk receptors: roles in neuronal signal transduction. *Annu Rev Biochem* **2003,** *72*, 609-42.

138. Fukui, M.; Choi, H. J.; Zhu, B. T., Mechanism for the protective effect of resveratrol against oxidative stress-induced neuronal death. *Free Radic Biol Med* **2010,** *49* (5), 800-13.

139. Fukui, M.; Song, J. H.; Choi, J.; Choi, H. J.; Zhu, B. T., Mechanism of glutamate-induced neurotoxicity in HT22 mouse hippocampal cells. *Eur J Pharmacol* **2009,** *617* (1-3), 1-11.

140. Sun, J.; Ren, X.; Simpkins, J. W., Sequential Upregulation of Superoxide Dismutase 2 and Heme Oxygenase 1 by tert-Butylhydroquinone Protects Mitochondria during Oxidative Stress. *Mol Pharmacol* **2015,** *88* (3), 437-49.

141. Xu, X.; Chua, C. C.; Kong, J.; Kostrzewa, R. M.; Kumaraguru, U.; Hamdy, R. C.; Chua, B. H., Necrostatin-1 protects against glutamate-induced glutathione depletion and caspase-independent cell death in HT-22 cells. *J Neurochem* **2007,** *103* (5), 2004-14.

142. Kizhuveetil, U.; Palukuri, M. V.; Sharma, P.; Karunagaran, D.; Rengaswamy, R.; Suraishkumar, G. K., Entrainment of superoxide rhythm by menadione in HCT116 colon cancer cells. *Sci Rep* **2019,** *9* (1), 1-12.

143. Fukui, M.; Choi, H. J.; Zhu, B. T., Rapid generation of mitochondrial superoxide induces mitochondrion-dependent but caspase-independent cell death in hippocampal neuronal cells that morphologically resembles necroptosis. *Toxicol Appl Pharmacol* **2012,** *262* (2), 156-66.

144. Rajkovic, O.; Gourmel, C.; d'Arcy, R.; Wong, R.; Rajkovic, I.; Tirelli, N.; Pinteaux, E., Reactive Oxygen Species-Responsive Nanoparticles for the Treatment of Ischemic Stroke. *Adv Ther* **2019,** *2*, 1-15.

145. Chen, X.; Zhong, Z.; Xu, Z.; Chen, L.; Wang, Y., 2',7'-Dichlorodihydrofluorescein as a fluorescent probe for reactive oxygen species measurement: Forty years of application and controversy. *Free Radic Res* **2010,** *44* (6), 587-604.

146. Wang, Y.; Zhang, Y.; Yang, L.; Yuan, J.; Jia, J.; Yang, S., SOD2 Mediates Curcumin-Induced Protection against Oxygen-Glucose Deprivation/Reoxygenation Injury in HT22 Cells. *Evid Based Complement Alternat Med* **2019,** *2019*, 1-14.

Annex

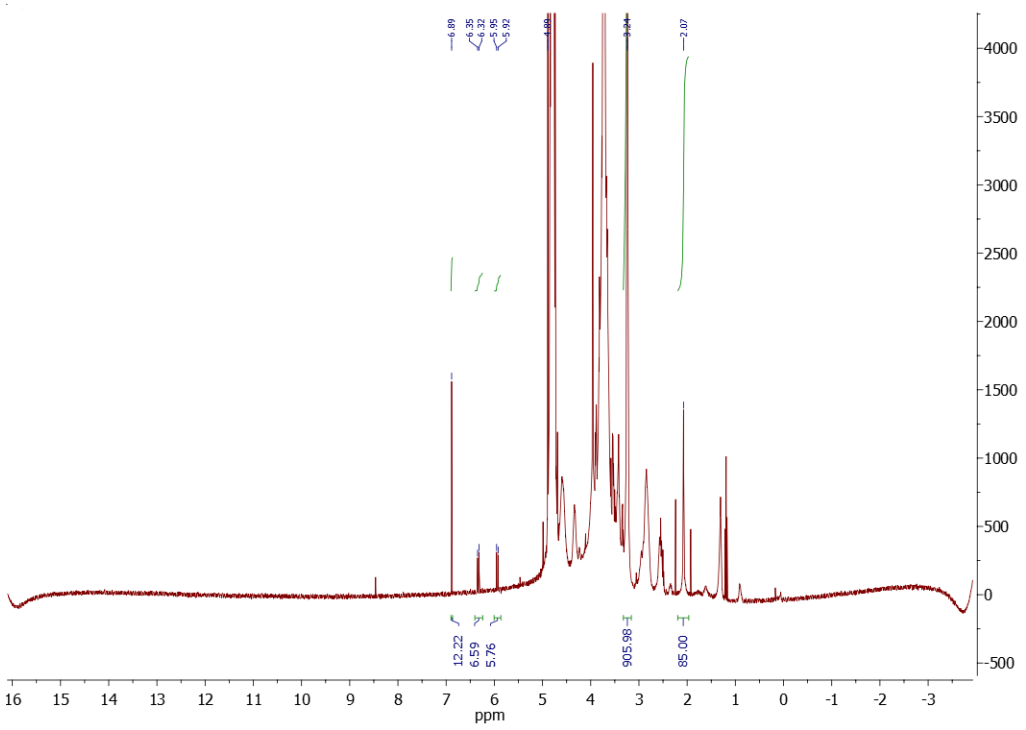

Figure A. 1- ^{1}H-NMR Spectrum of TMC-PEG-MAL Polymer (D_2O; 400 MHz)

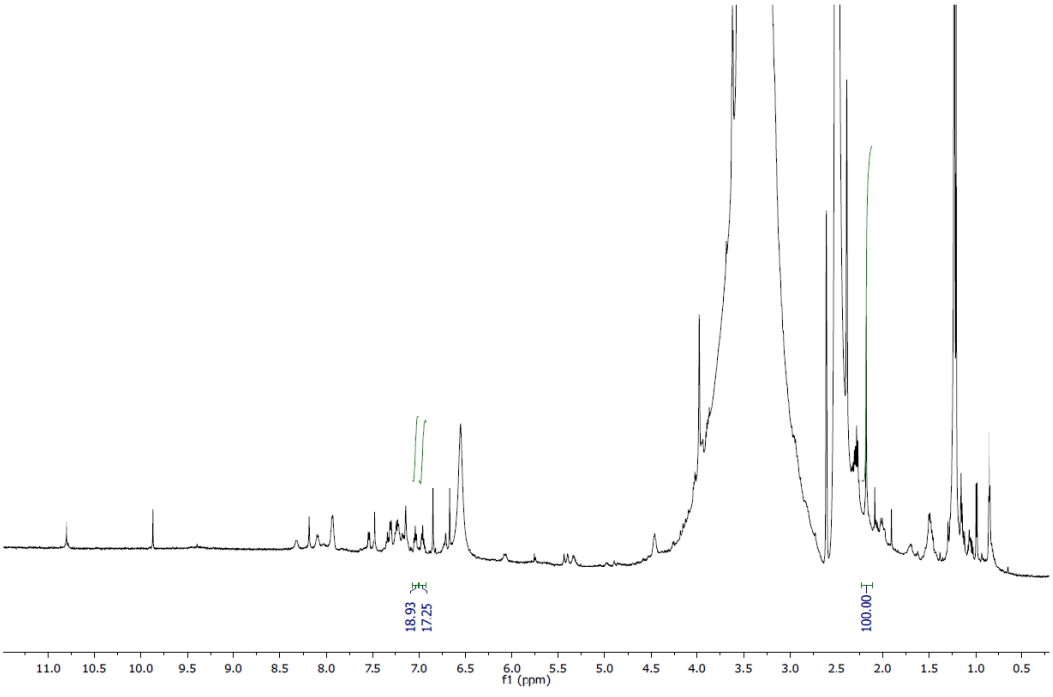

Figure A. 2- ^{1}H-NMR Spectrum of TMC-PEG-LM22A1 Polymer (DMSO; 600 MHz)

Table A. 1- Maximum absorption wavelength and respective absorbances of LM22A1, LM22A1-Cys and TMC-PEG-LM22A1 compounds

Compound	λmax(nm)	Abs
LM22A1	225	0.877
LM22A1-Cys	234	1.99
TMC-PEG-LM22A1	225	0.05

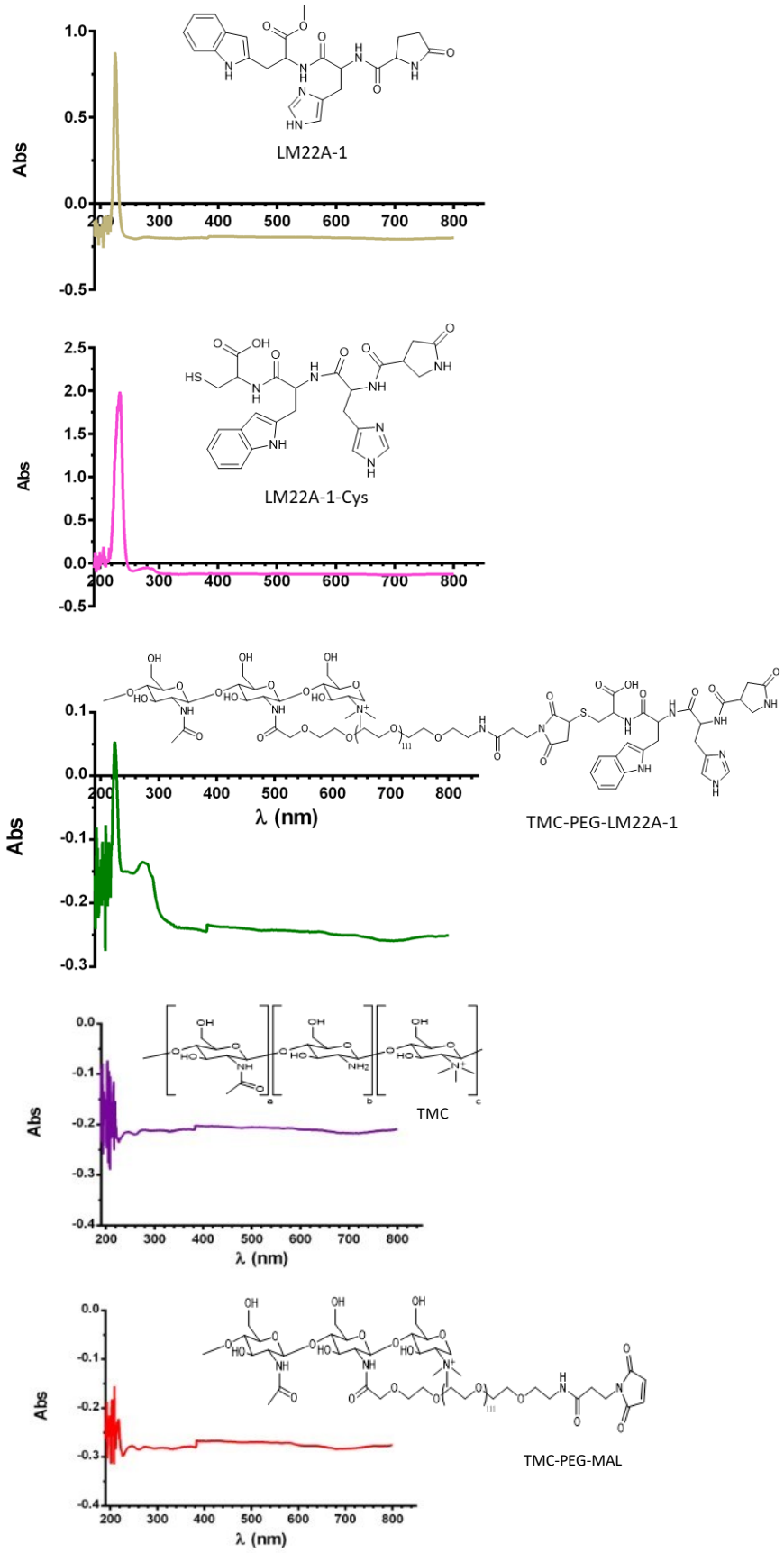

Figure A. 3- UV/ VIS spectra and respective chemical structures of the LM22A1, LM22A-Cys, TMC-PEG-LM22A1, TMC and TMC-PEG-MAL compounds

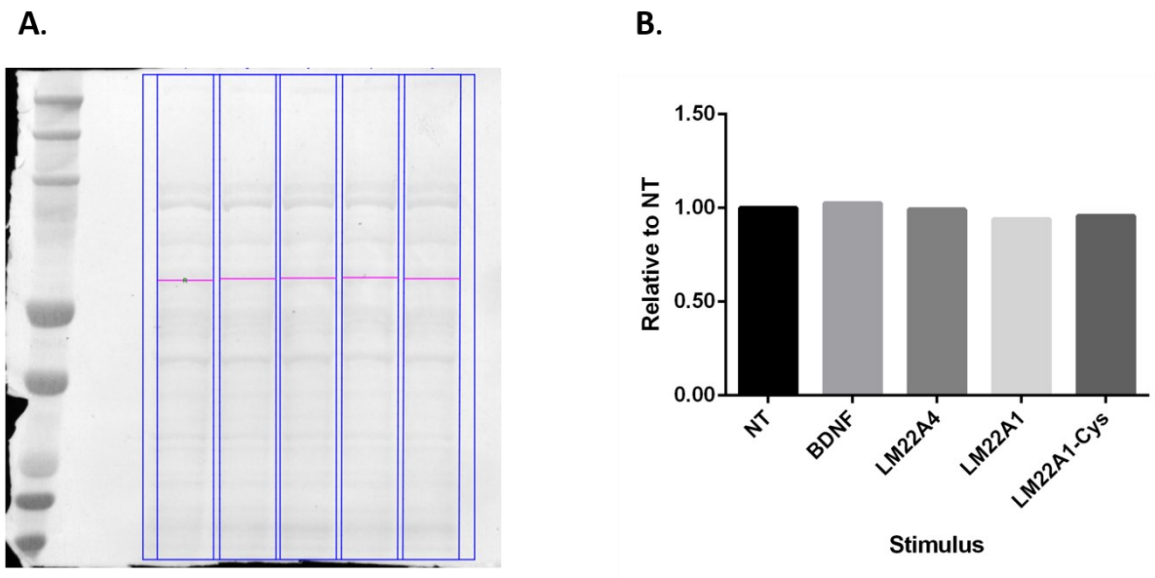

Figure A. 4- Total protein ponceau stained membrane blots of the experience with HTT22-GFP cells non-treated or incubated for 60 minutes with BDNF or LM22A4, LM22A1 and LM22A1-Cys compounds (A.) and respective total protein quantification relative to the control (NT) of the pink selected band (B.).

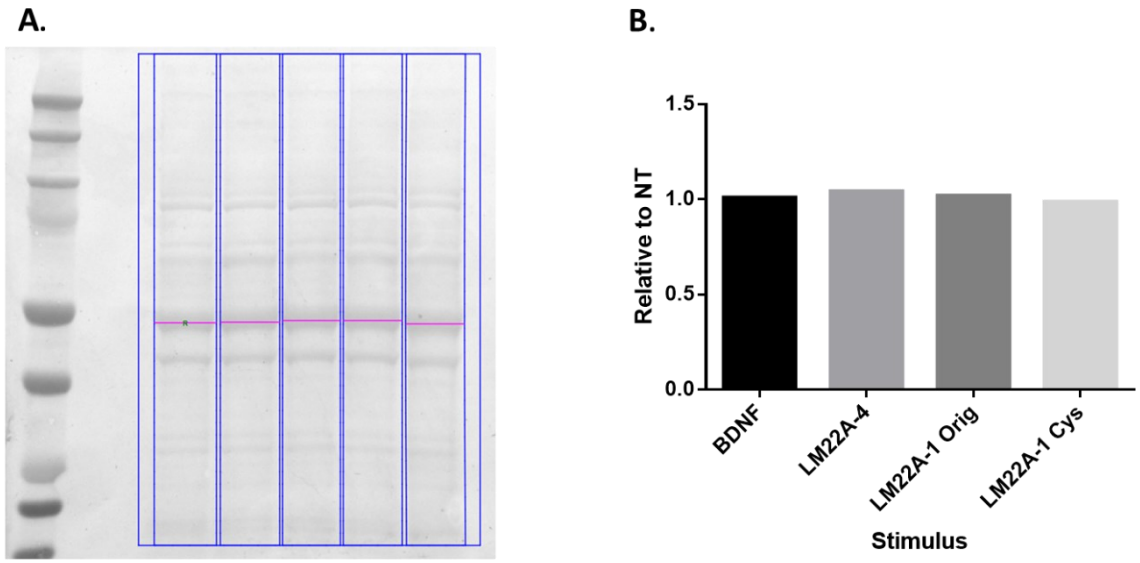

Figure A. 5- Total protein ponceau stained membrane blots of one experiment with NCCC cells cultured during 7 days *in vitro*, non- treated or incubated for 60 minutes with BDNF or LM22A4, LM22A1 and LM22A1-Cys compounds (A.) and respective quantification relative to the control (NT) of a selected band (B.).

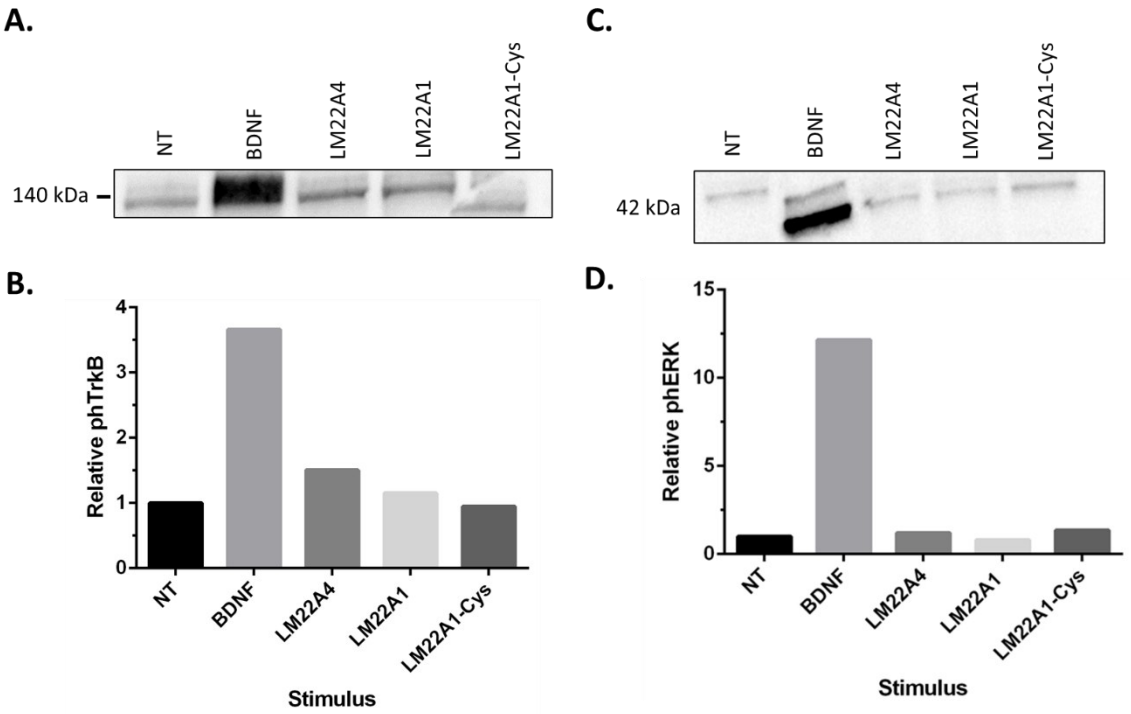

Figure A. 6- Second western blot experiment for NCCC cells cultured for 7 days *in vitro*, non-treated or incubated for 60 minutes with BDNF or LM22A4, LM22A1 and LM22A1-Cys compounds. A. Detection of the phosphorylated TrkB-receptor (140 kDa) and respective quantified fold changes compared to the untreated cells Although the membrane has a cut, an analysis of the same area per band was guaranteed. (B.). C. Identification of phosphorylated ERK2 protein and its signal quantification represented as fold variations (D.). Band inclination occurred and the lower band of the BDNF was analyzed in comparison with the others.

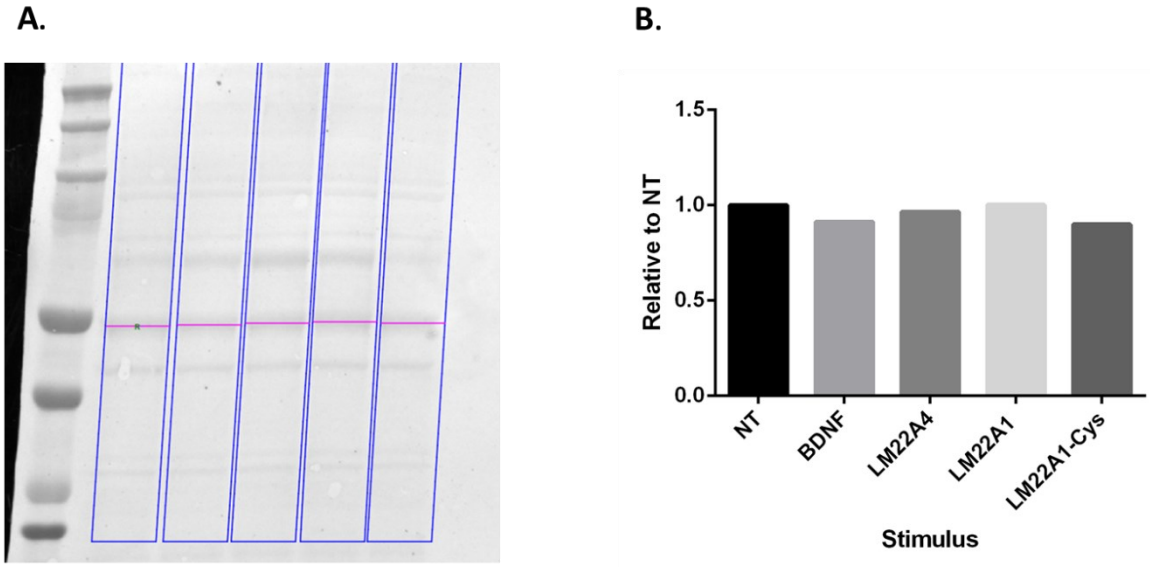

Figure A. 7- Total protein ponceau stained membrane blots of the experience with NCCC cells cultured during 14 days *in vitro*, non- treated or incubated for 60 minutes with BDNF or LM22A4, LM22A1 and LM22A1-Cys compounds (A.) and respective quantification relative to the control (NT) of a selected band (B.).

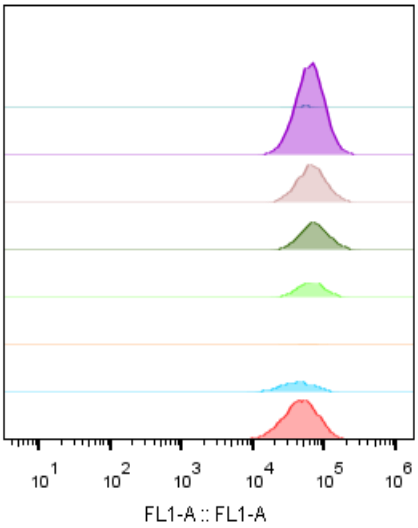

	Sample Name	Subset Name	Count	Median : FL1-A
	B05 fenton 24.fcs	HT22-GFP	213	54832
	B03 GLU 0.25 24.fcs	HT22-GFP	11538	59426
	B02 GLU 0.5 24 .fcs	HT22-GFP	4691	62365
	B01 Glu 1 24.fcs	HT22-GFP	3351	67589
	A06 glu 2 24.fcs	HT22-GFP	1850	61567
	A05 glU 4 24.fcs	HT22-GFP	161	49786
	A02 CTRL SDCF 24.fcs	HT22-GFP	1586	39362
	A01 CTRL CDCF 24.fcs	HT22-GFP	6229	43772

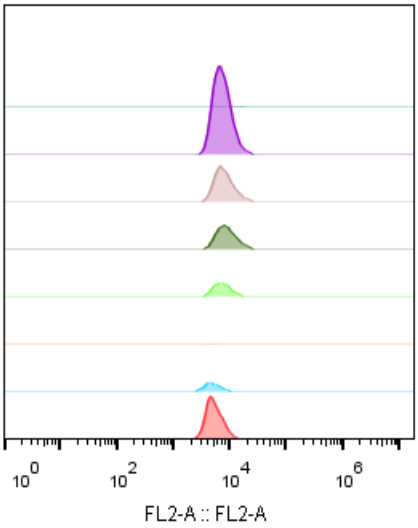

	Sample Name	Subset Name	Count	Median : FL1-A
	B05 fenton 24.fcs	FL1-A subset	143	54832
	B03 GLU 0.25 24.fcs	FL1-A subset	10178	62970
	B02 GLU 0.5 24 .fcs	FL1-A subset	4198	65449
	B01 Glu 1 24.fcs	FL1-A subset	3068	68907
	A06 glu 2 24.fcs	FL1-A subset	1676	64197
	A05 glU 4 24.fcs	FL1-A subset	112	62970
	A02 CTRL SDCF 24.fcs	FL1-A subset	962	50920
	A01 CTRL CDCF 24.fcs	FL1-A subset	4258	54832

Figure A. 8- Histogram with FL1 and FL2 signal for cells treated for 24 hours with glutamate-0.25 mM (B03-purple), 0.5 mM (B02-pink), 1 mM (B01-dark green), 2 mM (A06-green) 4 mM (A05-orange) and respective controls with cells treated (A01-red) or not treated (A02-blue) with the DCFH2 -DA probe and fenton reagent (B05-turquoise).

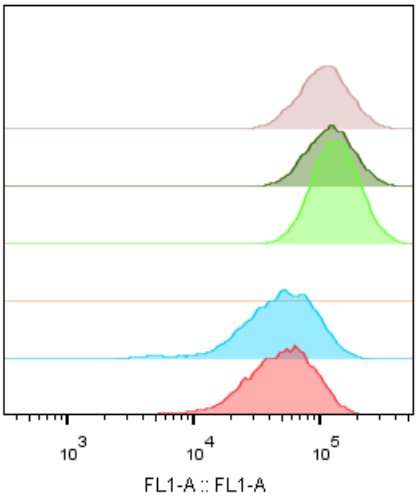

	Sample Name	Subset Name	Count	Median : FL1-A
	C02 Glu 1 2.fcs	HT22-GFP	6715	105691
	C01 glu 2 2.fcs	HT22-GFP	6059	118477
	B06 Glu 4 2.fcs	HT22-GFP	10603	129718
	B04 Fenton 2.fcs	HT22-GFP	85,0	122407
	A04 glu2 SCF.fcs	HT22-GFP	10169	49360
	A03 CTRL DCF 2.fcs	HT22-GFP	10183	48561

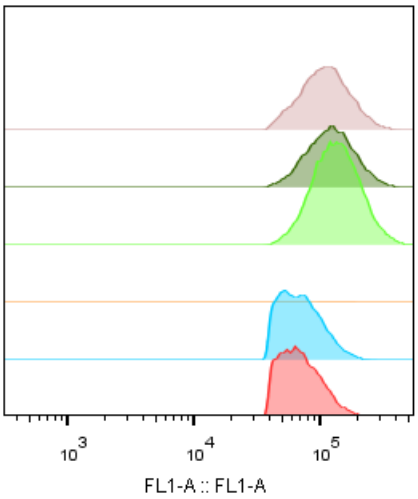

	Sample Name	Subset Name	Count	Median : FL1-A
	C02 Glu 1 2.fcs	FL1-A subset	6588	106846
	C01 glu 2 2.fcs	FL1-A subset	6033	118692
	B06 Glu 4 2.fcs	FL1-A subset	10552	129953
	B04 Fenton 2.fcs	FL1-A subset	80,0	123970
	A04 glu2 SCF.fcs	FL1-A subset	6532	66089
	A03 CTRL DCF 2.fcs	FL1-A subset	6432	65256

Figure A. 9- *Histogram with FL1 and FL2 signal for cells treated for 2 hours with glutamate- 1 mM (CO2-pink), 2 mM (CO1- dark green) 4 mM (B06-green) and respective controls with cells treated (A03-red) or not treated (A04-blue) and fenton reagent (B04-orange) with the DCFH2-DA probe.*

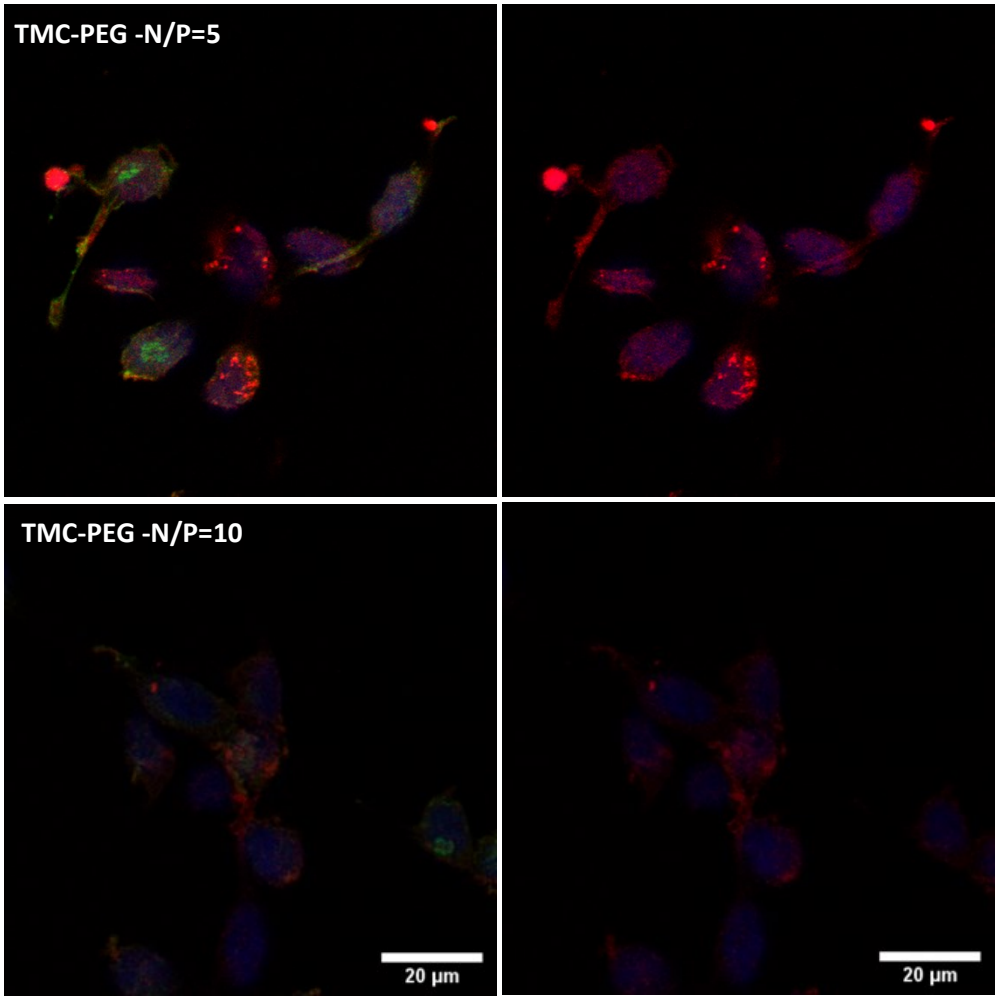

Figure A. 10- HT22-GFP cells treated with nanoparticles of TMC-PEG complexed with microRNA Dy547 (25 nM), at N/P ratios of 5 and 10. The right column exhibit the co-localization of nuclei (blue), F-actin (green) and micro-RNA Dy547 (red). In the left column is presented the same images with the nuclei and micro-RNA Dy547 signal. Images obtained by confocal microscopy.

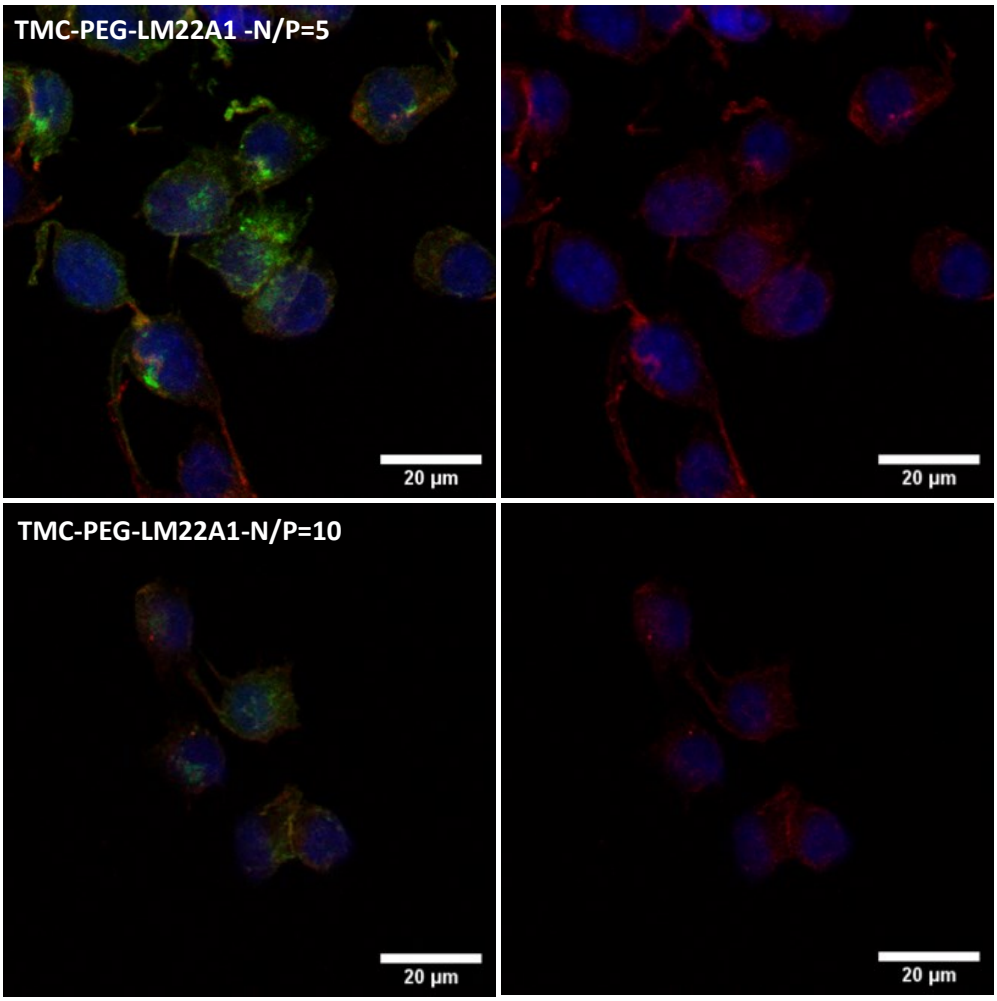

Figure A. 11- HT22-GFP cells treated with nanoparticles of TMC-PEG complexed with microRNA Dy547 (25 nM), at N/P ratios of 5 and 10. The right column exhibit the co-localization of nuclei (blue), F-actin (green) and micro-RNA Dy547 (red). In the left column is presented the same images with the nuclei and micro-RNA Dy547 signal. Images acquired by confocal microscopy.